

Electronic Theses and Dissertations, 2004-2019

2013

Electrohydrodynamic Manipulation Of Liquid Droplet Emulsions In A Microfluidic Channel

Jonathan Wehking
University of Central Florida

 Part of the [Mechanical Engineering Commons](#)
Find similar works at: <https://stars.library.ucf.edu/etd>
University of Central Florida Libraries <http://library.ucf.edu>

This Doctoral Dissertation (Open Access) is brought to you for free and open access by STARS. It has been accepted for inclusion in Electronic Theses and Dissertations, 2004-2019 by an authorized administrator of STARS. For more information, please contact STARS@ucf.edu.

STARS Citation

Wehking, Jonathan, "Electrohydrodynamic Manipulation Of Liquid Droplet Emulsions In A Microfluidic Channel" (2013). *Electronic Theses and Dissertations, 2004-2019*. 2876.
<https://stars.library.ucf.edu/etd/2876>

ELECTROHYDRODYNAMIC MANIPULATION OF LIQUID DROPLET EMULSIONS IN A
MICROFLUIDIC CHANNEL

by

JONATHAN D. WEHKING
B.S. University of Central Florida, 2005
M.S. University of Central Florida, 2008

A dissertation submitted in partial fulfilment of the requirements
for the degree of Doctor of Philosophy
in the Department of Mechanical and Aerospace Engineering
in the College of Engineering and Computer Science
at the University of Central Florida

Fall Term
2013

© 2013 Jonathan D. Wehking

ABSTRACT

This work specifically aims to provide a fundamental framework, with some experimental validation, for understanding droplet emulsion dynamics in a microfluidic channel with an applied electric field. Electrification of fluids can result in several different modes of electrohydrodynamics (EHD). Several studies to date have provided theoretical, experimental, and numerical results for stationary droplet deformations and some flowing droplet configurations, but none have reported a method by which droplets of different diameters can be separated, binned and routed through the use of electric fields. It is therefore the goal of this work to fill that void and report a comprehensive understanding of how the electric field can affect flowing droplet dynamics.

This work deals with two primary models used in electrohydrodynamics: the leaky dielectric model and the perfect dielectric model. The perfect dielectric model assumes that fluids with low conductivities do not react to any effects from the small amount of free charge they contain, and can be assumed as dielectrics, or electrical insulators. The leaky dielectric model suggests that even though the free charge is minimal in fluids with low conductivities, it is still enough to affect droplet deformations. Finite element numerical results of stationary droplet deformations, implemented using the level set method, compare well both qualitatively (prolate/oblate and vortex directions), and quantitatively with results published by other researchers. Errors of less than 7.5% are found when comparing three-dimensional (3D) numerical results of this study to results predicted by the 3D leaky dielectric model, for a stationary high conductivity drop suspended in a slightly lower conductivity suspending medium. Droplet formations in a T-junction with no applied electric field are adequately predicted numerically using the level set finite element technique, as demonstrated by other researchers and verified in this study. For 3D models, droplet size is within 6%, and droplet production frequency is within 2.4% of experimental values found in the microfluidic T-junction device. In order to reduce computational complexity, a larger scale model was solved first

to obtain electrical potential distributions localized at the channel walls for the electrode placement configurations.

Droplet deceleration and pinning is demonstrated, both experimentally and numerically, by applying steep gradients of electrical potential to the microchannel walls. As droplets flow over these electrical potential “steps,” they are pinned to the channel walls if the resulting electric forces are large enough to overcome the hydrodynamic forces. A balance between four dimensionless force ratios, the electric Euler number (Eu_e – ratio of inertial to electric forces), Mason number (Ma – ratio of viscous to electric forces), electric pressure (Ps – ratio of upstream pressure forces to electric forces), and the electric capillary number (Ca_e – ratio of electric to capillary forces) are used to quantify the magnitudes of each of these forces required to pin a droplet, and is consistent with a cubic dependency on the drop diameter. For larger drop diameters, effects of hydrodynamic forces become more prominent, and for smaller droplets, a greater electric forces is required due to the proximity of the droplet boundary with reference to the electrified channel wall. Droplet deceleration and pinning can be exploited to route droplets into different branches of a microfluidic T-junction. In addition, using steep electrical potential gradients placed strategically along a microchannel, droplets can even be passively binned by size into separate branches of the microfluidic device. These characteristics have been identified and demonstrated in this work.

ACKNOWLEDGMENTS

I first wish to acknowledge my advisors. I thank Dr. Chew for placing complete trust in my abilities, providing endless lessons in thinking and working independently, and imparting valuable career (and life) advice. I thank Dr. Kumar for his endless patience, unquestionable dedication to his students, and for holding my work to such high standards.

I also wish to acknowledge my friends and colleagues. While I would like to list and thank them all, I will most fondly remember Amjad and James because of our empathic and motivating conversations (. . . and for the gallons of coffee shared between us).

Finally, I wish to acknowledge my family. I thank my mother and father for instilling such a strong desire for furthering my education, and for their unabated encouragement throughout my life.

To my beautiful wife, Rebekah, and our son, Luke, I owe everything. Rebekah, this work would not have been possible without your courageous support during my post-graduate pursuits, and your confidence in my aptitudes. Luke, you are the creation of which I am most proud. My love for you both extends eternally.

TABLE OF CONTENTS

LIST OF FIGURES	ix
LIST OF TABLES	xv
CHAPTER 1: INTRODUCTION	1
CHAPTER 2: LITERATURE REVIEW	3
Non-electrified Droplets	3
Electrowetting	9
Electrocoalescence	12
Electrophoresis and Dielectrophoresis	15
Electroosmosis	16
Deforming Stationary Droplets in an Electric Field	18
Electrified Flowing Droplets	22
CHAPTER 3: THEORETICAL MODEL	26
Fluid Mechanics	26
Electric Field	27

Normalization	30
CHAPTER 4: MATERIALS AND EXPERIMENTAL SET-UP	33
Microchannel Material	33
Microchannel Design	37
Electrode Placements	39
Experimental Setup	42
CHAPTER 5: NUMERICAL MODEL	45
Mathematical Formulation	45
Discretization/Solver Scheme	47
Possible Simplifications	50
CHAPTER 6: RESULTS	57
Validation of the Numerical Models	57
Validation 1: T-Junction with No Electric Field	58
Validation 2: Stationary Droplet Under Electric Field	59
Computational Sensitivity Studies	66
Droplet Deceleration and Pinning	71

Droplet Routing 86

Droplet Binning by Size 90

CHAPTER 7: CONCLUSION 97

REFERENCES 99

LIST OF FIGURES

Figure 1:	Schematic of three droplet production configurations: (a) co-flowing, (b) flow focussing, (c) cross-flowing - figure reproduced from [1].	4
Figure 2:	Example of electrowetting experiment - figure reproduced from [2].	11
Figure 3:	Electrocoalescence experiment performed by Gu et al [3]. Cells (a)-(f) depict flow with no applied electric field, and cells (g)-(l) depict flow with an applied electric field. Electrodes are located at the intersection between the three channel branches - reprinted from [3]	13
Figure 4:	Potential distribution (φ) and resulting velocity profile (u) for electroosmotic induced flow - figure reproduced from [4].	17
Figure 5:	Observed (stationary) droplet shapes under an applied electric field.	19
Figure 6:	PDMS microchannel fabrication steps - adapted from [5, 6].	34
Figure 7:	Microsolidics fabrication steps (left column) and electrode healing procedure (right column) - adapted from [7].	36
Figure 8:	T-junction microchannel geometry.	38
Figure 9:	Full chip design with five T-junction microchannels of varying widths. . . .	39
Figure 10:	Three electrode placement configurations for MKI channel design.	40

Figure 11: MKII electrode configuration. The continuous and dispersed channel widths, and channel height are $w_c = 100\mu m$, $w_d = 50\mu m$, and $h = 50\mu m$ respectively.	41
Figure 12: Damaged electrode after applying $V_0 > 3500V$	42
Figure 13: Schematic of experimental setup.	43
Figure 14: Steady electrical potential distribution of entire chip, and resulting channel boundary electrical potential distribution for MKI - configuration 1. Color scale represents electrical potential, and arrow vectors represent the electric field distribution (left). Numbers along bottom of plot indicate position along channel boundary (see inset).	51
Figure 15: Channel boundary electrical potential distribution for MKI - configuration 2.	52
Figure 16: Channel boundary electrical potential distribution for MKI - configuration 3.	52
Figure 17: Interface thickness change for two different mesh densities (quarter symmetry model).	55
Figure 18: (a) - Percent error distribution in electrical potential between perfect and leaky dielectric assumptions. (b) - Maximum error for various permittivity ratios.	56

Figure 19: Qualitative comparison between experimental and numerical droplets. The continuous fluid is silicone oil and the dispersed fluid is deionized water (see table 2 for material properties) with $Q_c = 200\mu L/hr$, $Q_d = 100\mu L/hr$, $w_c = 200\mu m$, and $w_d = 100\mu m$. For the experimental and 3D numerical cases, the channel height is $h = 100\mu m$	58
Figure 20: Schematic of two-dimensional stationary droplet deformed shapes. $q = \epsilon_c/\epsilon_d$, and is the ratio of relative permittivities, and D is the droplet deformation defined by equation 17, 18, or 19.	61
Figure 21: Two-dimensional computational model, highlighting dimensions and boundary conditions.	63
Figure 22: Two-dimensional quantitative comparison of theoretical (equation 17) and numerical (equation 18) droplet deformations.	64
Figure 23: Three-dimensional computational model, highlighting dimensions and boundary conditions.	65
Figure 24: Three-dimensional quantitative comparison of theoretical (equation 19) and numerical (equation 18) droplet deformations.	66
Figure 25: Two-dimensional numerical drop deformation with respect to changes in boundary distance from droplet for $q = 10.33$ ($D = 0$).	67
Figure 26: Two-dimensional drop deformation mesh sensitivity study for $q = 10.33$ ($D = 0$).	70
Figure 27: Three-dimensional drop deformation mesh sensitivity study for $q = 9.57$ ($D = 0$).	70

Figure 28:	Force diagram on unconfined and confined droplets, with boundary conditions used for electrical potential. A steep potential gradient is used on bottom boundary, and zero potential is used on top boundary.	73
Figure 29:	Two-dimensional electric pinning force dependency on drop diameter. Polynomial fit is $F_E = O(N/m) = 4.784 \times 10^6 d^2 - 8.538 \times 10^6 d + 0.055$ with $R^2 = 0.989$. Note that $d = O(m)$ when using the curve fit.	77
Figure 30:	Individual magnitudes of 2D polynomial fit: $F_E = O(N/m) = 4.784 \times 10^6 d^2 - 8.538 \times 10^6 d + 0.055$. Note that $d = O(m)$ when using the curve fit.	79
Figure 31:	Three-dimensional electric pinning force dependency on dimensionless drop diameter. Polynomial fit is $F_E = O(\mu N) = -3.136 \times 10^{12} d^3 + 8.195 \times 10^8 d^2 - 6.369 \times 10^4 d + 1.919$. with $R^2 = 0.999$. Note that $d = O(m)$ when using curve the fit.	80
Figure 32:	Individual magnitudes of 3D polynomial fit $F_E = O(\mu N) = -3.136 \times 10^{12} d^3 + 8.195 \times 10^8 d^2 - 6.369 \times 10^4 d + 1.919$. Note that $d = O(m)$ when using the curve fit.	82
Figure 33:	Qualitative comparison between experimental and numerical droplets. The continuous fluid is silicone oil and the dispersed fluid is deionized water (see table 2 for material properties) with $Q_c = 200 \mu L/hr$, $Q_d = 100 \mu L/hr$ and $w_c = 200 \mu m$. For the experimental and 3D numerical cases, the channel height is $h = 100 \mu m$	83
Figure 34:	Three-dimensional electrostatic simulation of electrical potential distributions for MKI (a) and MKII (b) microchannel designs. Red color indicates applied potential ($V = V_0$) and blue indicates grounded region ($V = 0$).	85

Figure 35: Qualitative comparison between experiments conducted on the MKII channel design and three-dimensional numerical droplets. Drop sizes observed experimentally for the MKII channel design were not exactly matched numerically. Two-dimensional numerical droplets depicted identical behavior, and are therefore not shown. The continuous fluid is silicone oil and the dispersed fluid is deionized water (see table 2 for material properties). 86

Figure 36: Two-dimensional numerical simulation of droplet routing configurations. Schematic and sequence of images at different times are listed for a T-junction electrified in the top corner (left column), and the bottom corner (right column) for two different drop diameters (d). Once pinned, the droplet position at all future time steps overlap the final pinning location (droplet totally arrested with no additional deformation). The channel width is $100\mu m$, and fluid properties are listed in table 2. 87

Figure 37: Three-dimensional numerical simulation of droplet routing configurations. Schematic and sequence of images at different times are listed for a T-junction electrified in the top corner (left column), and the bottom corner (right column) for two different drop diameters (d). Once pinned, the droplet position at all future time steps overlap the final pinning location (droplet totally arrested with no additional deformation). The channel width and height are $100\mu m$, and $50\mu m$ respectively, and fluid properties are listed in table 2. 90

Figure 38: Two-dimensional numerical simulation of a two droplet binning configuration. Sequence of images are listed for the non-electrified two branch microchannel (left), and the electrified two branch microchannel (right), along with the electrical potential distribution at the channel wall.	92
Figure 39: Three-dimensional numerical simulation of a two droplet binning configuration. Sequence of images are listed for the non-electrified two branch microchannel (left), and the electrified two branch microchannel (right). Electrical potential distribution locations are in the same corners illustrated in figure 38.	95

LIST OF TABLES

Table 1:	List of relevant dimensionless numbers.	32
Table 2:	Physical properties of materials tested.	38
Table 3:	Summary of experimental setup components.	44
Table 4:	Summary of numerical boundary conditions.	45
Table 5:	Quantitative comparison between experimental and numerical droplets.	58
Table 6:	List of dimensionless hydrodynamic / electric force ratios for two-dimensional routing simulations, according to equation 25b.	88
Table 7:	List of dimensionless hydrodynamic / electric force ratios for three-dimensional routing simulations, according to equation 25b.	89
Table 8:	List of dimensionless hydrodynamic / electric force ratios for two-dimensional binning simulations, according to equation 25b. N/A values are due to the first droplet being binned at the first branch.	93
Table 9:	List of dimensionless hydrodynamic / electric force ratios for three-dimensional routing simulations, according to equation 25b. N/A values are due to the first droplet being binned at the first branch.	94

CHAPTER 1: INTRODUCTION

The production and manipulation of liquid droplet emulsions have been topics of great interest and investigation. Applying various fields to droplet producing devices has been shown to affect the droplet production characteristics in many different ways. The addition of an external force supplied by any energy field, be it electric, magnetic, gravitational, thermal, or acoustic, will affect the production of these droplets if strong enough. Given the ever growing list of applications for microliter and nanoliter sized liquid droplet emulsions, applying external fields to microfluidic devices has become of great interest to the scientific community because of the added control this may bring to producing droplets. Not all external force fields are able to be applied to every system, and the details surrounding the coupling of these fields with the equations governing the primary physics will continue to intrigue researchers for the foreseeable future.

Electrification has primarily been viewed as a way to obtain additional control over the production and behavior of liquid droplets, and offers yet another parameter to study for a given application. One of the unique aspects of manipulating droplets using an electric field is that the methods are physically unobtrusive to the flow field. For example, this means there does not need to be any physical contact with a liquid droplet in order to change its direction or shape. Another benefit to using an electric field is the availability of low cost electrical control devices, such as power supplies and electrical measurement instruments. The placement of electrodes can still prove to be costly, but new advances in this technology are allowing microfluidic devices with imprinted electrodes to be produced more economically each year.

There have been several theoretical, numerical, and experimental studies that explore the effects of applying an electric field to various fluid systems, which will be explored in detail in the next section, but none that focus specifically on droplet deceleration and pinning downstream from

a microfluidic T-junction with an externally applied electric field. Studies involving an externally applied electric field have been performed in co-flowing and flow focusing droplet systems, but not in T-junctions as of yet. It is thus the goal of this study to provide a comprehensive understanding that will help to fill this void.

CHAPTER 2: LITERATURE REVIEW

This section will include an overview of relevant topics and studies in the field of microfluidic droplet production, with and without electrokinetics. First, the production of droplets without electrification will be presented, and is offered to establish a general understanding of the basic physics and studies carried out in this field to date. The sections following will focus on electrokinetics, and are organized such that each subsection will cover the general concepts behind the phenomena that arise as a result of applying an electric field to droplet producing devices, as well as some key studies and applications.

Non-electrified Droplets

The production, manipulation, and optimization of microscale liquid droplets has been, and continues to be, one of the most popular fields in microfluidics research. However, before the application of an external field is employed to manipulate liquid droplet emulsions, a thorough understanding of the flow and interfacial physics that govern the production of liquid droplets must be obtained. Even if no external fields are applied to droplet systems, understanding and modeling the physics of two-phase droplet producing fluid flow still proves to be a challenging task.

Given the unlimited number of possible designs for microfluidic devices today, the geometry of a majority of these devices can be classified somewhere within the span of three basic configurations: co-flowing streams, flow-focusing devices, and cross-flowing streams [1]. In the first two types, the dispersed channel is aligned coaxially with the continuous phase, and the third type is usually some type of angled junction, with the T-junction and Y-junction being two of the most recognizable configurations. Using these three basic designs (depicted in figure 1), and with the continued

advancement of microfabrication technology, some fairly elaborate droplet producing microfluidic devices have been created, and continue to be the focus of several research studies. Christopher and Anna [1], Teh et al [8], and Seemann et al [9] all provide thorough overviews on the subject of droplet based microfluidics.

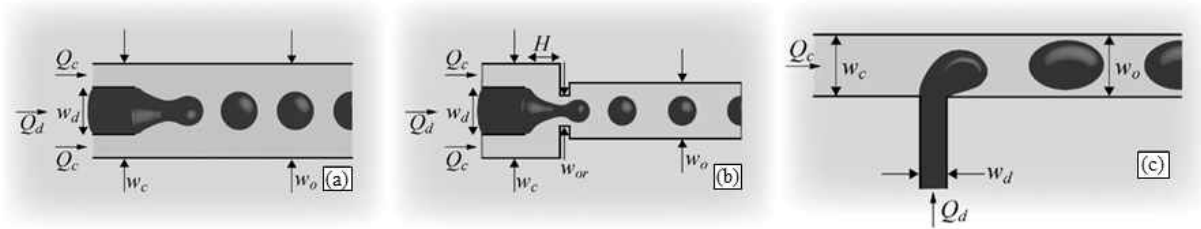


Figure 1: Schematic of three droplet production configurations: (a) co-flowing, (b) flow focussing, (c) cross-flowing - figure reproduced from [1].

Part of a chemical engineering research group, Thorsen et al was primarily interested in spatiotemporal pattern formation in their 2001 study [10]. However, this group was the first documented to observe droplet formation in a T-junction microfluidic device. Their experimental set-up contained a microfluidic device made from acrylated urethane (naturally hydrophilic surfaces), with channels approximately $60\mu m$ wide x $9\mu m$ high, in both square and rounded cross-section configurations. The channels also tapered down to $30\mu m$ in width (still $9\mu m$ high) where the T-junction occurred. An oil-surfactant mixture (Span 80) was used for the continuous fluid, while water was used for the dispersed fluid. The fluids were propelled by pressurizing their respective reservoirs, so observations were made specifically based on droplet patterns and their respective reservoir pressures. All droplets were unconfined by the channel, so the patterns took on various forms of clumping and staggering of droplets based on which pressure was higher (oil or water) and by how much. A pattern phase diagram was mapped based solely on observation of these droplet arrays and their reservoir pressures (similar to determining droplet formation regimes, which later became the focus of several future studies by other researchers, the details of which will be explained later). A

correlation was offered that estimated the droplet diameter based on interfacial tension, continuous phase viscosity, and shear rate, which accurately estimated the droplet diameter within a factor of two (when compared to actual droplet diameters). The authors claim that the two important effects that contribute to these droplet patterns include the motion of one fluid entraining the other, and the non-linearity in the equations of motion that arise from the boundary between the two fluids not being static. The non-linearity is prevalent even though the flow is technically at a low Reynolds number (and nonlinear inertial effects should be minimal).

Christopher et al [11] sought to model droplet production characteristics for two immiscible fluids at a T-junction for the transition region between the “squeezing” and “dripping” flow patterns. A wide variety of flow rate ratios, viscosity ratios, and channel width ratios were used. The continuous phase fluid was always silicone oil (viscosity range $6 - 350 \text{ mPa} \cdot \text{s}$, channel width $150 \mu\text{m}$), and the disperse phase was always deionized water (viscosity $1 \text{ mPa} \cdot \text{s}$, channel width range $65 - 375 \mu\text{m}$). Channel height was fixed at $50 \mu\text{m}$. Microchannels were fabricated out of poly(dimethylsiloxane) (PDMS) and baked to ensure hydrophobic wetting of surfaces. Specific characteristics measured were the droplet volume, production frequency, length, and to a lesser degree, flow pattern (dripping, squeezing, jetting). The authors also attempted to develop an “extended scaling model,” based on the original work of Garstecki et al [12], to better predict droplet characteristics at higher capillary numbers. A similar approach was used by Thorsen [10] and Husny and Cooper-White [13], where the droplet size is based on the balance of the three primary forces that govern the droplet breakup process: capillary force resisting deformation at the interface, viscous forces acting on the emerging droplet (not considered for very low Ca), and the squeezing force due to the buildup of pressure behind the droplet. Once detachment begins, the authors use arguments similar to Garstecki et al [12]. The model also includes the width ratio of the T-junction, which is a parameter not included in any model to date. The model predicts that the droplet volume depends both on capillary number and flow rate ratio, the trends of which were

corroborated with experiments.

Xu et al [14] produced a study where droplet flow patterns were analyzed for the authors' prior (3) works [15, 16, 17] in T-junction microchannels and compared to popular analytical scaling laws. Their work considered three separate flow patterns and were organized according to capillary number range. $Ca < 0.002$ was considered the squeezing regime (or droplet in channel - DC), $0.002 < Ca < 0.01$ was considered the transient regime, $0.01 < Ca < 0.3$ was considered the dripping regime (or droplet at T-junction - DTJ). The authors used experimental data from their prior experiments, where a capillary was inserted or "tapped" perpendicular to the main channel. In one study, the oil was dispensed perpendicularly into the flowing water, and in the other study, the fluids were reversed. However, the authors chose to always designate the water as the "dispersed" phase and the oil as the "continuous" phase, regardless of their flow orientation. In all other publications viewed, the continuous phase always designates the main flow channel (usually placed horizontally in figures), and the dispersed phase designates the perpendicular leg to this main flow channel, regardless of the fluid type in each of the respective channels. First the authors compared their data for the dripping regime to correlations provided by Thorsen et al [10], and found that by modifying the velocity used in the capillary number definition to account for the cross-sectional area blockage by the droplet (designated by u' and Ca'), correlations by Thorsen et al did in fact fit the data quite well. For the squeezing regime, correlations provided by Garstecki et al [12] fit the data very well. For the transient regime, correlations by Garstecki et al were modified by the addition of a capillary number term which, once the exponents and coefficients were determined, also fit the data very well. There was no mention of how to choose these exponents/coefficients, and the only explanation as to their different values was due to different flow geometries.

Efforts have also been made to numerically model droplet formation in a microfluidic T-junction using the lattice Boltzmann method (LBM). This mesoscale numerical method has the benefit of being applied to macroscale flow configurations while still retaining some of the powerful traits

of molecular numerical models without excessive computational requirements [18]. A study was carried out by Gupta et al [19] whereby droplet formation patterns were estimated using LBM based simulations in a T-junction. The authors primarily concentrated on observing the effects that modifying the flow rate ratio, viscosity ratio, and capillary number had on the normalized droplet volume and flow regimes. The regimes studied were denoted by DTJ - or “Droplet at T-Junction,” where the droplet forms primarily due to shearing from the cross flow, DC - or “Droplet in Channel,” where the droplet thread is allowed to protrude from the dispersed phase channel into the continuous phase channel before necking and eventual severing of the droplet, and PF - or “Parallel Flow,” where the dispersed phase fluid jets into the continuous phase channel and the results in a two-fluid flow configuration downstream of the T-junction. Results were also compared to theoretical models developed by Christopher [11]. It was found that as the capillary number increases, the band of flow rate ratios where DC flow occurs for a fixed viscosity ratio narrowed significantly. Also, as the viscosity ratio was decreased, the normalized droplet volume increased. A trend that was verified and compared with analytical models was that as the capillary number decreased, the normalized droplet volume increased.

Gupta and Kumar [20] also provided an analysis where droplet size characteristics (length and volume) were observed using lattice Boltzmann simulations in a T-junction. The results were compared to the numerical results and empirical correlations of Garsteki et al [12], and Christopher et al [11] (empirical correlations only). It is shown that the geometry independent correlations presented by Garsteki et al and Christopher et al do well when the capillary number is very low or when the flow rate ratio ($= Q_d/Q_c$) is less than 0.5, where Q_c and Q_d refer to the continuous and dispersed fluid flow rates, respectively. These correlations were also described as not taking into account the effect of the capillary number on the droplet size. Results indicate that droplet volume decreases with decreasing flow rate ratio and decreasing capillary number, trends that were also observed in the empirical correlations even though the LBM data do not match these correlations

very well. Another notable result were that for all flow rate ratios less than 0.2, the droplet lengths change very little and instead depend on the capillary number of the continuous phase following an asymptotic dependence. In addition, the channel depth was shown to play a key role in the resulting droplet size. The discrepancies between the correlations presented by Garsteki et al [12] and Christopher et al [11] and their work could also be because these correlations were developed only for cross-sectional aspect ratios of $\Gamma = h/w_c \leq 1$, where w_c and h refer to the continuous channel width and height, respectively. The general trend for increasing this ratio was that the droplet volume also increased. The subsequent explanation was that because the Laplace pressure difference (pressure required to push the protruding droplet against the downstream edge of the dispersed phase channel) across the interface of the two fluids increases when Γ is increased, the droplet lengthens to a greater degree before pinching off and traveling downstream.

Gupta and Kumar [21] also produced three-dimensional lattice Boltzmann simulations that were developed to observe the effects of adjusting two distinct parameters: the channel width ratio $\Lambda = w_d/w_c$ (by adjusting continuous channel width w_c , where w_d is the dispersed channel width) and the viscosity ratio $\lambda = \mu_d/\mu_c$ (by adjusting the continuous channel viscosity μ_c , where μ_d is the dispersed phase viscosity). The authors sought to characterize these effects around the framework established in a prior work, where the the droplet formation regimes were more clearly established: DTJ (dripping), DC (squeezing), and PF (streaming) [19]. After validating the LBM model using data from De Menech et al [22] and Christopher et al [11] for the normalized droplet volume versus capillary number (for two flow rates), it was verified that the critical value of the capillary number (from transition to dripping) depends of the viscosity ratio. Empirical correlations were offered to help determine this critical capillary number depending on the droplet generation regime. When the continuous channel width was increased (for constant capillary number, flow rate ratio, and viscosity ratio), the droplet frequency exhibited a very weak (increasing) dependency, where the volume exhibited a sharper (increasing) dependency. It was concluded that a major increase in

droplet volume could be gained by increasing the continuous channel width without altering the droplet frequency drastically. Another correlation was offered here to aid in the determination of the droplet volume (given the droplet frequency) for the DTJ flow regime. The range of capillary numbers considered in this correlation were relatively high ($0.1 \leq Ca \leq 0.7$), and the channel width ratio as $1/5 \leq \Lambda \leq 1/2$ (where $\Lambda = w_d/w_c$). The results of adjusting the viscosity ratio found that for a constant capillary number, channel width ratio, and flow rate ratio, the droplet frequency (volume) increased (decreased) as the continuous phase viscosity decreased (viscosity ratio increased). Concluding remarks regarding implementing these findings indicate that a higher rate of formation of droplets (increased frequency) is best obtained by decreasing the continuous phase viscosity, and not adjusting the channel width. However, adjusting the continuous channel width would be recommended to manipulate the droplet volume if a relatively stable frequency is desired. Experimental effects to the droplet formation regimes attributed to interfacial surface tension, viscosity ratio, and channel geometry were later investigated by Wehking et al [23].

Now that a basic overview of droplet production in the absence of external fields has been established, the application of an electric field, and the resulting behavior, referred to generally as electrokinetics, can be studied.

Electrowetting

Electrowetting refers to a phenomena whereby applying an electric field to a sessile droplet changes the droplet's contact angle with a surface. For a typical liquid droplet (such as water) resting on a typical solid surface with no applied electric field, the contact angle will be dependent on the net surface energy balance between the cohesion of the water molecules, and adhesion of these molecules to the solid surface. When surfaces are roughened or contaminated, the contact angle is normally large (usually 120° or greater) for a droplet with high surface energy, and the surface

is said to be hydrophobic, meaning the solid/vapor interfacial surface energy is very small when compared to the solid /liquid and liquid/vapor interfacial surface energies (the latter is also known as surface tension). By contrast, if the contact angle is small, say less than 90° , the surface is said to be hydrophilic, which means that the solid/vapor interfacial surface energy is a more formidable opponent to the solid/liquid surface energy and surface tension. Hydrophobic surfaces are “liquid-fearing” or “non-wetting,” and hydrophilic surfaces are “liquid-attracting” or “wetting.” One important aspect is that the determination of a hydrophobic/hydrophilic surface depends heavily on a fluid’s interaction with the surface, so that a surface is not deemed hydrophobic in and of itself, but rather with respect to a given fluid. For example, a surface can be hydrophobic to water, but not to some other type of liquid (such as fluorinet liquid), since the surface energy of water is much larger than the fluorinet liquid. Therefore, the surface in this example would be hydrophobic to water, but hydrophilic to the fluorinet liquid. The contact angle is described by the Young equation (equation 1), where the various energy terms can be seen to oppose each other (with θ denoting an angle and σ denoting surface energies). Subscripts sv , sl , and lv refer to solid-vapor, solid-liquid, and liquid-vapor respectively. It can be concluded from equation 1 that if the surface tension is high enough, the contact angle will always reduce to 90° .

$$\theta_{Young} = \arccos \left(\frac{\sigma_{sv} - \sigma_{sl}}{\sigma_{lv}} \right) \quad (1)$$

When an electric field is applied to the droplet, the electrical energy is working in conjunction with the surface energy to help the droplet wet the surface better, or to render the surface more hydrophilic with respect to a given fluid. Now, instead of the solid/vapor surface energy alone combating the liquid surface energies, the combined electrical/solid surface energy work against the liquid free surface energy. If the electric field is strong enough, the droplet will actually deform and wet the surface almost completely (or with close to a 0° contact angle). This modification to

the contact angle is explained by the Young-Lippmann equation, where θ and σ are as specified in equation 1 and η is the dimensionless electrowetting number [2].

$$\theta_{contact} = \arccos \left(\frac{\sigma_{sv} - \sigma_{sl}}{\sigma_{lv}} + \eta \right) \quad (2)$$

The tendency concluded from equation 2 will be for η to always increase the quantity within the “arccos” argument, and thus always decrease the overall contact angle. Figure 2 depicts a schematic of electrowetting.

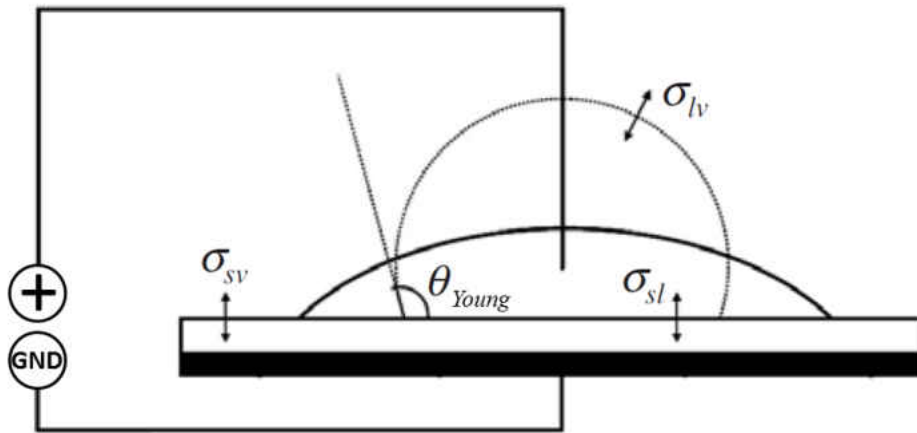


Figure 2: Example of electrowetting experiment - figure reproduced from [2].

Electrowetting is one of the mechanisms that contribute to electrocoalescence, whereby electrical forces allow the droplet to adhere more strongly to solid surfaces, thus getting trapped until another droplet collides and coalesces with it. More on this phenomena will be presented in later sections. A very recent and popularized application of electrowetting comes from the practice of

electrowetting on device (EWOD) whereby wetting of a given liquid can be controlled locally via deliberate placement electrodes. When an electric field is applied between these electrodes, the droplet passing through can be forced to wet one surface more than the others, or even propelled in prescribed paths based on the electrode shape. Once such experiment allowed Lee and Kim [24] to move a mercury droplet around a circular shaped track simply using EWOD, and another experiment allowed Gunji and Mashizu [25] to do something similar with a water droplet and an oval shaped track.

The physics up to this point has been very unidirectional, meaning that by applying electrical energy between a droplet and a solid surface, the droplet shape can be deformed due to electrowetting. Krupenkin and Taylor [26] decided to see if the reverse were possible, that is, to extract electrical energy from a droplet that is deformed by other mechanical means. The mechanical means they chose for deforming the drop was walking. A prototype of this technology has been incorporated into the soles of shoes to extract the mechanical energy produced from walking/running, and converting a portion of it into electrical energy via a process called reverse electrowetting (REWOD). This type of configuration, when applied over a large number of droplets (and steps), has shown to be quite effective at harvesting a usable amount of electrical energy (power densities up to 10^3 W/m^2) to charge/power a typical mobile consumer electronic device. This application has gained quite a bit of popularity due to its potential of providing battery powered mobile devices with an energy supply proportional to its user's frequency of steps.

Electrocoalescence

Electrocoalescence utilizes an externally applied electric field to assist in the coalescence (combining) of two or more liquid droplets. The mechanism can be put into practice a number of ways. One method includes the local trapping of a droplet in a channel via attractive electrical forces

(from an externally applied electric field). This trapping employs the concept of electrowetting to increase the surface energy, and thus decrease the contact angle, such that the droplet wets one (or more) of the channel walls much more than the others. Originally flowing down the channel, this first droplet is held in place via electrowetting until another droplet comes along and collides with it. Depending on the fluids' electrical properties and flow conditions, the impact of the second droplet on the first can cause coalescence of the two droplets, as well as break the newly formed single droplet free of any electrical trapping forces because of the momentum generated by the collision. The electrical parameters (electrode placement, geometry, field strength, etc.) can then be adjusted to provide a number of possible droplet combination outcomes, where more than two droplets are required before a trapped droplet will break free, or a double T-junction is used with an electrode at the junction to prevent the need for precise droplet formation synchronization. Figure 3 shows an experiment performed by Gu et al [3] in a double T-junction.

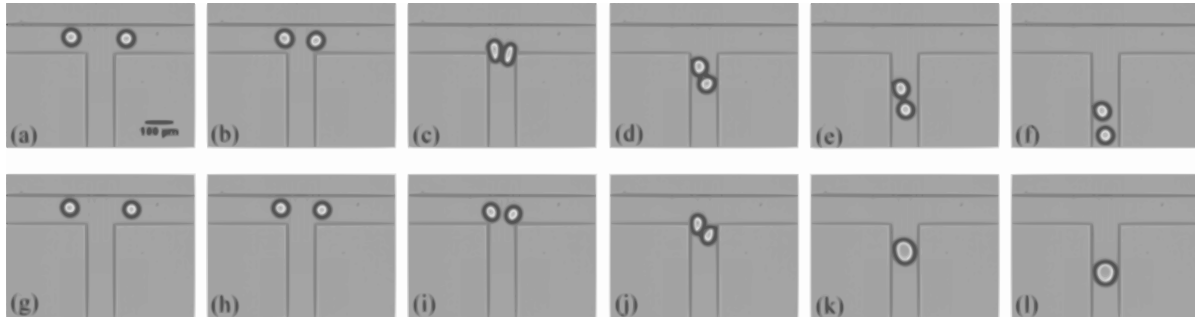


Figure 3: Electrocoalescence experiment performed by Gu et al [3]. Cells (a)-(f) depict flow with no applied electric field, and cells (g)-(l) depict flow with an applied electric field. Electrodes are located at the intersection between the three channel branches - reprinted from [3]

The method just described is typically utilized when the droplet size is the same order of magnitude as the channel, but a second method can be used when the droplet is much smaller than the channel. This method relies on the attractive force generated between the droplets as a result of polarization from the applied electric field. When the droplet boundaries meet, if the electric field is strong

enough, the electrical boundary forces will overcome the interfacial surface forces causing the boundaries to break down, and thus causing the droplets to coalesce. A selection of works by Zagnoni et al are offered to give some overview of typical studies into electrocoalescence.

Zagnoni and Cooper [27] set out to create an on-demand device (a switch) for electrocoalescence of droplets. Oil was used as the continuous phase, and water as the disperse phase, with a small patch of electrodes built into the bottom wall of a PDMS microchannel, in both a single and double T-junction configuration. The AC voltage range was 0 – 20 volts, at a frequency range of 0 – 100 kHz. The experimenters found that as the droplets passed through the section of the channel containing the electrode, depending on the droplet volume and velocity, it could get trapped over the electrode until another droplet came along and collided with it. This is the primary mechanism of coalescence. The authors found that the best conditions under which the droplets would merge predictably was when the droplet had a high velocity, and minimal separation from the electrode. The results were tested and verified on both the single and double T-junction channel configurations. The experimenters claim that this on-demand method of droplet coalescence was favored over other methods because it did not require careful alignment of the electrode, special synchronization of the double T-junction flow rates, or any permanent change to a portion of the microchannel.

Zagnoni et al [28] supplemented prior work by studying the effects of changing the shape of the microchannel electrode. Numerical analyses were performed to simulate the effects of the electric forces on the droplet in each of the coordinate axes. Numerical results showed that greater electrical forces can be applied (with less electrical potential) when the two poles of the electrodes were placed closer together. Overall results proposed two systems of droplet coalescence: one for two droplets in contact that coalesced after passing over the electrode, and one where droplets were separated by a portion of the continuous phase. The contact droplet system depended primarily upon the electric forces overcoming the interfacial surface tension between the droplets (separated

by layers of surfactant and continuous phase), where the separated droplet system depended upon the electric forces competing with the viscous forces of the continuous phase. Four different water/oil/surfactant combinations were tested using microchannels constructed from PDMS, where authors used an electrical potential between 0 – 20 volts for both single and double T-junction configurations.

Electrophoresis and Dielectrophoresis

This mechanism is the transport/migration of bodies through a fluid by means of an externally applied electric fields. Electrophoresis refers to body (most often solid particle) migration due to the existence of charge on the particle surfaces. These charges activate a Coulomb force on the particles, which must overcome the existing hydrostatic viscous forces, and cause these bodies to move while keeping the fluid stationary. The principle governing the movement behind electrophoresis and electroosmosis are identical, where there is simply a change of reference with regards to the relative motion and thus boundary conditions. In electrophoresis, an electric double layer (EDL) is formed around the charged submerged body due to the electrical properties of the body and surrounding liquid, whereas in electroosmosis, an electric double layer is formed at the walls of the flow geometry due to similar electrical interactions between the fluid, wall material, and the electric field. By contrast, dielectrophoresis, suggesting by name that dielectric behavior is at work, is the force resulting from polarization by an inhomogeneous electric field, with no charges present [29]. With no charges, there is no EDL, and the force is solely caused by dielectric polarization due to the presence of an electric field. Additional details regarding electrophoresis and dielectrophoresis can be found in a reviews by Seemann et al [9], Pethig [29], with Kirby providing more of a textbook style reference [4].

Electroosmosis

This phenomena results when bulk motion is induced in a conducting fluid simply by applying an electric field to the inlets/outlets of the flow system. The volumetric charge density is approximated by the Poisson-Boltzmann distribution of the electric field, with constant potential (φ) boundary conditions at the channel walls (designated as φ_0) described by the zeta (ζ) potential (where $\zeta = \varphi_0$). The zeta potential is a parameter that is highly dependent on the wall and fluid electrochemical material properties, and can change with different pairings of fluid/substrate combinations. The presence of an electric field activates the free electrons in a conducting fluid such that they congregate at the walls of a channel over time. Once the channel walls accumulate enough of these free electrons, there exists a thin layer, called the electric double layer (EDL), that activates fluid flow outside the EDL due to Coulomb forces within the EDL. One way to visualize this effect is to picture free electrons from the fluid trying to congregate at the wall of the channel, but being blocked and effectively “skipped along” downstream or upstream. While this is happening within the EDL, the net result is bulk fluid motion with a fairly uniform velocity profile. Usually, uniform velocity profiles are merely simplifying approximations since typical channel flows result in velocity profiles that are maximized at the center of the channel and zero at the walls (enforcing a no-slip condition). This is still enforced by electroosmotic flow, but the change of slope of the velocity profile occurs very sharply within the EDL itself, while still reducing to zero at the wall. Given that EDL sizes are typically less than a few hundred nanometers, the details of the velocity profile within this region may often not be desired. Therefore, instead of solving for the complete velocity profile from the fluid momentum equation, with the Coulomb body force included, an effective slip velocity boundary condition can be used. This boundary condition is called the electroosmotic slip velocity, and will also be the final bulk fluid velocity obtained once the flow is allowed to reach steady state. Since the velocity outside the EDL is uniform, this is effectively the velocity reached everywhere outside the EDL, and often a sufficient solution for most analyses.

The effects of this phenomena can be found in figure 4.

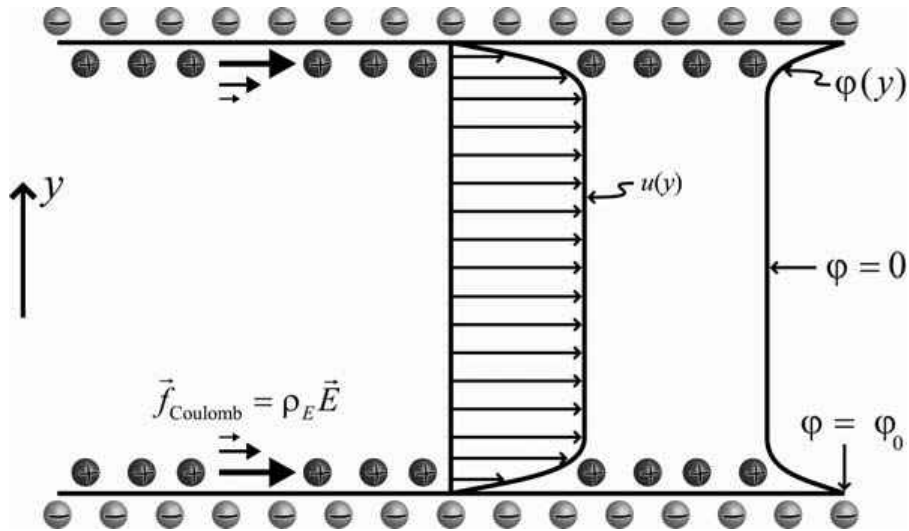


Figure 4: Potential distribution (φ) and resulting velocity profile (u) for electroosmotic induced flow - figure reproduced from [4].

A series of works produced by researchers at Nanyang Technological University in Singapore provide an excellent overview of electroosmotic flow. Gao et al [30] begins by providing an analytical solution to an immiscible two-fluid system between parallel plates. The idea is to illustrate the capability of delivering a non-conducting fluid using a conducting fluid via electroosmosis of the conducting fluid alone. The effect is analogous to moving the plate in contact with the conducting fluid at a constant velocity, thereby simulating the electroosmotic velocity at that wall, and observing how the second (non-conducting) fluid is brought to flow as a result of the shearing of the shared boundary. As a validation, the limiting case of infinite fluid viscosity was applied to the non-conducting fluid and was shown to be in agreement with single fluid electroosmosis solutions. Later on, Li et al produced analytical solutions for a three immiscible fluid system under the combined effects of electroosmotic/pressure driven flow, for both steady [31] and time dependent studies [32]. This proved to be quite an accomplishment considering all of the complex mathematics necessary. The group then demonstrated, both theoretically and experimentally, the ability

to route non-conducting droplets using sheaths of conducting fluid solely by adjusting the applied electric field on the conducting fluid streams [33]. The droplet could be routed from a single inlet branch into one of five possible branches of a microfluidic system for a given flow rate simply by manipulating the electrical properties. This was deemed a valveless microfluidic switch, and was shown to be quite effective and precise at routing continuous droplet streams.

Deforming Stationary Droplets in an Electric Field

This field has been investigated quite actively and thoroughly since the 1960's. Initially, experimenters thought that fluids behaved in one of two ways: either as a perfect conductor or perfect dielectric. As a perfect conductor, a fluid contains free electrons that provide a means for electrical current to flow through the liquid in addition to its inherent polarity as a substance. No electric field would be present within the conducting liquid though since it is, in fact, considered a perfect conductor; charge distributes equally and instantaneously with no gradient of electrical potential. As a perfect dielectric, the liquid contains no free electrons, and thus does not allow electrical current to flow through it. The liquid is still polarized, however, and produces a dipole moment when charged. Given these two basic models for charged liquids, and applying a stress balance to an immiscible droplet submerged in another fluid, the droplet would deform into a prolate spheroid (a spheroid elongated in the direction parallel to the applied electric field). This prolate spheroid was expected when either a conducting or non-conducting liquid droplet was submerged in another a non-conducting liquid bath [34]. However, when Allan and Mason [35] tested some poorly conducting fluids in 1962, they discovered that some of their results behaved in accordance with the accepted theory and deformed into prolate spheroids, while others deviated from the theory and deformed into oblate spheroids (a spheroid elongated in the directions perpendicular to the applied electric field). Examples of prolate and oblate spheroids (represented as 2D ellipsoids) can

be found in figure 5.

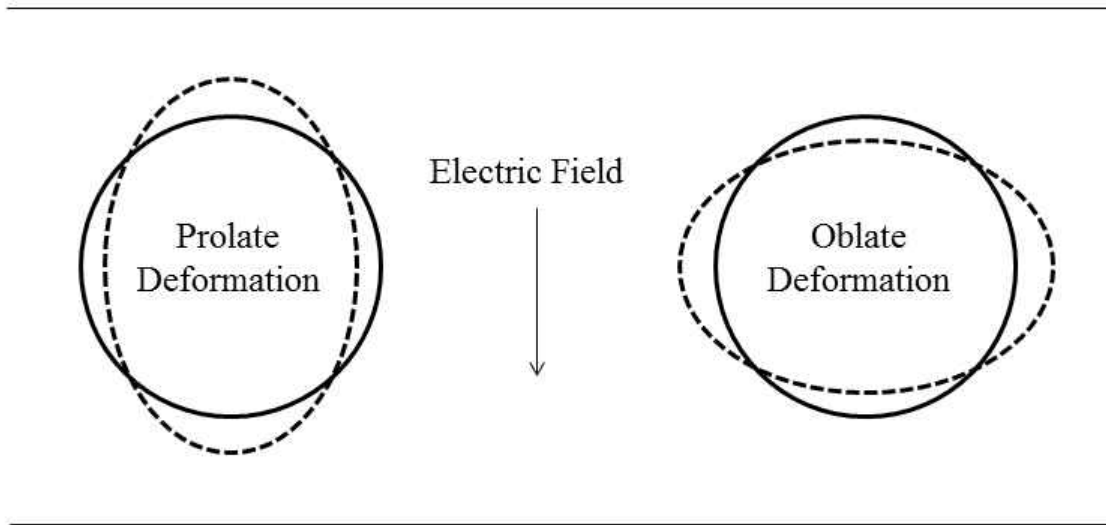


Figure 5: Observed (stationary) droplet shapes under an applied electric field.

Taylor [36] then found that by factoring in the liquids' conductivities into the stress balance of the deforming droplet, he could have cases where the droplets would deform into oblate spheroids. In this same work, Taylor established a discriminating function that could predict when a droplet submerged in another liquid would become oblate or prolate based on the ratios of conductivity, permittivity, and viscosity between the two fluids (drop and surrounding medium), as well as quantify the amount of deformation from an ideal sphere. What was missed in prior models was imbalance of charge at the surface shared by the two fluids, which induced a toroidal circulation in the liquid droplet that depended on the ratio of fluids' electrical and hydrodynamic properties. This implied that when droplet and surrounding fluid pairs with very little conductivities ($\ll 1 S/m$) were allowed to stabilize after being exposed to an electric field, the fluids could not fully be approximated as dielectrics, but instead must be modeled with these finite conductivities having an

effect on the overall stress balance at the interface. The Taylor-Melcher “leaky-dielectric” model was born and was fully outlined by Melcher and Taylor [37] and later by Saville [38]. This began an onslaught of studies to verify the applicability and accuracy of the proposed theory that continues to this day. Torza et al. [39] was one of the first thorough and complete attempts to verify Taylor’s findings experimentally, and, in addition to testing using steady (DC) electric fields, expanded the scope of his study to include electrification via AC electric fields as well. While Taylor’s discriminating function appeared to accurately predict when a droplet would become oblate or prolate, the amount of deformation did not match very well between experiments and theory. A thorough attempt at reconciling the quantitative differences between theory and experiments was performed by Vizika and Saville [40]. After experimental results were found to not agree with well quantitatively with Taylor’s leaky dielectric theory, with one of the primary causes speculated as inaccurate values used for material properties (conductivity, permittivity, etc.), Vizika and Saville set out to remove as much doubt as possible from the material properties by directly measuring as many as they could. While the results did improve, discrepancies still remained.

With the birth of high performance computing came another wave of analyses that focused on validating the Taylor-Melcher leaky dielectric model using computational fluid dynamics (CFD). One major benefit to modeling the system numerically was that non-linear governing equations could be solved without any (or with very little) simplifications. This ensured that discrepancies due to approximations/simplifications could be ruled out when comparing to theory and/or experiments. A drawback that was quickly found was the instabilities and inaccuracies that may result due to nature of numerical techniques and solvers. Numerical analysis of deforming droplets appears to have started with Sherwood using a boundary integral technique [41], and later Feng and Scott using a Galerkin-finite element method [42]. More recent studies were carried out by Hua et al using finite volume/front tracking methods [43], Lin et al using the phase field [44] and level set methods [45], and Lopez-Herrera et al using volume-of-fluid/front tracking [46]. The study by

Lopez-Herrera et al also included a generalized treatment of the electrical properties of the two fluids, such that the distinction of a particular fluid as a perfect dielectric, perfect conductor, and/or leaky dielectric in the numerical model was not necessary. As an example of a typical numerical study investigating the deformation of a stationary droplet under an applied electric field, the following summary is offered.

Zhang and Kwok [47] utilized the lattice Boltzmann method (LBM) to study steady droplet deformations under an applied electric field. The mesoscale LBM equations were modified to include forces/stresses from an electric field using the Taylor-Melcher leaky dielectric model, and was applied to a two-phase fluid flow. The leaky dielectric model incorporates the Maxwell stresses into the Navier-Stokes equations for fluid flow. The authors validated their LBM code using a theoretical droplet diameter deformation equation from Feng [48] for a fluid droplet immiscibly suspended in another fluid. The theoretical model by Feng, as with aforementioned models presented by Taylor and others, was derived based on small droplet deformations, so for larger deformations, the LBM code deviated slightly higher than Feng's model. However, the model agreed well at smaller deformations. The authors also validated their modified LBM code on velocity profiles for droplets flowing immiscibly in another fluid, again with a theoretical analysis by Feng. They found relatively good agreement within the droplet, but not so good agreement at the droplet interface and outside the droplet. This is primarily because of the boundary conditions in LBM requiring that the velocity go to zero at the walls, where the theoretical model requires an infinite distance for the velocity profile to decay to zero. The LBM scheme also showed some (somewhat asymptotic) deviations at the droplet interface that others have also reported for LBM. No definitive conclusions have been offered for this behavior.

Electrified Flowing Droplets

Both experimentation and simulation in this field is relatively new given the recent arrival of low-cost microfluidic devices and the arrival of high performance computing systems. A system containing two-phase flow coupled with effects from an electric field can contain electrokinetic phenomena from a number of the topics discussed in prior sections, with effects often occurring simultaneously. The electrical properties of the fluids and parameters/placement of the electric field can usually help determine the type of effects being exhibited by the system, but accurate numerical modeling and precise control of experiments still prove to be a challenging task given its vast complexity. The system can be further expanded by varying the flow geometry to contain various droplet producing features such as flow focussing nozzles, single/double T-junctions, and Y-junctions of varying angles. While the individual components of electrokinetics mentioned above are still under much interrogation, there is an endless combination of geometric features and electrode placements that will allow users to fine tune a system in any way necessary to obtain the desired outcome.

Sato et al [49] investigated the effects of electrification on co-flowing immiscible fluids with respect to uniform droplet formation. The apparatus consisted of a tank of the continuous phase fluid (deionized water). A nozzle dispensing the disperse phase fluid (kerosene) was located at the bottom of the tank, and was surrounded by a positively charged electrode. The negatively charged electrode (or “Earth electrode”) was located about 10mm above the positively charged plate. There was also an inlet for injection of continuous fluid at the bottom of the tank, configured such that the two fluids co-flowed through a restrictor plate (which also acts as an insulator between the two electrodes) before passing the “Earth electrode.” The group excited the flow using three types of electrification techniques: direct AC at a specified frequency, AC/DC superimposed at a specified frequency, and pulsed DC. Experiments were carried out by first keeping the frequency constant

($4kHz$) and varying the voltage, and then keeping the voltage constant (240 volts) and varying the frequency. Finally, the flow rate ratio was adjusted and droplet diameter changes were noted. The classical model that governs surface wave behavior on laminar jets was developed by Rayleigh. This phenomenon presented itself as expected before any voltage was applied, but after voltage was applied (and in specified ranges of voltage and frequency), synchronous droplet formation occurred. This is when uniform droplets are formed that are synchronized with the surface wave frequencies. Not much difference was seen between the three types of applied voltages, but the lower limit of synchronous voltage was plotted against the applied frequency to show the types of droplet formation. In addition, droplet diameters were shown to change based on the flow rate ratio of the two fluids. Finally, the droplet diameter was shown to be more consistent in size (1.5% variation) when the voltage was applied than when not applied (6.1% variation).

Fernandez and Tryggvason [50] numerically simulated droplet migration and behavior in both stationary, and simple Poiseuille flow for several droplet/medium fluid combinations. After first validating their numerical model against existing results following the Taylor-Melcher leaky dielectric theory for deforming droplets, they observed the behavior of multiple droplets in a non-flowing channel. The results of this study indicated a dependency on where the droplets started in the domain, as well as the electrical properties of the droplets. For cases where the time evolution produced oblate droplets, multiple polarized drops would attract each other due to dielectrophoretic forces if started close enough to each other at the beginning of the simulation, or migrate to the walls if started too far apart. Prolate droplets, by contrast, would try to repel each other due to the circulating viscous fluid motion. Simulations including several oblate drops would eventually form chains that spanned the width of the channel in the direction of the applied electric field. When a low pressure driven (Poiseuille) flow was added, the droplet chains would break, but would still collect at the walls leaving the center of the channel clear. As the flow rate increased, fewer drops cling to the walls until the fluid shear is strong enough to completely prevent droplet adherence to

the channel walls. This competition between electrostatics and fluid shear depends on the electrical/mechanical properties of the fluids, as well as the channel geometry, electric field strength, and flow parameters. One effect that was not modeled, but would eventually occur is electrocoalescence, where the droplets collecting at the channel walls would combine and produce a three fluid layer flow field.

Singh and Aubry [51] performed an experimental and numerical analysis of droplets flowing over a two electrode configuration where both the positive and negative electrodes were located on the same channel wall, and positioned very close to each other. This type of configuration simulated a smoothed step function in the electric potential at the wall. The fluids were both modeled as perfect dielectrics in an effort to show the effects of a dielectrophoretic force on the droplets. A finite element analysis was used employing the level set method (for capturing the interface) for the direct numerical simulations (DNS). Since dielectrophoresis typically refers to particle motion induced by dielectric forces, a distinction was highlighted in this study that in addition to migration of the “droplet particles,” there was also deformation of the liquid droplets that is not typically found in common purely dielectrophoretic studies. Only qualitative similarities were found between numerical simulations and experiments using glycerin (droplet fluid) and silicone oil (suspending medium fluid). Droplet capturing and deformation due to dielectrophoretic forces was demonstrated (though this could also be due to some electrowetting in experiments, as electrowetting was not modeled numerically) and when two droplets were placed on the electrodes, they would coalesce once the electric field was strong enough. The interfacial surface tension was then reduced so that droplet stretching could be simulated numerically.

Gong et al [52] modified LBM in a similar manner to Zhang and Kwok [47], and applied the model to a co-flowing microchannel configuration. Model validation was also carried out using the Laplace equation for validation of surface tension. Efforts were concentrated on mapping the streamlines and the difference between the pressure inside the droplet and pressure outside the

droplet just after the central channel exit plane (see figure 3 in [52]). The minimum distance between the droplet and the wall was also measured for varying capillary numbers (flow rates) and applied electric fields. Changing the capillary number seemed to have an effect on this minimum distance when no electric field was applied, and also when the electric field was below a critical value. Once the electric field was increased up to (or past) the critical value, the droplet would be in direct contact with the walls containing the electrodes, and further increasing the capillary number had little to no effect on the droplet diameter or formation frequency. This is reasoned to be because of the effective “blockage” the droplet creates due to filling the entire channel, and the resulting added pinching on the droplet’s back side because of this increased pressure.

Now that an overview of the relevant studies in electrohydrodynamicis has been covered, the formulation of the problem examined in this study can be outlined.

CHAPTER 3: THEORETICAL MODEL

This section will include the fundamental theory and governing equations. The flow will be modeled as a two-phase flow system using two immiscible fluids in a microfluidic T-junction. The equations of continuity (equation 3) and momentum (equation 4) will describe the flow.

Fluid Mechanics

$$\frac{\partial \rho}{\partial t} + \nabla \cdot (\rho \mathbf{v}) = 0 \quad (3)$$

$$\frac{\partial(\rho \mathbf{v})}{\partial t} + \rho(\mathbf{v} \cdot \nabla) \mathbf{v} = \nabla \cdot [-p \mathbf{I} + \mu(\nabla \mathbf{v} + (\nabla \mathbf{v})^T) + \boldsymbol{\sigma}^M] + \gamma \kappa \delta \hat{\mathbf{n}} + \rho g \hat{\mathbf{n}}_g \quad (4)$$

ρ Density	$\boldsymbol{\sigma}^M$ Maxwell stress tensor
\mathbf{v} Velocity field	γ Interfacial surface tension
t Time	κ Shape function (interface curvature)
p Pressure	δ Dirac-delta function
\mathbf{I} Identity matrix	$\hat{\mathbf{n}}$ Normal vector of the fluid interface
μ Dynamic viscosity	g Gravity
	$\hat{\mathbf{n}}_g$ Gravitational unit vector

The momentum equation (equation 4) contains an additional term in the stress tensor due to the presence of an applied external electric field acting on the fluid. In most macroscopic flow studies, the influence of a typical external electric field on a flowing fluid can safely be neglected, as shown by a simple order of magnitude analysis (similar to that found in table 1, shown later). This force

must be accounted for as the flow scale decreases, as externally applied electric fields (even when relatively “weak”) can have a more significant effect on a flowing conducting fluid, especially when considering a multi-phase (immiscible) flow case.

There is also a force term accounting for the surface tension between the two immiscible fluids (last term of equation 4). Since this two-phase fluid model is being observed at such small scales, the effects from the capillary forces must be accurately accounted for in the momentum equation. Droplet formation at the microfluidic T-junction is the purpose of the microchannel design, and the interfacial surface tension between the two fluids is a vital mechanism for droplet production at these scales.

Electric Field

Electric Field/Potential:

$$\mathbf{E} = -\nabla\psi \quad (5)$$

Charge Conservation:

$$\frac{\partial q^f}{\partial t} + \mathbf{v}\nabla q^f = -\nabla \cdot (\sigma\mathbf{E}) \quad (6)$$

Gauss’s Law:

$$\nabla \cdot (\epsilon\epsilon_0\mathbf{E}) = q^f \quad (7)$$

Maxwell Stress Tensor [38]:

$$\boldsymbol{\sigma}^M = \epsilon\epsilon_0\mathbf{E}\mathbf{E} - \frac{1}{2}\epsilon\epsilon_0 \left[1 - \frac{\rho}{\epsilon} \left(\frac{\partial\epsilon}{\partial\rho} \right) \right] (\mathbf{E} \cdot \mathbf{E})\mathbf{I} \quad (8)$$

\mathbf{E}	Electric field	σ	Electrical conductivity
ψ	Electric potential	ϵ	Relative permittivity
q^f	Free charge density	ϵ_0	Vacuum permittivity

Proper modeling of the electric field depends on the application and level of accuracy desired. As stated earlier, if precise droplet deformation in response to an applied electric field is the focus, Taylor's leaky dielectric model should be utilized because all liquids have a finite conductivity, even if they are relatively small. With this theory, tangential and normal stresses between the two fluids exist and must be properly considered. Ohmic conduction causes charge to accumulate at each of the fluid interfaces, and the mismatch in charge creates a tangential stress that must be balanced somehow. Hydrodynamics provides the balance, and circulating fluid motion is the result. Normal stresses at the fluid interfaces are also present, and result because of a mismatch in dipole moments in each of the fluids. When solving the equations governing the electric field in the leaky dielectric model, the free charge will eventually collect at the surface and reach steady state. It is therefore appropriate (when modeling mathematically and numerically) to neglect the presence of free charge in the bulk of each of the respective fluids, solving equation 6 as $\nabla \cdot (\sigma \mathbf{E}) = 0$ for the potential distribution. In a perfect dielectric, where there are no free electrons to cause a net charge accumulation, the fluids respective dipole moments are the only cause of stress at the interface, thus the stress at the interface must be only directed normal to the interface surface. Under this model, there is no free charge density because of the absence of free electrons, and thus the free charge density everywhere is zero by definition. It is therefore appropriate to find the potential distribution under this model using equation 7 as $\nabla \cdot (\epsilon \mathbf{E}) = 0$.

When the divergence of the Maxwell stress tensor ($\mathbf{F}_M = \nabla \cdot \boldsymbol{\sigma}^M$) is carried through to obtain the

electric body forces, the resulting form is then included in the momentum equation:

$$\mathbf{F}_M = \nabla \cdot \boldsymbol{\sigma}^M = q^f \mathbf{E} - \frac{1}{2} \mathbf{E} \cdot \mathbf{E} \nabla \epsilon + \nabla \left(\frac{1}{2} \mathbf{E} \cdot \mathbf{E} \frac{\partial \epsilon}{\partial \rho} \right) \quad (9)$$

The first term results in the Coulomb force (after applying equation 7). This resulting force illustrates a direct result of how the charge accumulation at the fluid interfaces affect the fluid flow. This term need only be considered if there is charge accumulation at the fluid interfaces, and if there is an electric field present to activate this charge. The resulting forces at the interfaces contain both tangential and normal components, but the tangential component is responsible for the toroidal fluid circulation. The second term is the dielectric force, which is only evident when there is a mismatch in dipole moments somewhere in the domain, and is illustrated mathematically by the gradient of the permittivity ($\nabla \epsilon$). This term will always be considered when immiscible fluids of differing permittivities are allowed to interact in the presence of an electric field. Since the force is activated at when there is a gradient of permittivities, this force will act normal to the interface shared by the two fluids, and always in the direction from the fluid of higher permittivity to the fluid with lower permittivity. The third term is the electrostriction force, and if the fluids' electrical properties are constant with respect to its physical properties, this term can be safely neglected (since $\frac{\partial \epsilon}{\partial \rho} = 0$ in each of the respective fluids). As per explanations presented earlier, if the fluids are incompressible and are both considered under the perfect dielectric model, the first and third terms can be neglected. If the fluid are incompressible and are both considered under the leaky dielectric model, only the third term can be neglected. If there is any combination of leaky dielectric, perfect dielectric, and/or perfect conducting fluids, special care must be taken to include the necessary terms in this body force.

Another parameter of interest when determining the electrical effects each fluid bring to the resulting analysis is the electrical relaxation time, $t^E = \epsilon/\sigma$. The result will indicate the time necessary

for the charge to migrate and equilibrate in the fluid. By comparison, the viscous relaxation time ($t^v = \rho l_{ref} / \mu$) is the relative time necessary for the system to evolve hydrodynamically. If $t^E \ll t^v$, the electric field will develop much much faster than the flow field, and vice versa if $t^E \gg t^v$. If $t^E \ll t^v$, charge migration and accumulation is considered much much faster than any flow field development, and fluids should be modeled to account for the resulting force without any temporal dependencies, as is done in the leaky dielectric model. If the opposite is true, or $t^E \gg t^v$, then the flow field develops much much faster than the electric field, and charge may not have enough time to accumulate before the fluid passes out of the electric field (by flow convection, for example). In this case, the resulting force induced by this charge is not present, and thus should not be modeled, as is done in the perfect dielectric model. For the majority of studies performed in this work, the continuous fluid is silicone oil and the dispersed fluid is deionized water (see table 2). Studies by Zholkovskij et al [53] showed that for this fluid pairing, droplets of radius $r \leq 5 \times 10^{-8}m$ (or $r \leq 50nm$) followed behavior consistent with the perfect dielectric theory, and droplets of radius $r \geq 2 \times 10^{-6}m$ (or $r \geq 2\mu m$) followed behavior consistent with the leaky dielectric theory. Given that all droplets under consideration in this work are $r > 30\mu m$, the leaky dielectric model will serve as the governing theory for this fluid pair.

Normalization

All variables are normalized using the following characteristic scales:

$$\mathbf{r}^* = \frac{\mathbf{r}}{l_{ref}} \quad t^* = \frac{t}{l_{ref}/v_{ref}} \quad \mathbf{v}^* = \frac{\mathbf{v}}{v_{ref}} \quad p^* = \frac{p}{\rho_{ref}v_{ref}^2} \quad \mathbf{E}^* = \frac{\mathbf{E}}{E_o} \quad \kappa^* = \frac{\kappa}{l_{ref}}$$

$$\delta^* = \frac{\delta}{l_{ref}} \quad \rho^* = \frac{\rho}{\rho_{ref}} \quad \mu^* = \frac{\mu}{\mu_{ref}} \quad \epsilon^* = \frac{\epsilon}{\epsilon_{ref}} \quad \sigma^* = \frac{\sigma}{\sigma_{ref}} \quad \psi^* = \frac{\psi}{V_o}$$

When the two immiscible fluids are incompressible with constant physical and electrical properties, as well as zero bulk free charge density, the normalized equations reduce to:

Continuity:

$$\nabla \cdot (\rho^* \mathbf{v}^*) = 0 \quad (10)$$

Momentum:

$$\begin{aligned} \rho^* \frac{\partial \mathbf{v}^*}{\partial t^*} + \rho^* (\mathbf{v}^* \cdot \nabla) \mathbf{v}^* = & -\nabla p^* + \frac{1}{Re} \nabla \cdot \mu^* (\nabla \mathbf{v}^* + (\nabla \mathbf{v}^*)^T) \\ & + \frac{1}{Eu_e} \nabla \cdot \epsilon^* [\mathbf{E}^* \mathbf{E}^* - \frac{1}{2} (\mathbf{E}^* \cdot \mathbf{E}^*) \mathbf{I}] \\ & + \frac{1}{We} \kappa^* \delta^* \hat{\mathbf{n}} + \frac{1}{Fr^2} \rho^* \hat{\mathbf{n}}_g \end{aligned} \quad (11)$$

Electric field:

$$\text{Leaky Dielectric: } \nabla \cdot (\sigma^* \nabla \psi^*) = 0 \quad (12a)$$

$$\text{Perfect Dielectric: } \nabla \cdot (\epsilon^* \nabla \psi^*) = 0 \quad (12b)$$

The form of using equation 11 depends on the system being analyzed. equation 11 compares the relative strength of all forces with respect to the fluid inertial forces, while other forms compare the relative strength of these same forces with respect to different forces. Different formulations may help to simplify (or even eliminate) various terms for approximation purposes or parametric studies, and may also assist in stability of numerical implementation. Aside from which formulation is used, the relative interplay of various forces can always be monitored and adjusted to highlight different aspects of the system. Table 1 depicts the relevant non-dimensional numbers that may be

Table 1: List of relevant dimensionless numbers.

Number	Form	Ratio of Effects	Value Range*
Reynolds	$Re = \frac{\rho_{ref} v_{ref} l_{ref}}{\mu_{ref}}$	Inertial / Viscous	0.01 – 1.25
Froude	$Fr = \frac{v_{ref}}{\sqrt{g l_{ref}}}$	Inertial / Gravitational	0.02 – 6.83
Bond	$Bo = \frac{\rho_{ref} g l_{ref}}{\gamma}$	Gravitational / Interfacial	$2.6 \times 10^{-3} - 0.02$
Weber	$We = \frac{\rho_{ref} v_{ref}^2 l_{ref}}{\gamma}$	Inertial / Interfacial	$5.4 \times 10^{-6} - 0.12$
Capillary	$Ca = \frac{We}{Re} = \frac{\mu_{ref} v_{ref}}{\gamma}$	Viscous / Interfacial	$3.9 \times 10^{-4} - 0.10$
Electric Euler	$Eu_e = \frac{\rho_{ref} v_{ref}^2}{E_o^2 \epsilon_0 \epsilon_{ref}}$	Inertial / Electric	$5.1 \times 10^{-9} - 838$
Electric Capillary	$Ca_e = \frac{We}{Eu_e} = \frac{E_o^2 \epsilon_0 \epsilon_{ref} l_{ref}}{\gamma}$	Electric / Interfacial	$1.4 \times 10^{-4} - 2872$
Mason	$Ma = \frac{Eu_e}{Re} = \frac{\mu_{ref} v_{ref}}{E_o^2 \epsilon_0 \epsilon_{ref} l_{ref}}$	Viscous / Electric	$3.7 \times 10^{-7} - 670$

*Based on silicone oil/deionized water (continuous/dispersed) fluid pair.

applicable to this system, with their most frequently used mathematical form, general qualitative relation between effects, and a quantitative range based a typical system of fluids. The table lists the dimensionless numbers in order of potential impact to the overall system, starting with the smallest and ending with the greatest. The order (and placement of the horizontal dividing lines) is based on the extrema observed for each quantity considering all geometric and flow parameters (but keeping the physical properties of the two fluids fixed), as well as the range of orders of magnitude spanned.

CHAPTER 4: MATERIALS AND EXPERIMENTAL SET-UP

This section will include figures and details pertaining to the experimental setup and microfluidic T-junction channel construction.

Microchannel Material

Poly(dimethylsiloxane), also known as PDMS, was chosen as the microchannel material. This material is a type of two-part polymer that is mixed and cured to produce a transparent elastomer. PDMS offers many advantages as a microfluidic device due to its inert physical properties (thermally, electrically, and chemically), pliability (reversible deformation and conformance to non-planar surfaces), portability, reversible sealing properties to other materials and itself, optical transparency down to $280nm$, and relatively low manufacturing costs [6]. The bulk material is also naturally hydrophilic to aqueous solvents, meaning these liquids will have contact angles greater than 90° with the microchannel surfaces as they flow downstream. This state makes the PDMS microchannels ideal for producing aqueous liquid droplets. However, part of the microchannel bonding process includes treatment with plasma that causes the channel surfaces to become hydrophilic (contact angles $< 90^\circ$). In order to make aqueous liquid droplet emulsions submerged in oil, the contact angle between the aqueous liquid and microchannel walls must be larger than 90° (hydrophobic), otherwise the droplet interface curvature would invert, forming droplets in the oil instead. Therefore, the naturally hydrophobic PDMS surfaces, which were made hydrophilic by the plasma bonding process, need to be treated to render them hydrophobic once again. The fabrication process will be outlined next, which includes steps to treat the microchannel surfaces in order to render them hydrophobic to aqueous liquids.

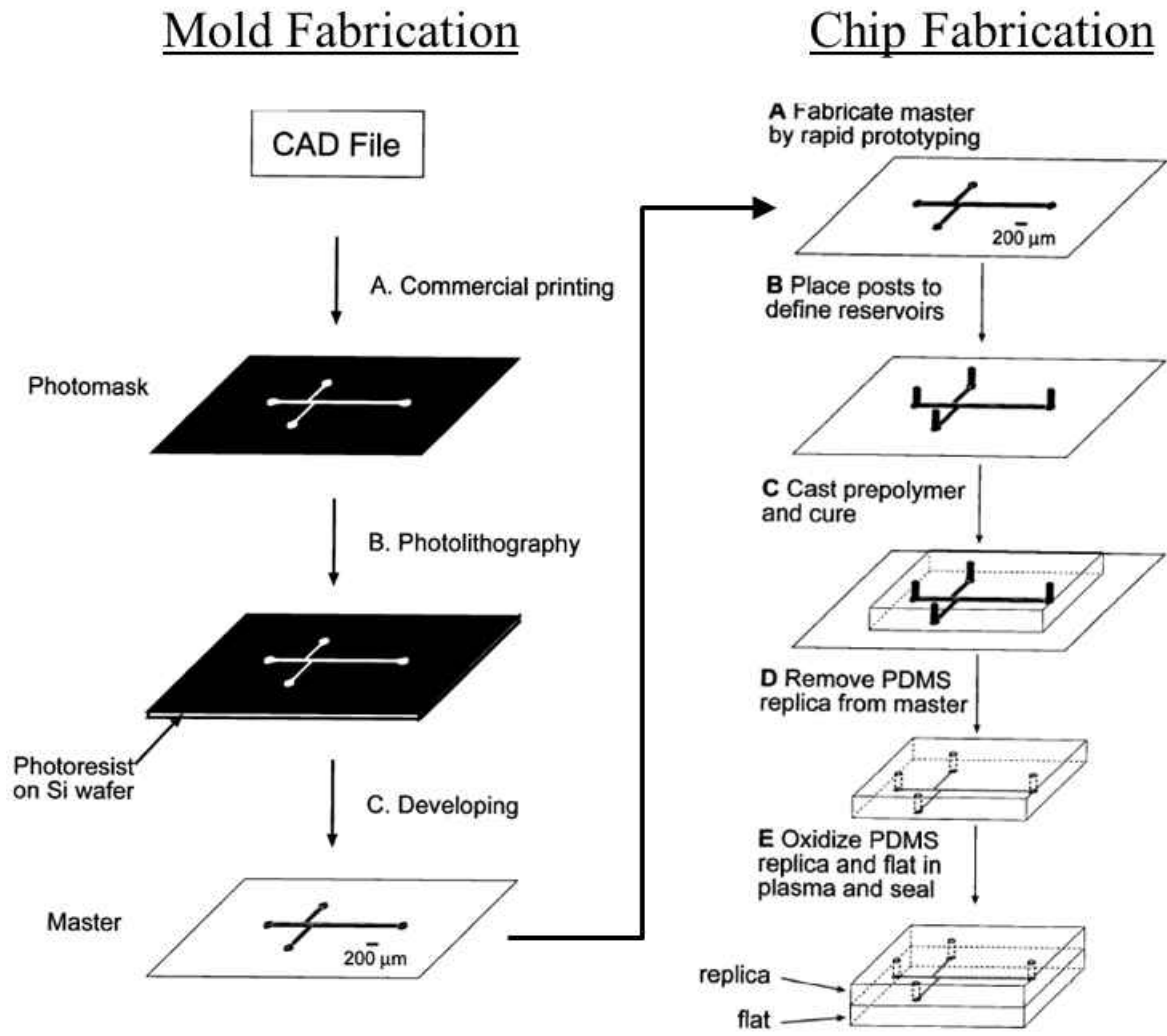


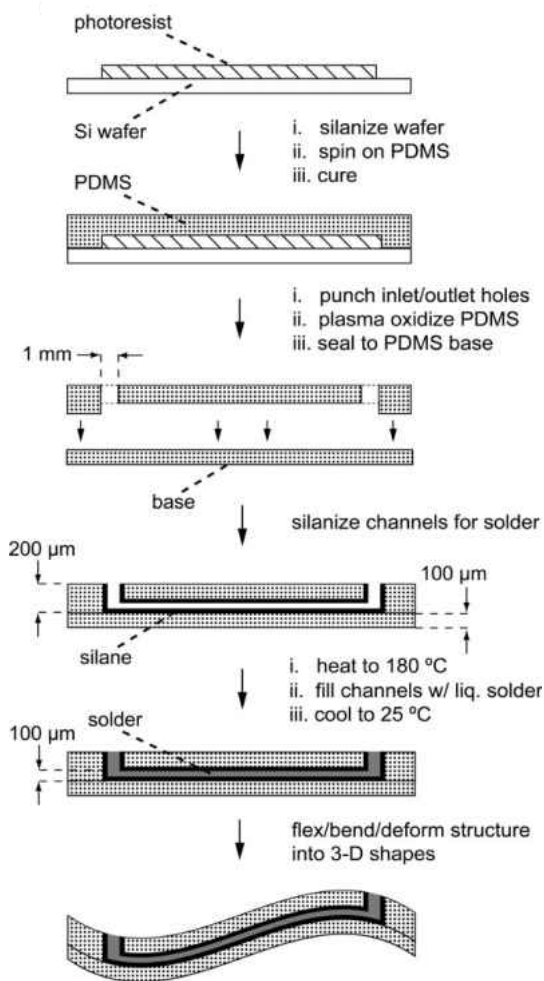
Figure 6: PDMS microchannel fabrication steps - adapted from [5, 6].

A flowchart of the fabrication process can be found in figure 6. First, a two-dimensional CAD file is created containing the planar features of the microchannels desired. Next, a high resolution 1:1 printout of the CAD file ($> 20,000$ dpi) is printed on a transparent film, as shown in (A) of “Mold Fabrication” in figure 6 (left column). Then, a silicon wafer is coated with photoresist, and exposed to an ultraviolet (UV) light source covered by the transparency “photomask.” The photomask acts as a type of filter to the UV light source, blocking light where the ink is solid on

the transparency, and letting light shine through the blank portions of the transparency. The UV light cures specific portions of the photoresist coated silicon wafer, and the remaining uncured photoresist is removed. What is left over is the master mold: a silicon wafer with cured photoresist “protrusions” which are the microchannel features, the height of which are determined by the initial height of the uncured photoresist, and exposure time and intensity of the UV light. Starting from this master mold, as shown in (A) of “Chip Fabrication” of figure 6 (right column), any number of microchannels can be made provided the integrity of the cured photoresist protrusions remain intact. Part (B) of “Chip Fabrication” shows the placement of posts in order to mold access ports to the microchannel. Another method is punching holes in the cured PDMS once separated from the mold, but great care must be taken to remove any debris from the molded features before bonding the device to a blank substrate, or clogging can occur. The method chosen should reflect the precision desired and application of the microfluidic device, as well as the facilities/equipment available for processing. Moving to (C), liquid polymer is mixed at a 10:1 ratio and poured on the mold and allowed to cure. Once cured, the microchannel slab of PDMS is carefully peeled from the mold (D) and bonded to a substrate (glass microscope slide, or another blank slab of PDMS) using an oxygen plasma treatment [for example, as shown in (E)]. The term “chip” refers to one of these cured/bonded slabs of PDMS that contains molded microchannels. Since the plasma treatment causes the microchannel surfaces to become hydrophilic to aqueous liquids, the chips are heat treated to make them hydrophobic. Typical heat treatment includes a 2 – 4 hour soak at 180°C [54]. Additional information can be found in the review of McDonald et al [6], and Duffy et al [5].

Given that experiments will require electrification of microscale liquid droplet emulsions, precise placement of the device electrodes will give the most control over the applied electric fields, and offer the greatest flexibility when designing a device. A low cost option for obtaining such precision electrodes was developed by Siegel et al [7]. The process is called “microsolidics,” and allows for electrodes to be placed relative to the flow microchannels with the same precision offered by

Microsolidic Procedure



Healing Procedure

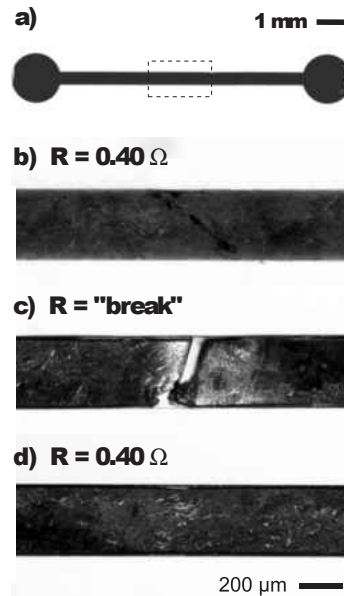


Figure 7: Microsolidics fabrication steps (left column) and electrode healing procedure (right column) - adapted from [7].

the fabrication process of the microfluidic device itself. This is because additional microchannels are designed and fabricated into the microfluidic device, and, after fabrication according to figure 6, are then filled with an electrically conducting yet low melting point metallic material. The low melting point is required because, after first treating the channels to allow for proper wetting of the metallic material, the entire device is then heated to allow the metal to liquefy. Once melted, the liquefied metal “solder” is then drawn through the empty electrode channels using a vacuum.

If the melting temperature is too high, the molded PDMS device could be damaged during heating. Once the device is cooled, the solder solidifies and becomes a molded electrode that takes the shape of the molded microchannel. This process is outlined in the left column of figure 7, and can be used to make very intricate and complex arrays of electrodes that are designed/molded right into the microfluidic device itself. The electrodes can also be used as resistance heaters to provide yet another external field to manipulate droplets. One beneficial feature of microsolidic electrodes, as demonstrated in [7], is the ability to “heal” electrodes that are damaged by applying additional heat (and solder, if necessary) to the device. This is shown in the right column of figure 7, under the heading “Healing Procedure.”

Microchannel Design

This section will contain the details of the specific microchannel geometry molded into the microfluidic chip. The geometry required for this study was that of a T-junction, as shown in figure 1c, which can be categorized as a type of cross-flowing geometry. Specific dimensions were chosen to keep the flow laminar, to achieve fully developed flow by allowing enough channel length after the fluid inlet ports, and to remain within the limits of the soft lithographic manufacturing process. The Reynolds number range based on the channel dimensions, fluids properties, and flow rates chosen for this study ranged from 0.01 – 23.75, well within the laminar flow regime. The laminar entry length required to achieve fully developed flow for these same parameters was $0.1\mu m - 190\mu m$. The fluids considered for this preliminary analysis were silicone oil (PMX-200, Dow Corning) and deionized water (W2-20, Fischer Scientific). As can be seen from figure 8, the entry length requirement is easily satisfied by allowing $5mm$ of channel length after the inlet ports and before the T-junction. This very high safety margin allows for extremely high flow rates should they be needed, as well as the option of changing to much lower viscosity fluids without

fear of encroaching on the laminar-turbulent transition or developing flow regimes. In addition, providing 10mm of channel length after the T-junction allows for adequate imaging and various electrode placements. Figure 8 depicts the dimensions of an individual microchannel and figure 9 shows the full chip with all five microchannels. Table 2 lists the relevant material properties for the silicone oil and deionized (DI) water two-phase flow system.

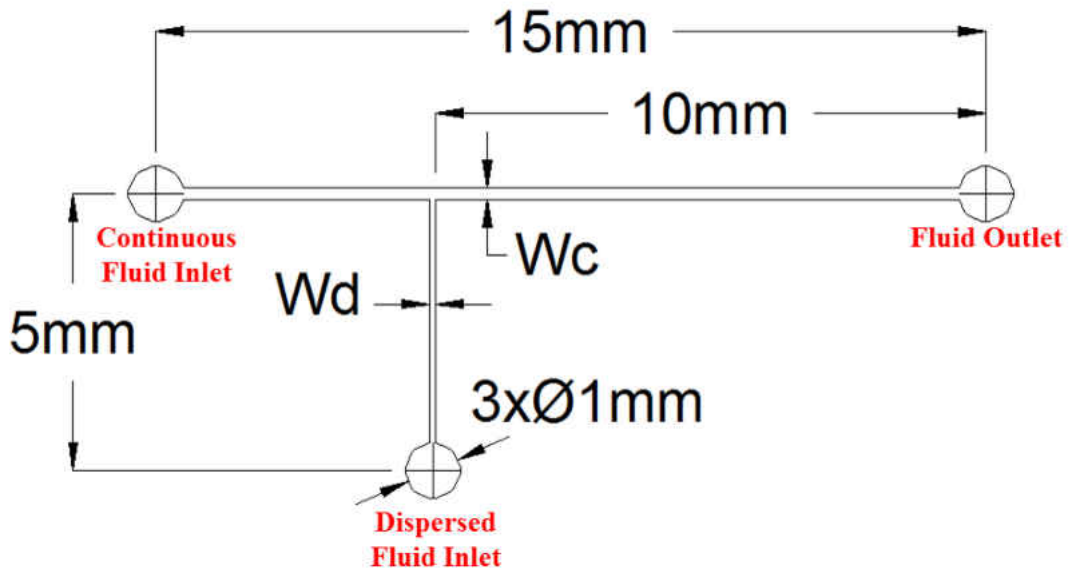


Figure 8: T-junction microchannel geometry.

Table 2: Physical properties of materials tested.

Liquid (-)	Density (kg/m^3)	Dynamic Viscosity ($Pa \cdot s$)	Electrical Conductivity (S/m)	Relative Permittivity (-)
DI Water	1000	1×10^{-3}	8.3×10^{-13}	80
20cSt Oil	950	19×10^{-3}	5.5×10^{-6}	2.2

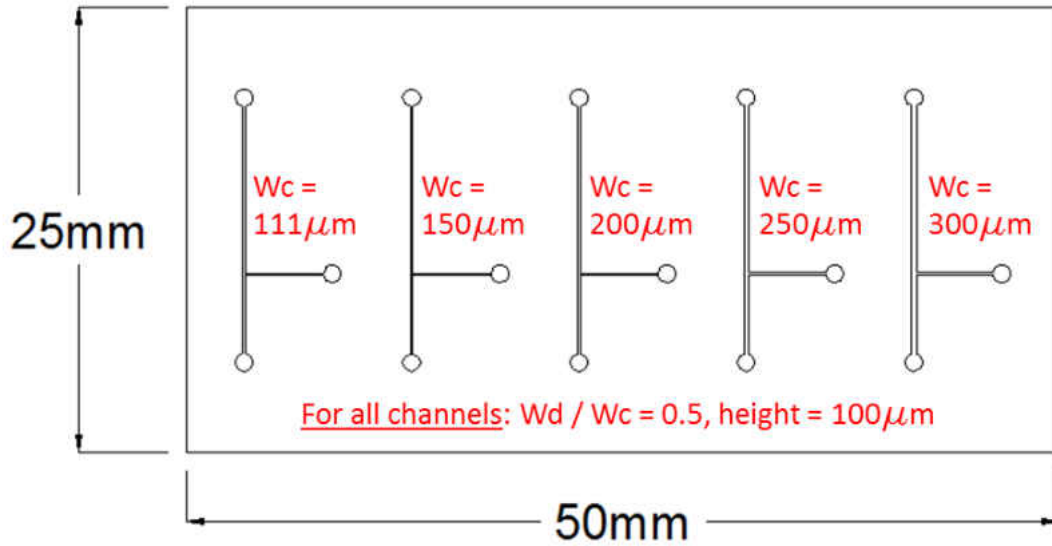


Figure 9: Full chip design with five T-junction microchannels of varying widths.

Electrode Placements

Since the application of an electric field to liquid droplet emulsions created in the T-junction was the primary focus of this study, where and how the electric field was applied was of great importance. Dozens of placement configurations were tested (of the infinite configurations possible), but three were found to have the greatest effect on droplet production and deformation. These three electrode placements can be found in figure 10, and will be denoted as the MKI design. It is important to note that each of the three T-junction microchannels shown represent the same channel, with each configuration denoting different placements of electrodes, and not multiple channels on the chip with the electrode configurations shown. Tests conducted on multiple channels simultaneously within the chip were never conducted to keep the effects of electrification localized. The electrodes used for the MKI design were 0.5mm diameter copper wire, placed approximately 1.5mm away from the microchannel and one another (for configurations 2 and 3). For configura-

tion 1, alligator clips were attached to the dispersed inlet and outlet flow needles.

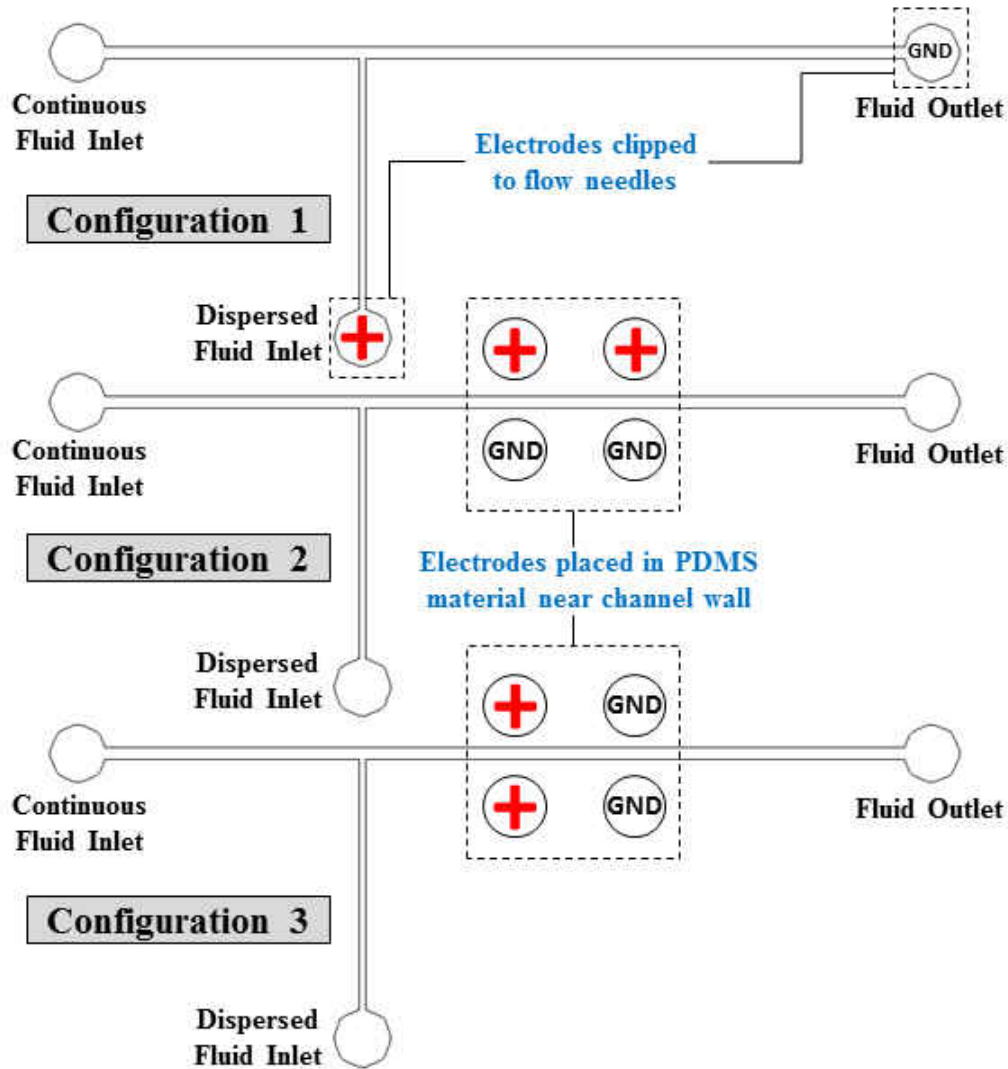


Figure 10: Three electrode placement configurations for MKI channel design.

After several experiments and numerical simulations were conducted with the MKI microfluidic device, a second microfluidic device was designed in order to incorporate the use of microsolidics. Figure 11 shows a schematic of the new device, denoted as the MKII design. The indium electrodes were placed at varying distances from the microchannel, where the $75\mu\text{m}$ spacing is shown in

figure 11.

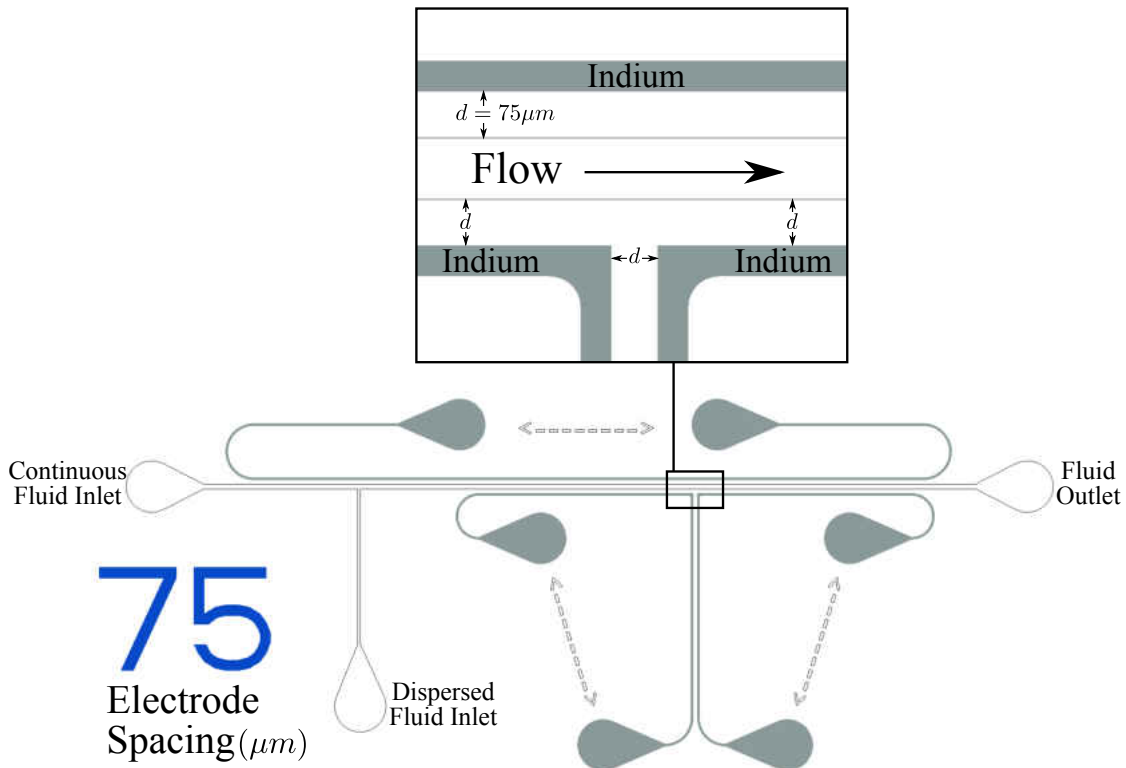


Figure 11: MKII electrode configuration. The continuous and dispersed channel widths, and channel height are $w_c = 100\mu m$, $w_d = 50\mu m$, and $h = 50\mu m$ respectively.

The MKII channel design had some limitations, however. For larger magnitudes of applied DC voltage, the electrodes experienced localized discontinuities due to arcing/shorting as shown in figure 12. The failure mode was not conclusively identified, but local melting and/or delamination of the PDMS material are likely causes. While the MKII design was able to produce some results, a MKIII design is already underway to help alleviate this (and other) problems with the MKII design.

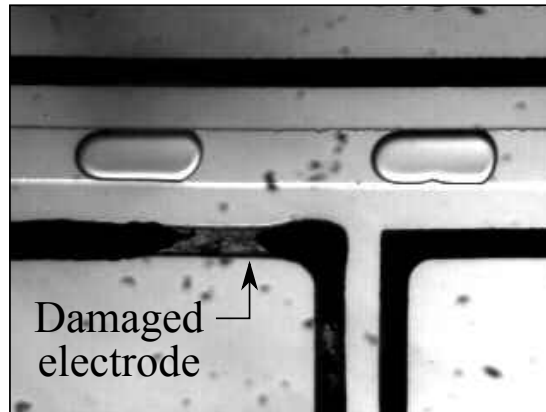


Figure 12: Damaged electrode after applying $V_0 > 3500V$.

Experimental Setup

The experimental setup for testing included five primary components. First were the test section chips discussed earlier, which contained the array of microchannels to be used for testing. Second, separate syringe pumps were used to drive the continuous and dispersed fluids through their respective branches of the T-junction microchannel. Third, the chip was placed under a standard laboratory microscope fitted with 4.0x magnification for visualization purposes. Fourth, one of two high speed cameras were used to capture the images from the microscope. Lastly, a computer equipped with the necessary camera software and drivers allowed direct capture of high speed video. A schematic of the experimental set-up can be found in figure 13, with a listing all equipment used in table 3.

The recorded video was limited to ≤ 200 frames per second (fps) on the Prosilica camera due to the resolution needed (640 x 480 was typically used for this camera). Using a smaller resolution would have allowed for a higher frame rate, and was often used when smaller portions of the microchannel were viewed. However, to obtain a complete view of the droplet formation dynamics at the T-junction, 640 x 480 was an optimal resolution for the Prosilica camera. Prostream, the Prosilica

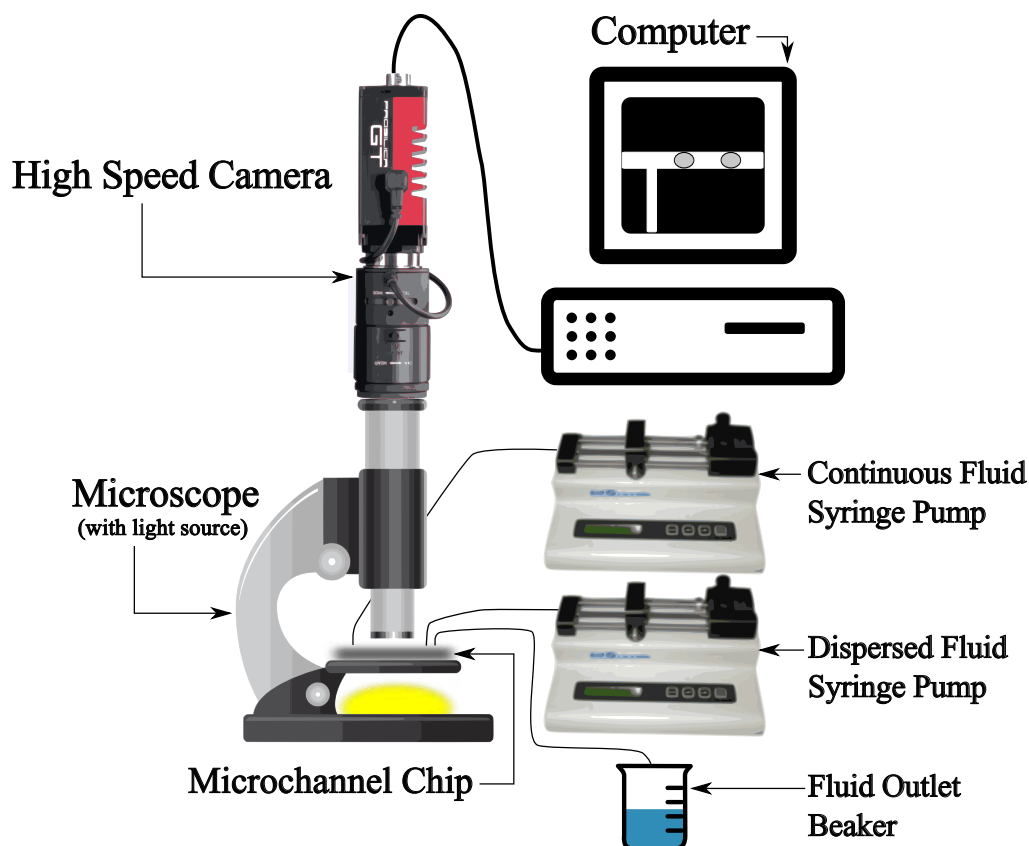


Figure 13: Schematic of experimental setup.

camera software used, allowed direct viewing of the video on the computer screen with virtually no time-lag (i.e. in “real-time”), and also contained a simple video viewing/editing package to aid in manipulating the video once captured (and prior to saving). The FastTech camera offered a far greater recording frame rate at a given resolution ($> 1000\text{fps}$ at 640×480), but was limited by slower file transfer speeds once the video was captured. When using the FastTech camera, the computer was only used as a storage device, as the video files were stored locally on the camera’s memory card until transferred. All basic video editing (like cropping) was performed on the camera itself prior to exporting, which proved to be cumbersome since the camera was mounted on the microscope, and it contained a built-in display of about only four inches in size.

Table 3: Summary of experimental setup components.

Part Name	Manufacturer	Model
Microscope (4.0x)	AmScope	B100B-MS
Camera 1*	Prosilica	GE680C
Camera 2*	FastTech	TSHRMM
Camera Adapter (1.0x)	Diagnostic Instruments	HRD 100-NIK
Fiber Optic Light Source	Techniquip	FOI-150
Syringe Pumps	KD Scientific	780272
Syringes (5cc/mL)	Terumo	SS-05S
Needles (23GA-Straight)	Small Parts	NE-232PL-C
Needles (23GA-90°)	Small Parts	NE-9023-25
Tygon Tubing (0.020" ID)	Saint-Gobain	S-54-HL

*Not used simultaneously.

An alternative would be to export the full video and edit it using external software, or unmount the camera each time video needed to be edited (prior to export), but slower file transfer speeds and time spent mounting/unmounting the camera made these options less efficient. Under standard testing conditions, the Prosilica camera proved to be satisfactory given its limitations.

CHAPTER 5: NUMERICAL MODEL

This section will give an overview of the numerical modeling performed for comparison to the experimental data. The details of the numerical model are listed along with the necessary simplifications to minimize computational overhead while sacrificing minimal accuracy.

Mathematical Formulation

Equations 3 - 8 listed in section (governing equations) and table 4 (boundary conditions) outline the mathematical formulation of the two-phase flow problem for both the fluid mechanics and electric field.

Table 4: Summary of numerical boundary conditions.

Physics	Boundary Condition	Location
Fluid Flow	$L_{ent} \nabla_t \cdot \left[-p_{ent} \mathbf{I} + \mu \left(\nabla_t \mathbf{v} + (\nabla_t \mathbf{v})^T \right) \right] = -p_{ent} \mathbf{n}$	Inlets (Laminar inflow)
	$p = p_0$	Outlet pressure
	$\mu \left(\nabla \mathbf{v} + (\nabla \mathbf{v})^T \right) = 0$	Outlet viscous stress
	$\mathbf{F}_{fr} = -(\mu/\beta) \mathbf{v}$ $\int_{\partial\Omega} \text{test}(\mathbf{v}) \cdot [\gamma (\mathbf{n}_{wall} - (\mathbf{n} \cos \theta_{wall})) \delta] dS$	Wall friction Wall contact angle (Weak formulation)
Electric Field	$\psi = \psi(\mathbf{r}_S)$	Wall potential
	$-\mathbf{n} \cdot (\epsilon_0 \epsilon \mathbf{E}) = 0$	Inlet/Outlet - PD (Zero charge)
	$-\mathbf{n} \cdot (\sigma \mathbf{E}) = 0$	Inlet/Outlet - LD (Electric insulation)

L_{ent}	Entrance length	p_{ent}	Entrance pressure
p_0	Outlet pressure	β	Slip length
Ω	Volume domain	S	Surface domain
$\text{test}(\mathbf{v})$	Velocity test function	\mathbf{n}_{wall}	Wall normal vector
θ_{wall}	Wall contact angle	\mathbf{r}_S	Wall position vector
PD	Perfect Dielectric	LD	Leaky Dielectric
\mathbf{F}_{fr}	Wall friction force		

The wall contact angle was chosen to be hydrophobic to water ($\theta_{wall} > 90^\circ$), and the slip length (β) was chosen to be equal to the mesh element size. Finally, the following list of assumptions are used:

Assumptions

1. All fluids are considered incompressible.
2. Gravitational effects are considered minimal, and are therefore neglected (see Froude and Bond number values in table 1).
3. Bounded charge density is not considered because polarization effects are factored in when using the dielectric permittivity (refer to equation 7).
4. The electric field is assumed to be steady (no time dependencies). Experimental measures will be evaluated after the slowest electrical relaxation time has elapsed.
5. Electrowetting at the channel walls will be neglected, opting instead for a fixed hydrophobic contact angle.
6. Some models are considered two-dimensional (Cartesian coordinate system) with the understanding that this may severely impact the accuracy of the results. Primary concerns are

with interfacial forcing terms which are a major contributor to droplet dynamics. While this assumption may offer a way to reduce computational cost, its impact will be compared to results from three-dimensional models.

Discretization/Solver Scheme

The governing equations and boundary conditions for both the fluid flow and electric field were implemented numerically using the commercial software package COMSOL Multiphysics. The two-phase laminar flow level set method was used to capture the moving interface shared between the two fluids, and provides one additional conservation law to the list of governing equations.

$$\frac{\partial \Phi}{\partial t} + \nabla \cdot (\mathbf{v}\Phi) = \lambda \nabla \cdot \left(\eta \nabla \Phi - \Phi(1 - \Phi) \frac{\nabla \Phi}{|\nabla \Phi|} \right) \quad (13)$$

Φ	level set function
λ	Reinitialization parameter
η	Interface thickness parameter

The level set function (Φ) prevents any discontinuities by assigning a dimensionless value between zero and one to each location within the domain at any given time step. This value represents the absolute volume fraction of each of the two phases at that specific grid node. First consider the extreme values of this function: when a location is chosen in the bulk of fluid 1 at a given time, the level set function will be equal to zero. Conversely, when a location is chosen in the bulk of fluid 2 (at the same time), the level set function will be equal to one. At the interface, the the level set function transitions from 0 to 1 in a continuous manner dependent on the interface thickness parameter (η). This parameter is typically set to be half the size of the largest element to prevent

inaccurate representation of the interface. The appearance, when graphed, is typically that of a smoothed step function. The function is also used to maintain continuity among all the physical material properties at the interface, and is implemented by modifying these properties to include the level set function as follows:

$$\begin{aligned}
 \text{Density:} \quad \rho &= \rho_1 + (\rho_2 - \rho_1)\Phi \\
 \text{Viscosity:} \quad \mu &= \mu_1 + (\mu_2 - \mu_1)\Phi \\
 \text{Relative permittivity:} \quad \epsilon &= \epsilon_1 + (\epsilon_2 - \epsilon_1)\Phi \\
 \text{Electrical Conductivity:} \quad \sigma &= \sigma_1 + (\sigma_2 - \sigma_1)\Phi
 \end{aligned}$$

The level set method, when initially adapted to model two-phase fluid flow, did not correctly conserve mass [55]. This made the method somewhat less attractive for modeling two-phase flow unless the error induced by this loss of mass could be tolerated. Upon further development, the method was refined to conserve mass by adding a compressive flux, then adding an “artificial viscosity” interface reinitialization (fictitious time step) to minimize stationary shocks induced by the compressive flux. Both of these additions require additional computational effort, but the conservative level set method is used in this work since mass conservation is critical to numerical droplet simulations. The reinitialization parameter was set to a value suited to the study ($\lambda = 0.05/v_{ref}$), and the interface thickness parameter (η) was set to half the maximum element height. Both streamline and crosswind diffusion were implemented for consistent stabilization purposes on both the momentum (with tuning parameter set at 0.5) and level set equations. Equations were mostly discretized with quadratic (second order) elements for the velocity and electric potential

components, and linear (first order) elements for the pressure components.

First, the phases are initialized to capture and establish the starting interface using a direct PARDISO solver. The solver uses a nested dissection multithreaded reordering algorithm, with row reordering/equilibration, a pivoting perturbation value of 10^{-8} , and a convergence factor of 10^{-3} . Matrix symmetry determination was automated during the solution procedure to either be symmetric or Hermitian, and the null-space function method was also automated to be either orthonormal or sparse for the computation of matrices used for handling the constraints. A damping factor was also used while solving that dynamically updated with each successive iteration. Once solved, these initial phase values are passed to the fully coupled time-dependent portion of the solver. A direct MUMPS solver is used with row reordering, equilibration, and pivoting, with a pivot threshold of 0.1. Similar settings were used for determining matrix symmetry and null-space functions that were used with the phase initializing PARDISO solver. The damping method was kept constant in the transient solver with a damping factor set to 1 and a Jacobian update of once per time step. The time stepping was implemented with a backward differencing function (BDF) confined to an interpolation polynomial of maximum order 2, and minimum order 1. All variables are fully coupled and are thus solved simultaneously. When solved, equation 13 includes an intermediate (and fictitious) time step to advect the interface without inducing any artificial viscosities while conserving mass. Each time step was determined automatically by the solver to ensure stability, but the initial time step had to be adjusted in some cases to extremely small values ($< 10^{-10}$ s) in order to prevent immediate divergence. This was because for finer mesh distributions, the numerical stability criteria would not be satisfied, as shown by a general stability relation in equation 14.

$$Stability \sim \sum_i c \frac{\Delta t}{\Delta x_i^n} \leq criteria \quad (14)$$

Where i covers all spatial dimensions within the computational domain and c is a constant specific to the equation being solved. The *criteria* can also vary depending on the numerical scheme being used and the number of dimensions being modeled, but typical values often found in finite differencing schemes range somewhere between $1/2$ and 1 [56]. Each time step converged to $< 10^{-3}$ before proceeding to the next time step. Theoretical derivation and discretization follows that of Olsson et al [57, 58] and Lafaurie et al [59], and these references, along with the user manual for COMSOL Multiphysics, should be consulted for further information.

Possible Simplifications

Two-dimensional models were initially used for computational simplification. The exact T-junction geometry was imported from the CAD model used to fabricate the channels via soft lithography techniques (aforementioned). Given that several channels were fabricated into a single chip the size of a standard microscope slide (as shown in figure 9), the surrounding PDMS material had to be considered in the electrical analysis. Since the minimum channel width ($55.5\mu m$) is 3 orders of magnitude smaller than the minimum chip edge ($25mm$), this presented an element scaling problem (along with unnecessary computational effort) when trying to apply the size range of mesh elements necessary to give accurate flow solutions in the channel. Therefore, a “full chip” model was first created to simulate the distribution of the electric field in the entire PDMS chip without any fluid flow. The steady electrical potential distribution along the boundary of the channel under test was then extracted from the “full chip” model (by curve fitting the data), and applied to a simplified “flow” model that included the channel geometry only. This ensured accurate representation of the electric field as it interacted with both the flowing fluid in an individual channel and the surrounding PDMS material. A sample analysis of curve fitting is shown in figure 14. This electrical potential distribution represents a single electrode placement configuration where

the positive electrode was attached to the dispersed inlet flow needle, and the grounded electrode was attached to the outlet flow needle (MKI - configuration 1 in figure 10). Given the relative ease of placing electrodes in PDMS, an infinite number of electrode placement configurations could be administered by simply adding alignment marks where necessary on the master molds. For MKI experiments in this study, however, the focus was placed only on the three configurations of electrode placements shown in figure 10.

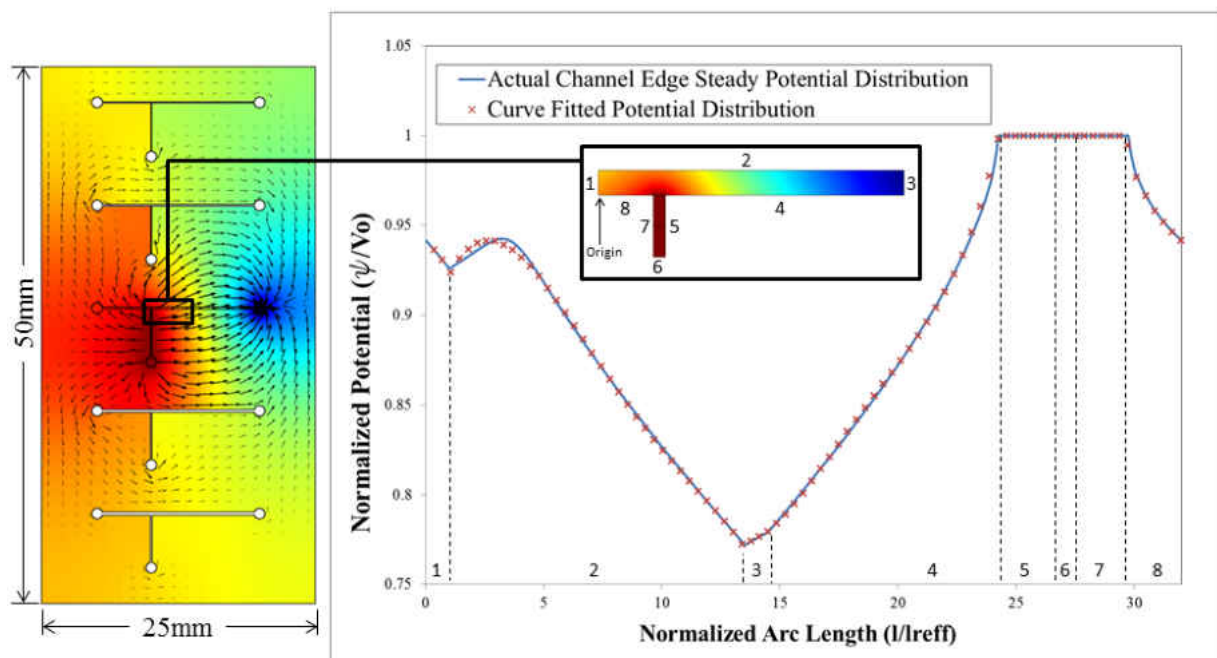


Figure 14: Steady electrical potential distribution of entire chip, and resulting channel boundary electrical potential distribution for MKI - configuration 1. Color scale represents electrical potential, and arrow vectors represent the electric field distribution (left). Numbers along bottom of plot indicate position along channel boundary (see inset).

Additionally, the electrical potential distribution can also be found for MKI - configurations 2 and 3 (as depicted in figure 10). These distributions are shown in figures 15 and 16.

While the profiles listed in figures figs. 14 to 16 were all tested experimentally and numerically, it

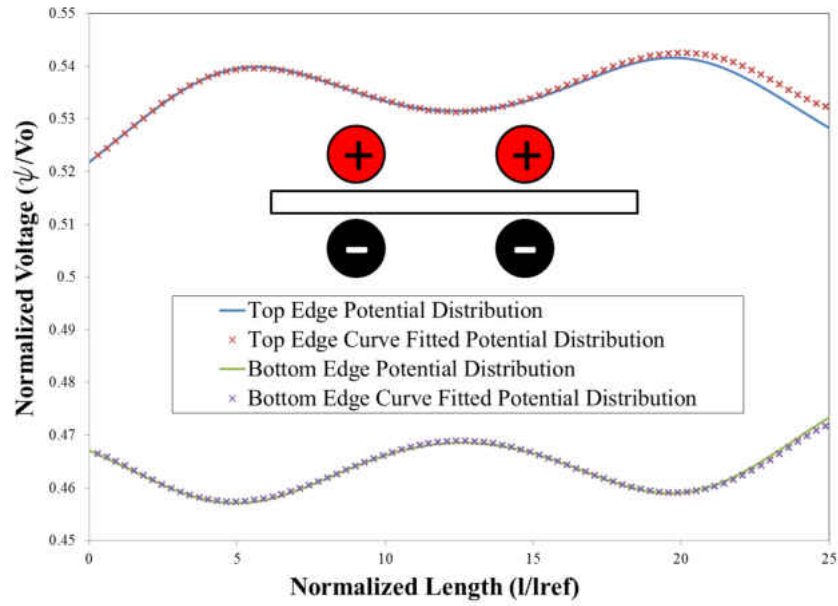


Figure 15: Channel boundary electrical potential distribution for MKI - configuration 2.

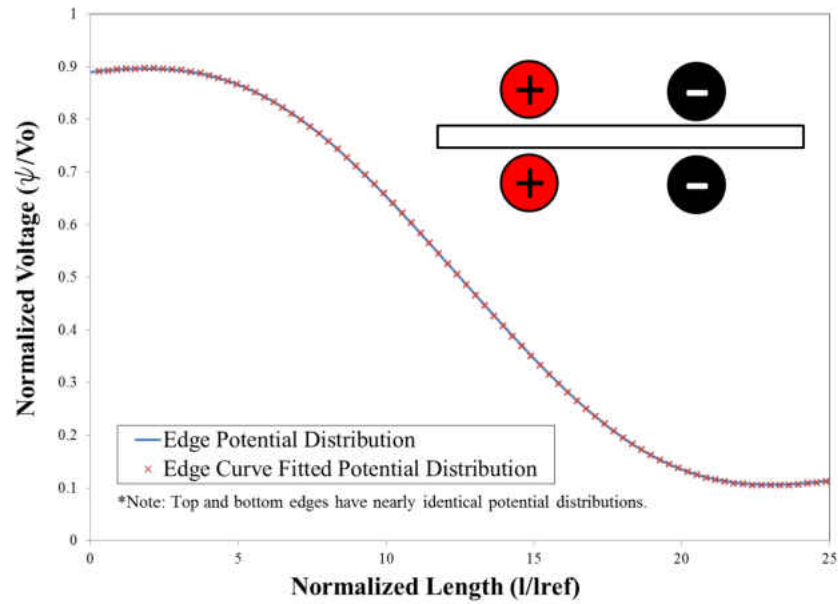


Figure 16: Channel boundary electrical potential distribution for MKI - configuration 3.

was the smoothed step profile shown in figure 16 that became the primary focus for this work. This step represents a smooth transition between two values of electrical potential in a localized area of the microchannel. The physics and associated applications of the step will be discussed later, but the numerical modeling and controlling parameters of the step will be discussed at this time. Step functions traditionally have been used to represent discontinuities, such as how Φ is used to provide a smooth transition between material properties in the level set method. A similar application is required here, but the transition between electrical potential values is not discontinuous in reality like each of the material properties in a two-phase flow system. The slope and severity need to be controllable parameters to keep the flexibility required in order to model the actual system, which can deviate from the “ideal” numerical values. While COMSOL Multiphysics contains several built-in smoothed step functions to accommodate this need (such as Heaviside), a logistic function model was used instead in order to maintain complete control over all shaping parameters. The logistic function is an analytical expression with continuous first and second derivatives that approximates a step function. The generalized spatially dependent logistic function used for this work is listed in equation 15.

$$V(x) = V_0 + \frac{\Delta V}{1 + \exp [c(x - x_0)]} \quad (15)$$

Referring to equation 15, V_0 (units V) is the “offset” with respect to the lower electrical potential (voltage), ΔV (units V) is the scaling parameter that determines the electrical potential range, c (units $1/m$) is the parameter controlling the severity of the slope, and x_0 (units m) is the spatial midpoint of the step. For all of the simulation in this work, $V_0 = 0V$ (grounded) and ΔV becomes the applied DC voltage. The parameters c and x_0 are tuned to fit the localized electrical potential distribution measured from the “full chip” numerical model.

A limitation is revealed when applying the level set method to fluids with large differences in mate-

rial properties. “Large differences” constitute differences of at least 5 orders of magnitude or more, which is easily demonstrated by considering the electrical conductivities of the fluids listed in table 2. When the level set function smears the fluid interface between these two electrical conductivity values, a heavy bias will develop unless the boundary is incredibly thin. This would require that the interface thickness parameter (η) be extremely small, and thus the elements approximating the boundary be very small since η is set to be half the largest element size encountered by the moving boundary. Given that the level set method is a front capturing routine, the elements within the domain do not change position as the boundary moves, but rather report that the boundary is present as it passes through a given location. This is different from front tracking routines, where the nodes/elements move with the boundary dynamically updating the mesh as it travels through the domain. Therefore, it is of no benefit to generate a locally finer, non-uniform mesh at the fluid-fluid interface to obtain greater accuracy if the interface is to move away from its initial location. As soon as the interface passes through a larger element, the η (interface thickness) value has already changed to reflect the larger element size, and any attempts to keep η small have failed. To maintain a thin boundary with a front capturing method such as level set, it is necessary to keep the elements small in every possible location the interface may travel throughout the domain, which may actually be the entire domain if a flowing confined droplet emulsion is the object of study. Figure 17 is a volume fraction plot, depicting how severely the interface shared between the two fluids can be impacted if the element density is too coarse. The color blue represents the dispersed (drop) fluid, and red the continuous (suspending) medium. Another simplification highlighted in this figure is the use of quarter symmetry (only first quadrant shown) to reduce the computational domain.

The only material property that provides difficulty in this study is the electrical conductivity. When considering the fluids mentioned in table 2, the silicone oil behaves as more of a dielectric (non-conductive insulator) and the deionized water behaves more as a conductor. Since the electrical

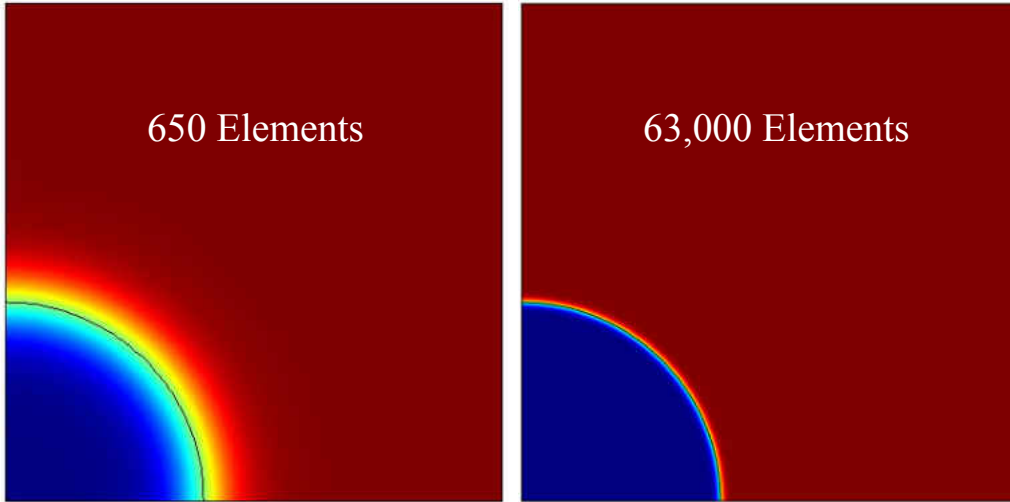


Figure 17: Interface thickness change for two different mesh densities (quarter symmetry model).

conductivity is only used when solving for the electrical potential distribution (and electric field) under the leaky dielectric model, approximations can be made depending on the severity of the difference between the conductivities. One observation reported by Feng and Scott [42] indicates that electrohydrodynamic behavior becomes insensitive to the true value of the fluid conductivities when the conductivity ratio value is 100 or more. For the deionized water ($\sigma_d = 5.5 \times 10^{-6} S/m$) silicone oil ($\sigma_c = 8.3 \times 10^{-13} S/m$) system, the electrical conductivity ratio is $R = \sigma_d/\sigma_c > 10^8$, which satisfies the assumption proposed by Feng and Scott. Other studies have shown that if a perfect conductor and a perfect dielectric make up the two-fluid system under investigation, the electric field can be solved by considering both fluids as perfect dielectrics and setting the permittivity difference between the two fluids to be high [37, 60, 61]. If using this approximation, the permittivities should be chosen such that the (actual) dielectric fluid contain a lower permittivity than the perfect conducting fluid. For the deionized water ($\epsilon_d = 80$) silicone oil ($\epsilon_c = 2.2$) system, this is satisfied because the permittivity ratio is $q = \epsilon_d/\epsilon_c = 36.4$. A comparison using these two fluids, with silicone oil as the continuous (suspending) medium and deionized water as the dispersed (droplet) fluid can be found in figure 18.

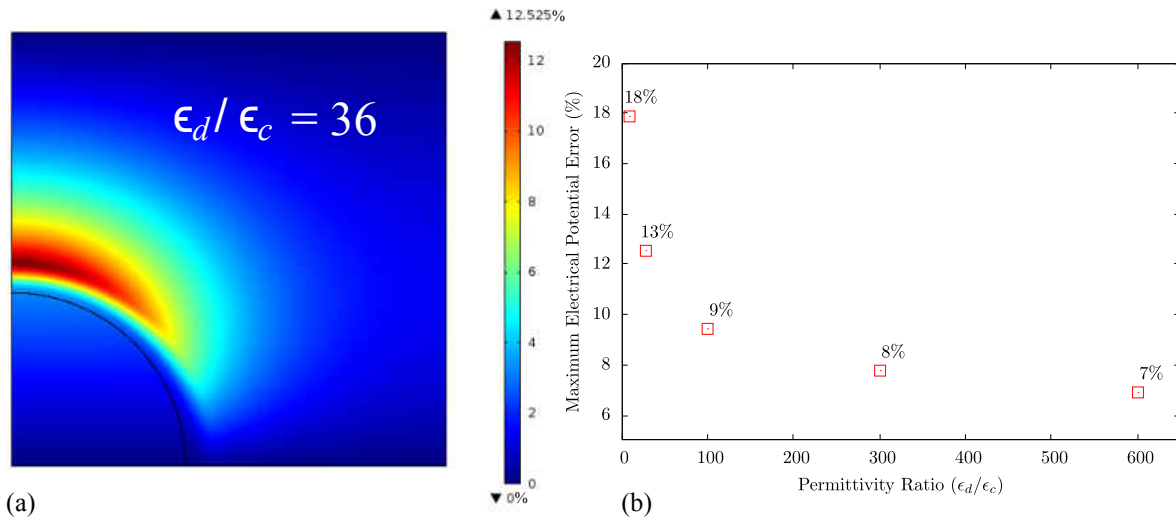


Figure 18: (a) - Percent error distribution in electrical potential between perfect and leaky dielectric assumptions. (b) - Maximum error for various permittivity ratios.

Part (a) of the figure is a two-dimensional error plot, highlighting the percent difference between the leaky dielectric electrical potential distribution (solved using equation 12a) and the perfect dielectric electrical potential distribution (solved using equation 12b). The error is located outside the droplet, and is shown to contain a maximum of around 12.5%. This error is due to the large electrical conductivity gradient that is smeared between the two fluids using the level set function (Φ). A series of permittivity ratios are plotted in part (b) of figure 18 to highlight that as the permittivity gradient gets large it begins to reflect that of the conductivity gradient, and the error between the two solutions is reduced. While both approximations are viable, setting the conductivity ratio to a maximum of $R = 1000$ will be used (because of its minimal error) whenever the leaky dielectric model is required.

CHAPTER 6: RESULTS

The results are divided into five main sections. The first section will provide a series of validations and numerical interrogations to ensure the validity of the mathematical and numerical models. The second section will investigate the computational sensitivity of the numerical models. The third section will show how pinning of a flowing droplet can be accomplished by utilizing a step function boundary condition for the electric potential on one of the microchannel walls. A parametric study is provided that compares the balance of forces required for droplet pinning for a series of drop sizes. The fourth section will illustrate how the physics that contribute to droplet pinning can be leveraged to route droplets of two different sizes. Finally, the fifth section will show how these same physics can bin droplets by size. All five sections, and their subsequent studies, will be performed both in two-dimensional (2D) and three-dimensional (3D) Cartesian computational domains.

Validation of the Numerical Models

The results begin with two validations that represent the two primary physical phenomena occurring when a droplet producing T-junction is electrified. The first validation is designed to test droplet production alone, and compares results produced by the T-junction droplet numerical model with known experimental measures. This will help to provide assurance that the two-phase level set numerical method models droplet production in a T-junction with an acceptable level of accuracy before any electrical effects are introduced. The second validation is designed to test known types of deformation experienced by a stationary liquid droplet immersed in a medium under the influence of an electric field. The numerical results in this case will be compared to well documented theoretical results from the literature, and will help determine if the numerical model

is representing the effects of the electric field accurately.

Validation 1: T-Junction with No Electric Field

Results showing good agreement between models utilizing the two-phase level set method and experiments have been reported for a wide range of interface contact angles, viscosity ratios, flow rates, and channel geometries [62]. After the T-junction was modeled numerically in this study, it was compared to experimental droplet video/images under identical flow conditions to validate its accuracy. In figure 19 and table 5, representative cases of both experimental and numerical droplets are shown to validate the qualitative (appearance) and quantitative (measured) properties.

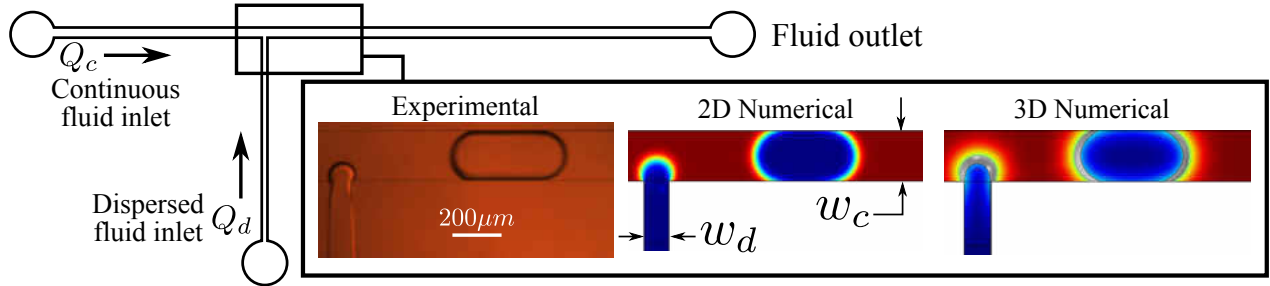


Figure 19: Qualitative comparison between experimental and numerical droplets. The continuous fluid is silicone oil and the dispersed fluid is deionized water (see table 2 for material properties) with $Q_c = 200\mu L/hr$, $Q_d = 100\mu L/hr$, $w_c = 200\mu m$, and $w_d = 100\mu m$. For the experimental and 3D numerical cases, the channel height is $h = 100\mu m$.

Table 5: Quantitative comparison between experimental and numerical droplets.

	Length (μm)	Frequency (drops/sec)
Experimental	480	4.1 drops/sec
2D Numerical (Error)	392 (18%)	4.2 (2.4%)
3D Numerical (Error)	452 (5.9%)	4.0 (2.4%)

Droplet length was chosen instead of droplet volume to permit comparison with numerical droplets produced two-dimensionally. Even with this approximation, there is still good agreement between the experimental and 2D numerical droplet frequencies (2.4% error), which refers to the rate of droplet production at the T-junction. The 2D numerical droplet length, however, shows a larger error (18%) when compared to experiments. Even though the magnitude of the errors are different, the cause is hypothesized to be the two-dimensional domain simplification, and its impact on the droplet surface tension forces. Droplet length and frequency are interrelated by the requirement to maintain flow continuity, so if the droplet frequency predicted numerically were to increase, the droplet length would need to decrease proportionally. Experimental comparison with droplet length and frequency produced using 3D numerical models agree rather well, highlighting that replicating the flow geometry as accurately as possible produces the most accurate droplet formation results. Considering the infinite approximation induced in a spatial dimension by assuming a two-dimensional Cartesian flow domain, the numerical and experimental results agree rather well, but still indicate that this third spatial dimension omitted numerically plays a critical role in droplet formation.

Validation 2: Stationary Droplet Under Electric Field

A second validation was carried out to ensure the initial application and coupling of the electric field with the fluid flow was performed correctly. Several theoretical, experimental, and (recently) numerical studies have been performed on the deformation (and flow) induced by an electric field on a stationary liquid droplet suspended in another liquid. Given the plethora of published data available from these studies, which span over 60 years at the time of this writing, this same configuration was solved using the two-phase level set numerical technique outlined above. The stationary droplet case was chosen to isolate and highlight any physical deformations caused by electrical effects independent of any bulk channel flow, as the dynamics of droplet production in a microflu-

idic T-junction contain plenty of deformations even before electrical effects are considered. The validation is performed with both two- and three-dimensional numerical simulations.

The governing equations used to model the fluid flow are the continuity and momentum equations (equations 3 and 4, respectively). The electric field is modeled using the conservation of charge (equation 6), neglecting any bulk free charge. Normalization of the continuity and conservation of charge equations leads to equations 10 and 12a, respectively. Normalization of the fluid momentum equation initially takes the form of equation 11, but is slightly modified to enable a thorough parametric study of the electric capillary number. The modified form of equation 11 is listed below in equation 16.

$$\begin{aligned} \rho^* \frac{\partial \mathbf{v}^*}{\partial t^*} + \rho^* (\mathbf{v}^* \cdot \nabla) \mathbf{v}^* = & -\nabla p^* + \frac{1}{Re} \nabla \cdot \mu^* (\nabla \mathbf{v}^* + (\nabla \mathbf{v}^*)^T) \\ & + \frac{Ca_e}{ReCa} \frac{L}{r} \nabla \cdot \epsilon^* [\mathbf{E}^* \mathbf{E}^* - \frac{1}{2} (\mathbf{E}^* \cdot \mathbf{E}^*) \mathbf{I}] \\ & + \frac{1}{We} \kappa^* \delta^* \hat{\mathbf{n}} \end{aligned} \quad (16)$$

With dimensionless numbers taking the form:

$$Re = \frac{\rho_c v_{ref} L}{\mu_c} \quad Ca_e = \frac{E_0^2 \epsilon_0 \epsilon_c r}{\gamma} \quad Ca = \frac{\mu_c v_{ref}}{\gamma} \quad We = ReCa$$

All spatial parameters (and gradient operators) are normalized by $l_{ref} = L = 1mm$. Defining the electric capillary number (Ca_e) using the drop radius ($l_{ref} = r$) requires the L/r quantity in the Maxwell stress tensor. The subscript c refers to continuous phase physical properties.

Theoretical studies by Reddy and Esmaeeli [63] were considered to validate numerical simulations of two-dimensional stationary droplet deformation in a suspending medium under an applied elec-

tric field. The droplets were represented in 2D as infinite liquid jets under a transversely applied electric field. The deformed droplet boundaries result from the balancing of normal and tangential boundary forces (between hydrodynamic and electric effects), and cause the droplet to take either a prolate or oblate shape, as shown in figure 20. This diagram is a reproduction of figure 5, but specific to both 2D and 3D droplet configurations.

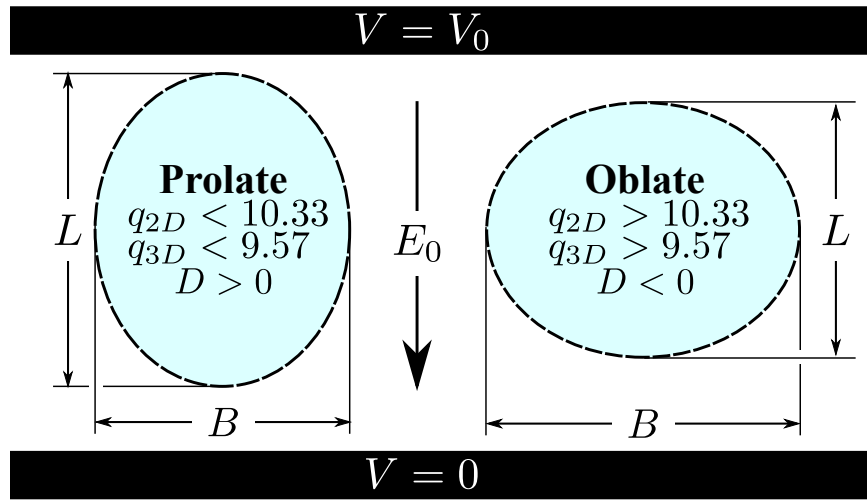


Figure 20: Schematic of two-dimensional stationary droplet deformed shapes. $q = \epsilon_c/\epsilon_d$, and is the ratio of relative permittivities, and D is the droplet deformation defined by equation 17, 18, or 19.

The theoretical deformation for a two-dimensional stationary droplet using the leaky dielectric model is [63]:

$$D = \frac{Ca_e}{3} \left[\frac{R^2 + R + 1 - 3q}{(1 + R)^2} \right] \quad (17)$$

where $R = \sigma_d/\sigma_c$, $q = \epsilon_d/\epsilon_c$ and $Ca_e = E_0^2 \epsilon_c \epsilon_0 r / \gamma$ is the electric capillary number which quantifies the ratio of electric forces to interfacial forces. ϵ_c , E_0 , r , and γ are the permittivity of the

continuous liquid, applied electric field, undeformed droplet radius, and interfacial surface tension, respectively. The vacuum permittivity is given by $\epsilon_0 = 8.854 \times 10^{-12} F/m$. The 2D critical value of the permittivity ratio shown in figure 20 ($q_{2D} = 10.33$) is obtained by setting $D = 0$ and $R = 5$ in equation 17, then solving for q . This represents a critical permittivity ratio below which the deformed droplet will be prolate ($D > 0$), and above which the droplet will be oblate ($D < 0$). For comparison, droplet deformations observed experimentally or numerically (as in this case) can be quantified as:

$$D = \frac{L - B}{L + B} \quad (18)$$

where L and B are the deformed droplet dimensions in Fig.20.

The 2D computational domain was modeled in a dimensionless Cartesian coordinate system using quarter symmetry, with a droplet of dimensionless radius $r^* = r/L = 0.5$, and boundaries at $x^* = y^* = 1.5$. Flow symmetry boundary conditions are imposed on all exterior boundaries, which are mathematically identical to slip boundary conditions. A detailed study is shown later that justifies this boundary condition. Zero pressure is defined at a single boundary point prevent divergence. The electrical potential boundary conditions take a Dirichlet form, and are defined such that the maximum value (V_0) is along the top boundary, and half the maximum ($V_0/2$) value is along the bottom boundary (due to symmetry). The right and left boundaries take a Neumann form, and are set to zero electric flux. The computational domain, along with the boundary conditions (both flow and electrical) is illustrated in figure 21.

Fixed parameter values used for these simulations are the Reynolds number ($Re = 1$), capillary number ($Ca = 1$), density ratio ($\rho_d/\rho_c = 1$), viscosity ratio ($\lambda = \mu_d/\mu_c = 1$), and electric conductivity ratio ($R = 5$). When the permittivity ratio $q < 10.33$, the simulated droplets deform

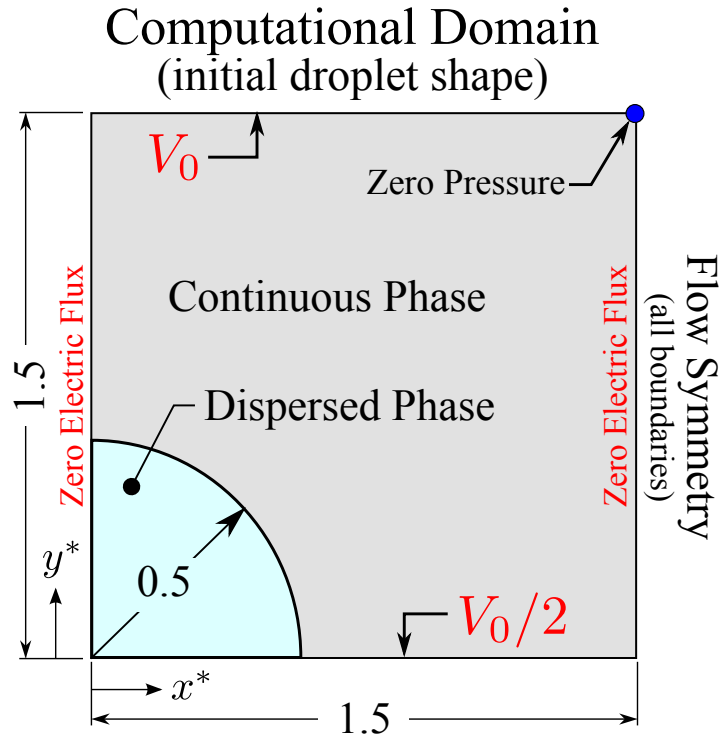


Figure 21: Two-dimensional computational model, highlighting dimensions and boundary conditions.

into prolate spheroids ($D > 0$), and when $q > 10.33$, they deform into oblate spheroids ($D < 0$). The numerical deformations, calculated using equation 18, agree excellently with equation 17, as shown in figure 22 for two electric capillary numbers. Deviations at larger magnitudes of q and D have been reported in other numerical studies [43, 42, 45] and are due to equation 17 being formulated based on Taylor's potential flow assumption (irrotational velocity field and small droplet deformations).

Simulated three-dimensional droplet deformations were also validated against studies conducted by Taylor [36]. The mathematical formulation is identical to the two-dimensional validation outlined above, with the added requirement of the third spatial dimension geometrically. Theoretical deformations in 3D take the form of equation 19 [39], while the numerical deformations still follow

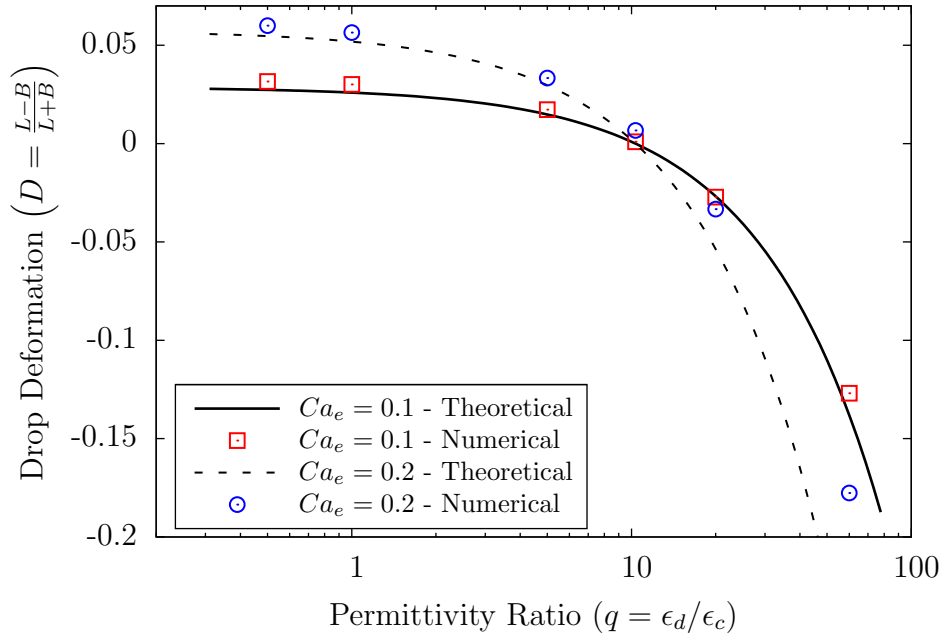


Figure 22: Two-dimensional quantitative comparison of theoretical (equation 17) and numerical (equation 18) droplet deformations.

equation 18.

$$D = \frac{9Ca_e}{16(2+R)^2} \left[R^2 + 1 + -2q + \frac{3}{5}(R-q)\frac{2+3\lambda}{1+\lambda} \right] \quad (19)$$

Referring back to figure 20, the permittivity ratio threshold for 3D is $q_{3D} = 9.57$, with $q < 9.57$ producing prolate droplets ($D > 0$), and $q > 9.57$ producing oblate droplets ($D < 0$). Similar to 2D, this critical permittivity ratio for 3D is found by setting $D = 0$, and $R = 5$ in equation 19 and solving for q .

The computational domain was designed in a three-dimensional Cartesian coordinate system to keep the model physics universally applicable to rectangular flow geometries (used extensively

later). The additional spatial dimension was added by revolving the 2D cross-section in figure 21 by 90° about the y^* axis. This axis in 3D is the z^* axis. The circular outer boundary was necessary to prevent any geometrically induced anomalies due to having a spherical droplet contained within a rectangular medium, resulting in a completely axisymmetric computational domain. The boundary conditions are identical to the 2D boundary conditions, and are illustrated in figure 23.

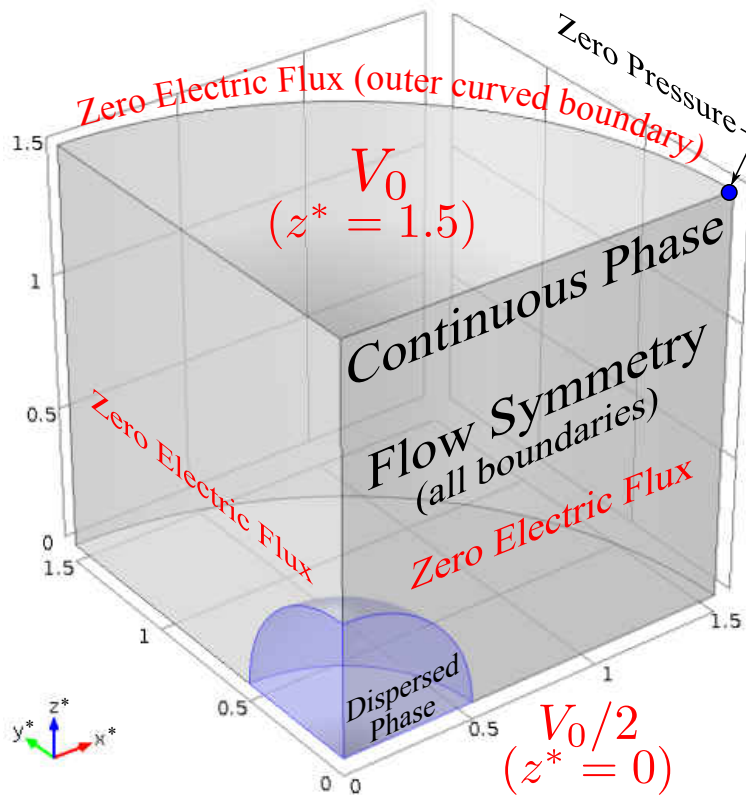


Figure 23: Three-dimensional computational model, highlighting dimensions and boundary conditions.

The three-dimensional droplet deformation results calculated using equation 18 are also in excellent agreement with equation 19, as shown in figure 24. Deviations for larger droplet deformations (and permittivity ratios) are once again due to the irrotational flow assumption (small droplet deformations).

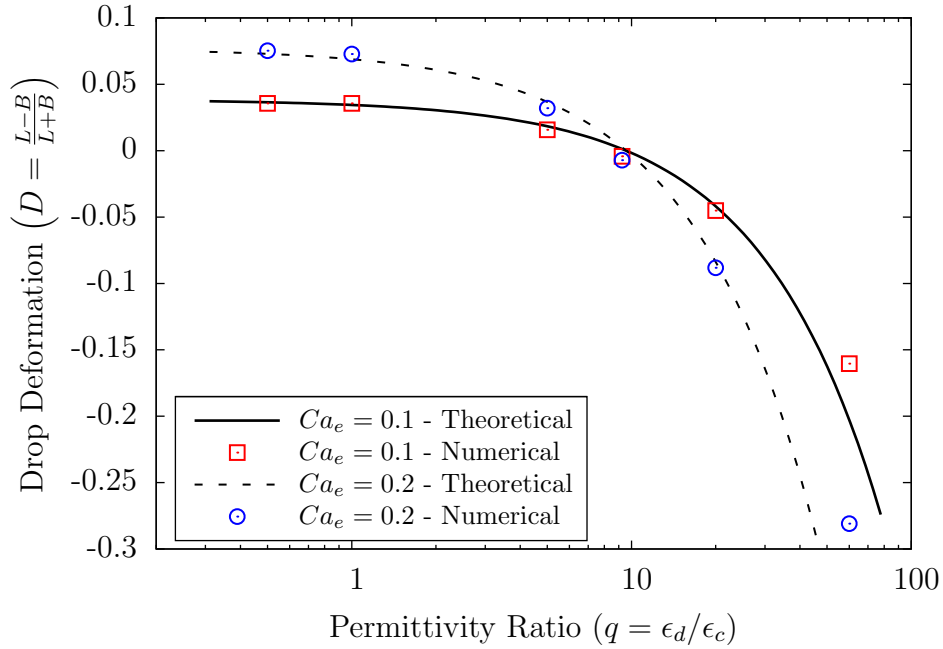


Figure 24: Three-dimensional quantitative comparison of theoretical (equation 19) and numerical (equation 18) droplet deformations.

Computational Sensitivity Studies

Two sensitivity studies were performed on the stationary droplet deformation numerical results. The first was designed to investigate the outer boundary edge effects on the two-dimensional drop deformation, and the second is a traditional mesh sensitivity study where the number of elements is methodically increased in both 2D and 3D numerical models in order to evaluate their accuracy.

Theoretical droplet deformation is based on the solution to the potential flow equation, where semi-infinite boundary conditions are imposed that force the fluid velocity to zero as the distance from the droplet approaches infinity. Since infinite boundaries were not used in the numerical model, unwanted effects from these finite numerical boundaries were investigated by solving the same deforming droplet configuration over for several different edge sizes, while keeping the starting

droplet size constant. This boundary distance parameter is listed as the horizontal and vertical 1.5 dimensions in figure 21. The sweep was performed on the same numerical model used for measuring two-dimensional droplet deformation with $q = 10.33$, and the horizontal and vertical edge dimensions were shifted by equal amounts (always kept equivalent). Equation 17 predicts that a 2D droplet will remain undeformed ($D = 0$) for $q = 10.33$ and any Ca_e , so this is considered the correct solution for the numerical model. The results are plotted in figure 25.

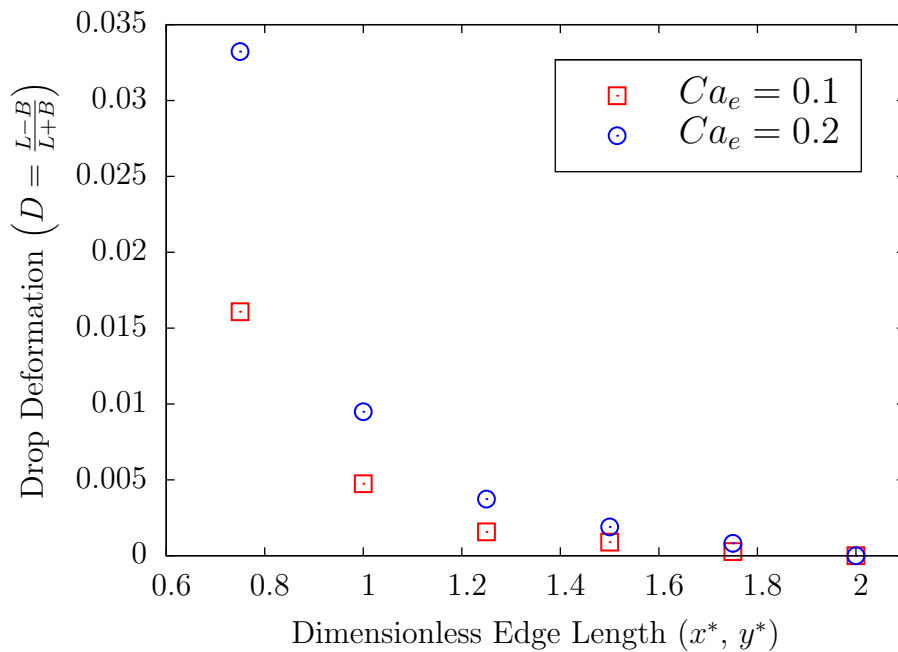


Figure 25: Two-dimensional numerical drop deformation with respect to changes in boundary distance form droplet for $q = 10.33$ ($D = 0$).

As the edge length increases, the 2D numerical drop deformation approaches $D = 0$ for both $Ca_e = 0.1$ and $Ca_e = 0.2$, which is the value also predicted theoretically by equation 17. When the outer computational boundary is closer to the deforming droplet boundary, however, the numerical drop deformation deviates from theoretical values asymptotically. This is due to the presence of the real boundaries in the numerical model causing the continuous fluid flow to circulate back

onto the deforming droplet. Therefore, instead of the velocity at the surface of the droplet being solely due to the physical necessity to balance the tangential electrical stresses, its magnitude gets compounded as time progresses by the recirculating fluid momentum getting redirected around the necessary outer boundaries of the computational domain. This increased fluid momentum causes an increase in the steady drop deformation that is not considered in the theoretical models, the severity of which is tied to the boundary edge length as shown in figure 25. To minimize these boundary effects on droplet deformation, symmetry (or slip) boundary conditions are imposed for the fluids. This allows a full redirection of the fluid momentum rather than decelerating the velocity to zero, as with the no slip boundary condition typically imposed at boundaries that are walls. If the fluid velocity were decelerated to zero at the boundaries (i.e. true no slip walls), the remaining fluid would be required to circulate even faster to maintain flow continuity, thus exacerbating the additional droplet deformation not considered theoretically.

Increasing the edge length also increases the size of the computational domain, which adds computational cost to the model. For this edge sensitivity study, the number of elements was fixed at approximately 62,000, bringing the total degrees of freedom for the 2D model to approximately 540,000. The next study will investigate the mesh sensitivity of both 2D and 3D numerical models for stationary deforming droplets under an electric field, offering further discussion on balance between computational cost versus accuracy.

Typical mesh sensitivity studies are required to ensure that a numerical representation of a mathematical model is of sufficient accuracy. The study can proceed in one of two ways depending on if theoretical solutions are available for validation. If theoretical solutions are available and applicable to the numerical model, then the numerical solution is directly compared to the available theoretical solution to test the model's accuracy. If theoretical solutions are not available, then the mesh density is increased until the numerical solution ceases to change with further refinements. The stationary deforming droplet validation shown earlier provides an excellent mesh sensitiv-

ity study because theoretical solutions are available, and the simulations seek to model the most critical physical laws (electrohydrodynamics) to this study.

Mesh sensitivity studies are performed on both two and three-dimensional drop deformation numerical models. The 2D study is performed for an edge length of 1.5, $Ca_e = 0.2$, and $q = 10.33$. The accepted theoretical deformation is once again $D = 0$ as predicted by equation 17. The results are shown in figure 26, and illustrate how interrelated the edge and mesh sensitivity studies are by how the numerical solution first under predicts the droplet deformation for coarser meshes, then over predicts the droplet deformation as the number of elements is increased. If the edge size were increased to 2.0, the edge effects on the final drop deformation would be minimized, and the deformation would be closer to zero as shown in figure 25. The 1.5 edge size was chosen to highlight this effect. Even though the final solution does not approach the theoretical solution, the numerical error for non-zero values of theoretical drop deformation are on the order of 20%. The numerical solution also begins to change less drastically as the number of elements increases – an indication that the numerical solution is approaching its maximum accuracy for the model.

The three-dimensional mesh sensitivity study was performed on the equivalent scenario of an electrified droplet with zero deformation. For this model, the edge length is set at 1.5, $Ca_e = 0.2$, and $q = 9.57$. The accepted theoretical deformation is $D = 0$ as predicted by equation 19. The results are shown in figure 27. The three dimensional models provided the added challenge of severely increasing the memory requirements while solving, with the largest mesh consisting of over one million degrees of freedom (DOF). This model required nearly 32 GB of available memory for the calculation of each time step on a single shared memory compute node. The 3D results have a similar trend to the 2D results, except that the required mesh density could not be achieved to overshoot the theoretical value for drop deformation in 3D as these higher element meshes became too computationally expensive when the study was performed. Distributed memory high performance computing has been an ongoing item of interest for COMSOL, and while the capability

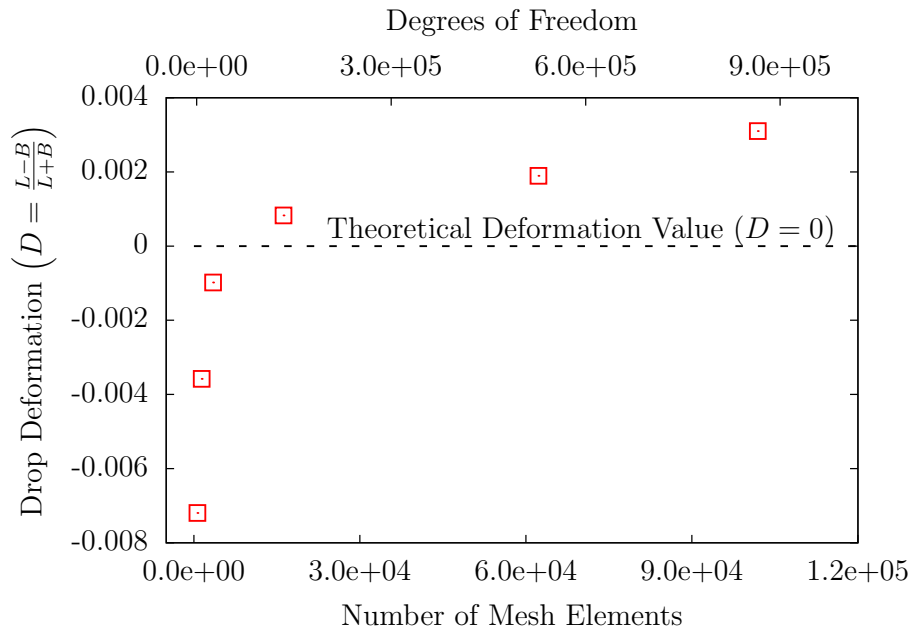


Figure 26: Two-dimensional drop deformation mesh sensitivity study for $q = 10.33$ ($D = 0$).

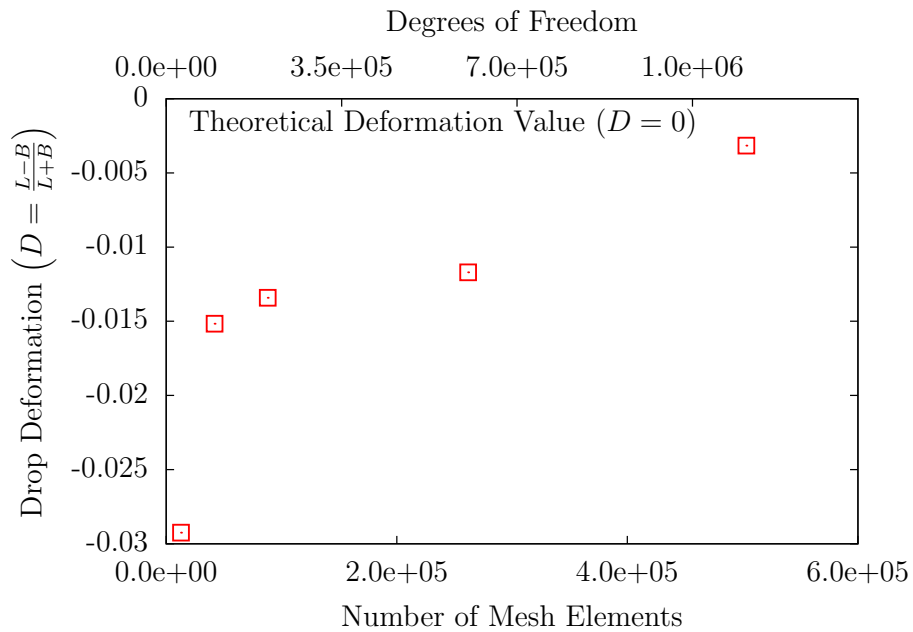


Figure 27: Three-dimensional drop deformation mesh sensitivity study for $q = 9.57$ ($D = 0$).

is currently available (as of v4.3), it is severely limited by the non-parallel portions (i.e. “bottlenecks”) of the MUMPS solver. With these bottlenecks, utilizing more than one compute node simultaneously (i.e. “clustering”) actually more than doubles the computational time, but allows for a much greater memory pool. Future versions of the software should improve this capability, and allow for meshes of much higher density without severely impacting computational cost. Even though the final solution does not demonstrate the same less drastic change as the element number increases, the numerical error for non-zero values of theoretical drop deformation are on the order of $< 7.5\%$, a much better agreement than the two-dimensional numerical models.

These sensitivity studies also provide good examples of the balance required between numerical accuracy and computational cost when evaluating the fidelity of the droplet boundary. The parameter controlling the boundary interface thickness (η) is typically tied to the mesh size in order to maintain an accurate representation of the shared interface, and is therefore affected if the outer boundary edge size increases without also increasing the number of elements. If the edge size is increased, and the number of elements is kept constant, the mesh has become coarser since the same element now represents a larger physical distance. If the mesh density is kept constant as the computational domain size increases, η will also increase in size. However, if the mesh density increases proportionally as computational domain size increases, η will remain constant, but the computational cost of the model has increased. This is where a balance must be reached between accurately representing one of the most critical parts of the computational model at the expense of increased computational cost.

Droplet Deceleration and Pinning

Electrohydrodynamics provides the necessary forces to greatly influence the behavior of flowing liquid droplet emulsions. The studies performed in this section will contain both two- and

three-dimensional numerical simulations, along with observations recorded in both MKI and MKII channel designs to qualitatively validate the numerical behavior.

A smoothed step function of electrical potential (following the form of equation 15) was applied to a channel wall which resulted in droplet deceleration and pinning. It is important to understand the relative magnitudes of the forces that would allow droplet deceleration and pinning within bulk continuous fluid flow. A force diagram depicting flowing droplets of two different diameters, is shown in figure 28.

Both confined and unconfined droplets are shown, along with the flow direction, electric boundary conditions, and contours of electrical potential. As suggested by the contours of electrical potential, the electric force contains non-uniform horizontal and vertical components. The largest component of the electric force, the dielectric force, is acting everywhere normal to the effected droplet surface, and always from the fluid with higher relative permittivity on the fluid with lower relative permittivity. It is strongest at the bottom channel wall, and the magnitude of this forces is estimated by equation 20.

$$F_{Electric} \sim \left(\frac{V_0}{l_e} \right)^2 \epsilon_c \epsilon_0 (hl_e) \sim O(1) \mu N \quad (20)$$

The electric field is estimated by the gradient of the potential step at the lower channel wall, $E_0 = V_0/l_e$, where V_0 is the applied potential, and l_e is the distance over which the potential decays to $V = 0$. ϵ_c and ϵ_0 are the continuous phase relative permittivity and the vacuum permittivity, respectively, and h is the channel height. The product (hl_e) refers to the area over which the electric stress is applied to obtain the effective electric force.

The droplet inertial force depends on the droplet mass and acceleration, and is estimated using

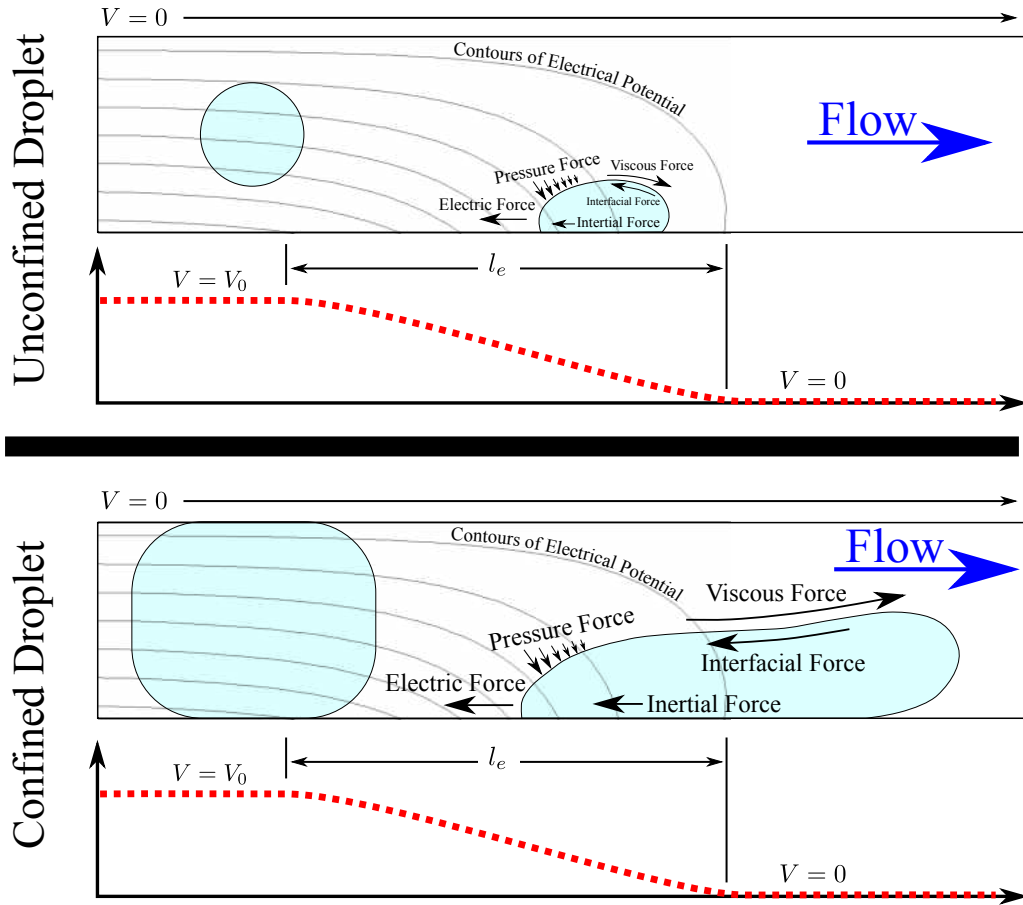


Figure 28: Force diagram on unconfined and confined droplets, with boundary conditions used for electrical potential. A steep potential gradient is used on bottom boundary, and zero potential is used on top boundary.

equation 21.

$$F_{Inertial} \sim \frac{\rho_d u_{ave}^2}{l_e} \left[\frac{4}{3} \pi \left(\frac{d}{2} \right)^3 \right] \sim O(1.19 \times 10^9 d^3) \mu N \quad (21)$$

The mass is obtained by the product of the droplet density (ρ_d) and volume $[4/3\pi(d/2)^3]$, where d is the undeformed droplet diameter. The acceleration scale is estimated by a characteristic velocity

(u_{ref}) over an interval of time ($t \approx l_{ref}/u_{ref}$). The characteristic velocity is chosen to be the average continuous phase velocity of the system $u_{ave} = Q_c/(w_c h)$ and the reference length is distance over which the droplet would be brought to rest ($\approx l_e$) so the acceleration is proportional to u_{ave}^2/l_e . The droplet inertial force is always opposing the direction of the droplet acceleration.

The surface area forces on the droplet are of two types: viscous shear and upstream pressure. The viscous shearing force is the tugging force of the continuous flow past the stationary (or decelerating) droplet, and is estimated using equation 22.

$$F_{Viscous} \sim \frac{\mu_c u_{gap}}{w_{gap}} \frac{1}{2} \left[4\pi \left(\frac{d}{2} \right)^2 \right] \sim O(1.46 \times 10^8 d^2) \mu N \quad (22)$$

The viscous shearing force depends on the continuous phase viscosity (μ_c), the rate of shear strain, and the exposed droplet surface area $[4\pi(d/2)^2/2]$, where d is the undeformed droplet diameter. As the droplet is pinned to the lower channel wall, it acts as an obstruction, causing the continuous fluid flow to pass through the narrow gap created above the droplet. Due to this blockage of the continuous fluid, the surface area effected by viscous shear is not the entire surface area of the droplet, and is instead estimated to be half of the undeformed droplet surface area. The shear rate ($\partial u/\partial y$) is estimated by the quotient of the velocity through the gap and the gap width (u_{gap}/w_{gap}). The gap width (w_{gap}) will also depend on the drop size (and thus, diameter), but the dependency on the diameter is kept to the effective surface area for this analysis. To obtain the order of magnitude result in equation 22, $w_{gap} \approx w_c/4$, and $u_{gap} \approx Q_c/(w_{gap} h)$.

The pressure forces are generated by the pinned droplet blocking the continuous fluid flow. This larger upstream pressure creates a squeezing force over the exposed droplet surface area, and is

estimated using the Hagen-Poiseuille approximation through the gap as shown in equation 23.

$$F_{Pressure} \sim \frac{\mu_c w_c Q_c}{w_{gap}^3 h} \frac{1}{2} \left[4\pi \left(\frac{d}{2} \right)^2 \right] \sim O(5.84 \times 10^8 d^2) \mu N \quad (23)$$

The exposed droplet surface area is the same used for approximating the viscous force $[4\pi(d/2)^2/2]$. The effective gap length is estimated to be w_c , and will also depend on the droplet size, but as with the viscous forces, the dependency on the diameter is kept to the effective surface area for this analysis. To obtain the order of magnitude result in equation 23, $w_{gap} \approx w_c/4$.

The remaining force affecting pinning is the droplet surface tension. The surface tension force acts as a restoring force trying to keep the droplet intact, and acts tangentially to the droplet boundary. This force is estimated using equation 24.

$$F_{Interfacial} \sim \sigma \frac{1}{2} (\pi d) \sim O(7.07 \times 10^4 d) \mu N \quad (24)$$

where σ is the surface tension coefficient for the fluid pair, and d is the undeformed droplet diameter. If the deformed droplet shape were factored into the analysis (not done here), the surface curvature perpendicular to the flow should be used. Like the surface area forces, this force acts over the exposed half of the droplet once it is pinned, but is only effected by the droplet circumference $(\pi d/2)$.

If the magnitudes of all the forces are summed (according to the sign convention in figure 28) at the point where a droplet is about to be pinned, an order of magnitude force balance is achieved. Separating all the electric forces from the hydrodynamic forces, the result is shown in equation 25a. If the electric force is divided through the entire equation, a *dimensionless* force balance is achieved, thus illuminating a critical combination of force ratios necessary for pinning with

dependencies on the drop diameter. This is shown in equation 25b.

$$F_{Electric} \sim -F_{Inertial}(d^3) + F_{Viscous}(d^2) + F_{Pressure}(d^2) - F_{Interfacial}(d) \quad (25a)$$

$$1 \sim -Eu_e(d^3) + Ma(d^2) + Ps(d^2) - Ca_e^{-1}(d) \quad (25b)$$

The parenthesis in equations 25a and 25b denote functional dependencies on d^n and not multiplication by d^n . All dimensionless quantities are defined in table 1 except for Ps , which is not any dimensionless number known at this time, but represents the ratio of pressure to electric forces. This force balance has far reaching implications for optimizing droplet pinning systems, but is offered solely as an order of magnitude study at this time.

The electric force required for pinning a two-dimensional droplet was simulated for droplets of eight different diameters ranging from $62.5\mu m$ to $150\mu m$. The fluid phase properties are for a silicone oil / deionized water system, with properties listed in table 2. The continuous phase flow rate was fixed at $Q_c = 3600\mu L/hr$, and the continuous channel width at $w_c = 100\mu m$, fixing the Reynolds number at $Re = 1$. For the steep gradient in electrical potential at the pinning site, $l_e \approx 390\mu m$ (refer to figure 28). The applied electrical potential (V_0) was then adjusted until pinning occurred for each of the eight different droplet diameters. Each data point required about twenty numerical simulations, and the pinning electrical potential was found within a $5V$ uncertainty. Figure 29 illustrates the results of the pinning force required for each droplet diameter simulated.

The trend of the pinning force per unit length for each of the droplet sizes exhibits features that can be supported through physical explanations. As the droplet size increases, the force necessary for pinning will increase due to the added droplet surface area on which viscous shear

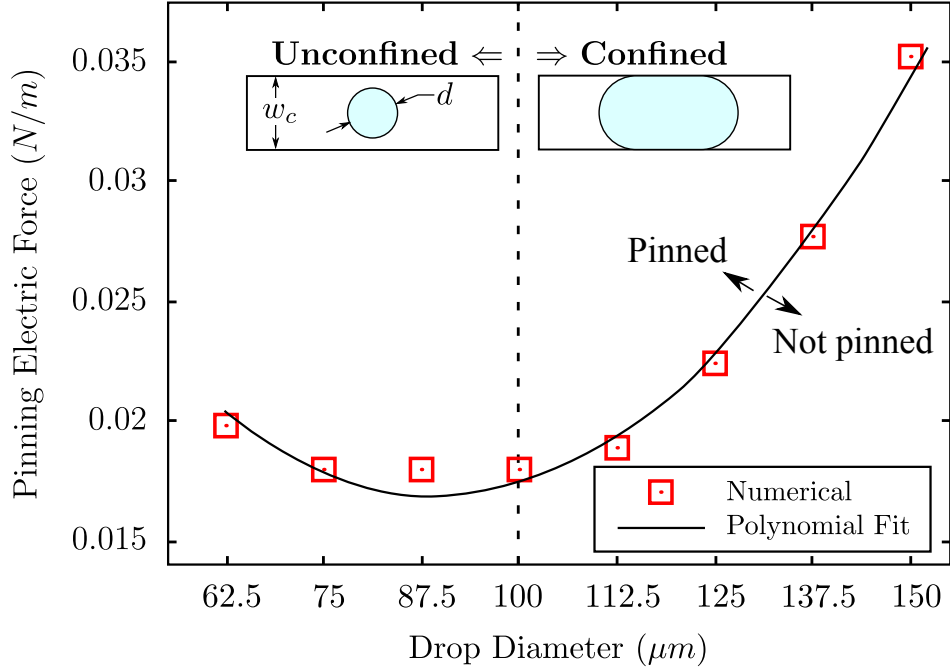


Figure 29: Two-dimensional electric pinning force dependency on drop diameter. Polynomial fit is $F_E = O(N/m) = 4.784 \times 10^6 d^2 - 8.538 \times 10^6 d + 0.055$ with $R^2 = 0.989$. Note that $d = O(m)$ when using the curve fit.

and pressure forces will act. However, there exists a minimum pinning force, located between $75\mu m < d < 100\mu m$. Then, as the drop diameter decreases further, the electric force required for pinning increases once again. When the droplet diameter decreases below $d = 75\mu m$, the droplet boundary is far enough away from the channel walls to start becoming much less effected by the steep gradient in electrical potential at the channel boundary as it passes the pinning site. This is because the electric field strength weakens as it progresses into the continuous channel and polarizes the continuous fluid. Therefore, this smaller droplet receives a fraction of the original strength of the electrical potential step, and thus requires a greater electric force to draw the droplet down to the channel wall in order to be pinned. If the droplet were to enter the pinning site flowing along the channel boundary that contained the steep potential gradient, the electric pinning force would be greatly reduced. This was not factored into the study, however, and all droplets were positioned

at the center of the continuous channel before traveling to the pinning site. The minimum pinning force, located between $75\mu m < d < 100\mu m$, is when the droplet size is large enough to almost start making contact with the channel walls. Having a droplet boundary already flowing near the channel wall containing the steep gradient allowed for pinning to occur without the added effort of first pulling the droplet out of the continuous flow and toward the pinning site. This same droplet is also small enough to keep the surface area forces low (pressure and viscous shear) so that pinning can occur. This droplet diameter range represents an optimized balance of electric and hydrodynamic forces, or “sweet spot,” where a minimum pinning force can be achieved for this 2D flow system.

The data points were fitted with a second order polynomial to match an order of magnitude analysis conducted for the two-dimensional droplets. In the 2D analysis, all forces are calculated per unit depth of the channel, such that the pinning force is in units of N/m rather than μN . The reduction of one spatial dimension was required for each term of the force balance in equation 25a. In the electric force term (equation 20), h was moved to the left hand side. In all of the hydrodynamic forces, the effected droplet geometry was reduced by one spatial order, meaning droplet volume $\sim O(d^3)$ reduced to cross-sectional area $\sim O(d^2)$, droplet surface area $\sim O(d^2)$ reduced to circumference $\sim O(d)$, and droplet curvature perpendicular to the flow $\sim O(d)$ reduced to a constant $\sim O(1)$. All coefficients remained the same, except that the gap width was increased to $w_{gap} = w_c/2$. This is because 2D simulated droplets blocked the channel less than 3D droplets once pinned. The individual magnitudes of each of the polynomial terms are plotted in figure 30.

Volume forces refer to d^2 terms in two-dimensional simulations (such as inertial forces), area forces refer to d terms (such as pressure and viscous shear). and edge forces refer to constants (such as interfacial tension). The force magnitude trends further support the physical explanations for the pinning force trends plotted in figure 29. For smaller droplets, the contribution from volume and area forces are small, and pinning is achieved by the competition between interfacial restoring

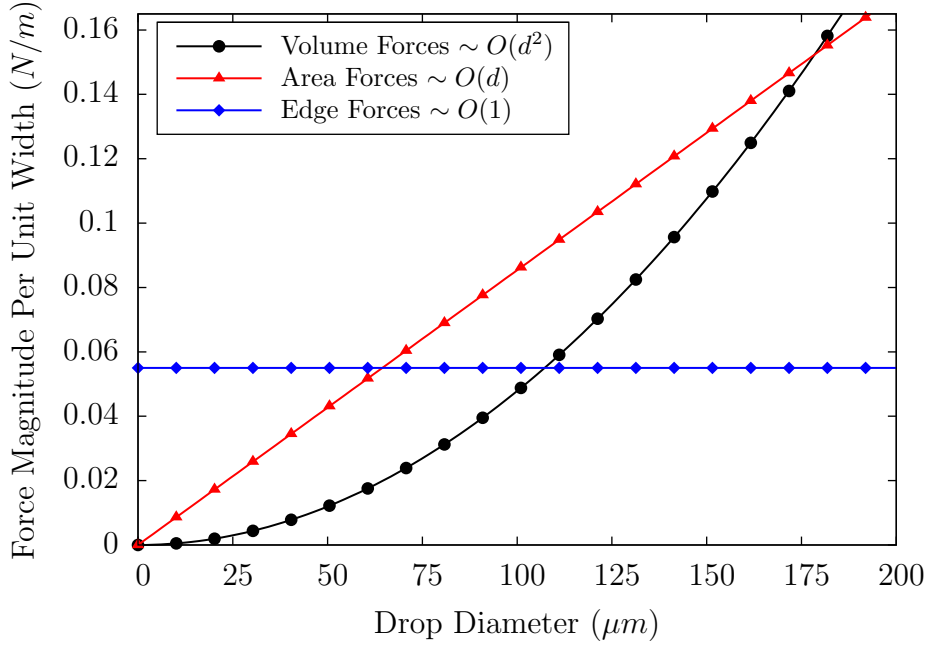


Figure 30: Individual magnitudes of 2D polynomial fit: $F_E = O(N/m) = 4.784 \times 10^6 d^2 - 8.538 \times 10^6 d + 0.055$. Note that $d = O(m)$ when using the curve fit.

forces trying to keep the droplet intact and electrical pinning forces as a droplet boundary passes over a steep potential gradient. Once the droplet size enters the $75\mu m < d < 100\mu m$ range, the surface area force magnitudes become larger, requiring the pinning electric force to increase. As the droplet diameter is increased further, the area and volume forces dominate and the constant interfacial forces are relatively small by comparison. It is also worth noting that the values generated by the order of magnitude analysis for 2D were quite close to some of the coefficients produced by the curve fit, accounting for 82% of the $O(1)$ edge forces ($0.055 N/m \sim \sigma = 0.045 N/m$), and 84% of the $O(d)$ area forces.

The electric force required for pinning a three-dimensional droplet was simulated for droplets of six different diameters ranging from $41.7\mu m$ to $116.7\mu m$. The fluid phase properties are for a silicone oil / deionized water system, with properties listed in table 2. The continuous phase flow rate was

fixed at $Q_c = 550\mu L/hr$, and the continuous channel width and height were $w_c = 100\mu m$ and $h = 50\mu m$, respectively, fixing the Reynolds number at $Re = 0.1$. For the steep gradient in electrical potential at the pinning site, $l_e \approx 390\mu m$ (refer to figure 28). The applied electrical potential (V_0) was then adjusted until pinning occurred for each of the six different droplet diameters. Each data point once again required about twenty numerical simulations, and the pinning electrical potential was found within a $5V$ uncertainty. Figure 31 illustrates the results of the pinning force required for each droplet diameter simulated.

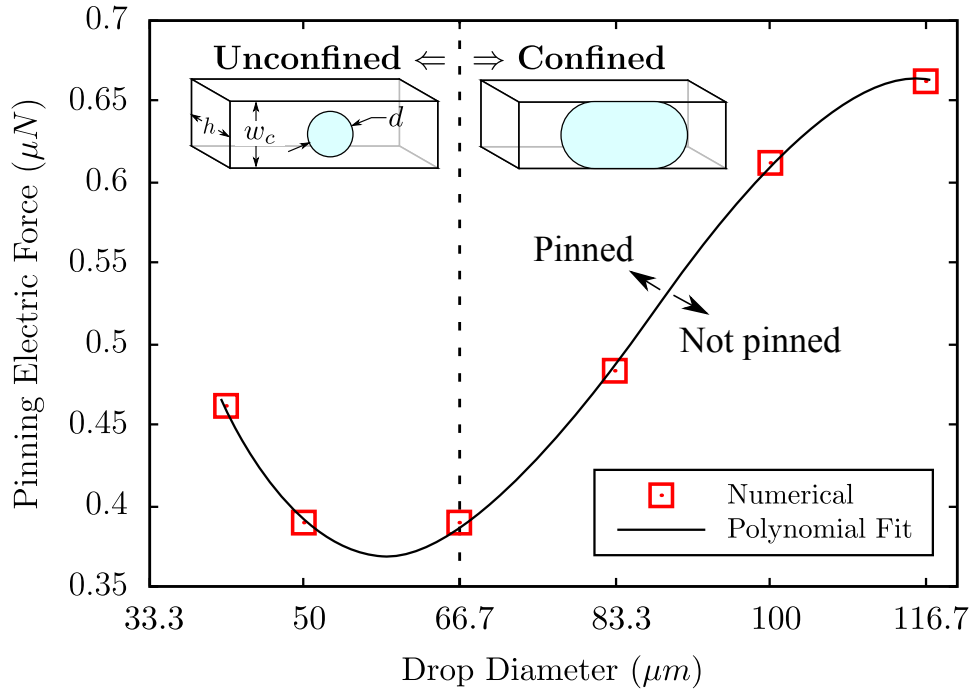


Figure 31: Three-dimensional electric pinning force dependency on dimensionless drop diameter. Polynomial fit is $F_E = O(\mu N) = -3.136 \times 10^{12}d^3 + 8.195 \times 10^8d^2 - 6.369 \times 10^4d + 1.919$. with $R^2 = 0.999$. Note that $d = O(m)$ when using curve the fit.

The trend of the pinning force for each of the droplet sizes exhibits features that can be supported though physical explanations, similar to those discussed for 2D simulations. As the droplet size increases, the force necessary for pinning will increase due to the added droplet surface area on which viscous shear and pressure forces will act. There again exists a minimum pinning force, now

located between $50\mu m < d < 66.7\mu m$. This is the diameter range “sweet spot” where the droplet boundaries are almost making contact with the channel walls while still keeping the tugging surface forces small. As the diameter increases, the increase in viscous and pressure surface forces require additional electric force for pinning. As the diameter decreases, the electric forces must increase in order to first pull the droplet away from the continuous flow and down to the pinning site. The features are much more exaggerated due to the addition of another spatial dimension. In 2D, all force magnitudes increase proportionally per unit length whereas in 3D this is most certainly not the case. For example, in 2D there is a channel wall with a steep gradient of electrical potential that is infinitely deep, whereas in 3D this same channel wall is only $50\mu m$ deep and meets two other channel walls with zero charge. Additionally, in 2D a droplet is actually a cylinder that is infinitely deep, whereas in 3D, the droplets can take a spherical or even ellipsoidal shape. These severe changes cause some of the subtle trends observed in 2D to be magnified in 3D, such as the relative decrease in pinning force for larger droplets ($d = 116.7\mu m$). This is due to a similar effect seen for smaller droplets, where more of the droplet boundary in the continuous channel settles in the electric field once pinned, thus increasing the effective boundary over which the electric pinning force is acting. For electrical potential values below the pinning value for this drop diameter, the droplet would split and a portion would remain pinned while another portion would continue downstream. This is because the restoring surface tension force is not large enough to prevent the viscous shear and upstream pressure forces from deforming and eventually splitting the droplet, highlighting the exact same competition of forces responsible for generating droplets at a T-junction. When the electrical potential is increased, however, the surface tension force is strengthened by the larger electrical forces present at the boundary, keeping the droplet intact and pinned.

The data points were fitted with a third order polynomial to match the order of magnitude analysis conducted for three-dimensional droplets. In the 3D analysis, all forces are calculated in units of

μN . The force balance described by equation 25a is applicable to this system, where the electric force is $\sim O(1)\mu N$. For the hydrodynamic forces, the volume forces (inertial) use the droplet volume $\sim O(d^3)$, the area forces (viscous and pressure) use the droplet surface area $\sim O(d^2)$, the edge forces (interfacial) use the droplet circumference $\sim O(d)$. The individual magnitudes of each of the polynomial terms are plotted in figure 32.

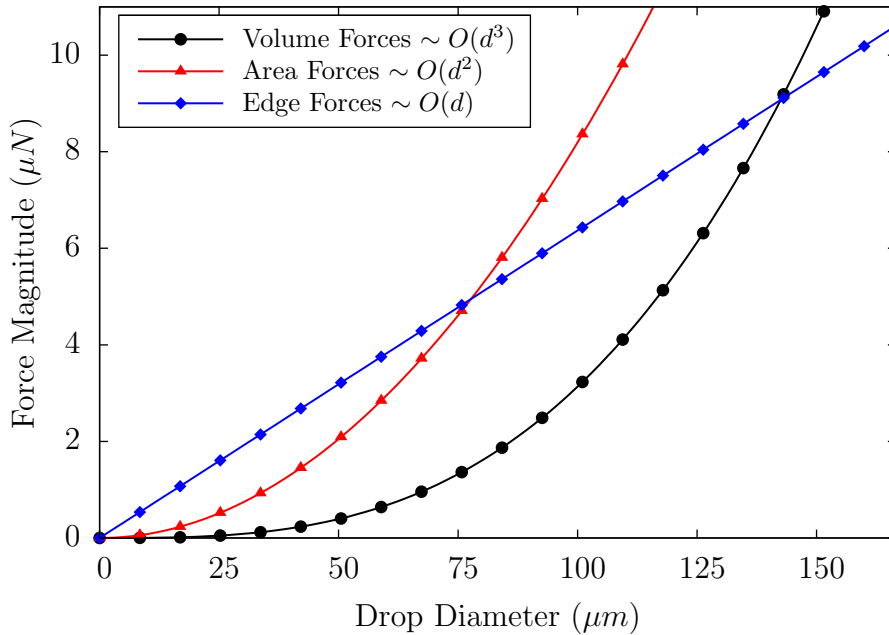


Figure 32: Individual magnitudes of 3D polynomial fit $F_E = O(\mu N) = -3.136 \times 10^{12}d^3 + 8.195 \times 10^8d^2 - 6.369 \times 10^4d + 1.919$. Note that $d = O(m)$ when using the curve fit.

Similar to the 2D plot in figure 30, the force magnitudes further support the physical explanations for the pinning force trends plotted in figure 31. For smaller droplets, the contribution from volume and area forces are small, and pinning is achieved by the competition between interfacial restoring forces trying to keep the droplet intact and electrical pinning forces as a droplet boundary passes over a steep potential gradient. Once the droplet size enters the $50\mu m < d < 66.7\mu m$ range, the surface area force magnitudes become larger, requiring the pinning electric force to increase. As

the droplet diameter is increased further, the area and volume forces dominate and the linear interfacial forces are relatively small by comparison. It is also worth noting that the values generated by the order of magnitude analysis for 3D also close to some of the coefficients produced by the curve fit, arriving within 11% of the $O(d)$ edge forces, and accounting for 89% of the $O(d^2)$ area forces.

Two experiments were designed to investigate droplet pinning in the MKI and MKII channel designs. Of all electrode configurations tested in figure 10, configuration 2 was the only one that demonstrated droplet pinning experimentally for the MKI design. The same microchannel is used as in figure 19, and a channel length of 10mm after the T-junction allowed for adequate imaging and electrode placements. Single strand 24 AWG copper wire ($\approx 0.5\text{mm}$ diameter) acted as the electrodes, and were placed directly in the bulk PDMS material according to the schematic shown in figure 33.

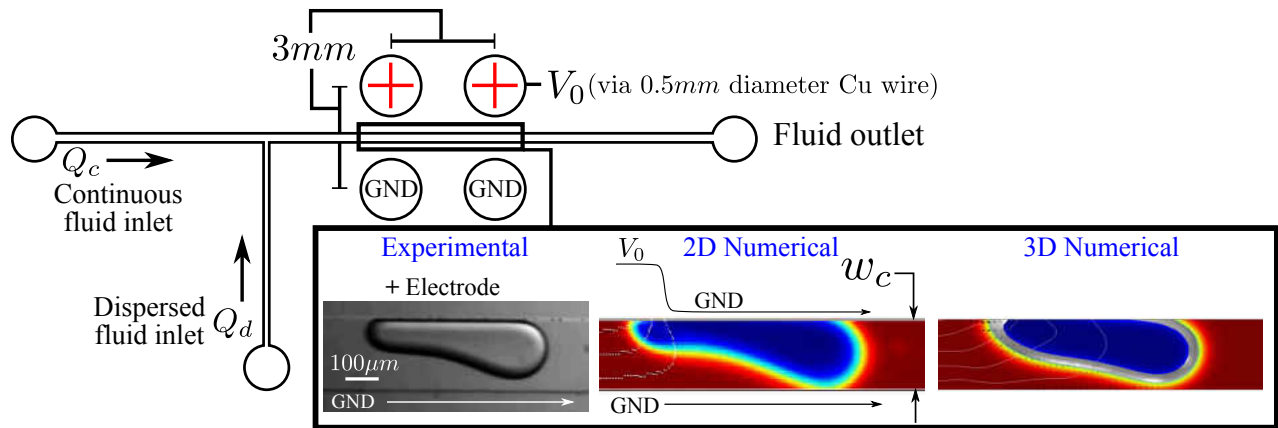


Figure 33: Qualitative comparison between experimental and numerical droplets. The continuous fluid is silicone oil and the dispersed fluid is deionized water (see table 2 for material properties) with $Q_c = 200\mu\text{L}/\text{hr}$, $Q_d = 100\mu\text{L}/\text{hr}$ and $w_c = 200\mu\text{m}$. For the experimental and 3D numerical cases, the channel height is $h = 100\mu\text{m}$.

This placement of electrodes created steep potential gradients along the upper channel wall at locations in the vicinity of the electrodes. The resulting droplet behavior exhibits single-wall de-

celeration and pinning at approximately the same wall location for each passing droplet, similar to the droplet behavior demonstrated in our numerical models. The electrical potential applied to the electrodes was set to $V_0 = 2000V$ (DC), and the pinning locations were located within $1.0mm$ upstream and/or downstream of each electrode pair for a droplet of length $l_d \approx 400\mu m$. The copper wire electrodes were spaced approximately $1.5mm$ from the microchannel, causing the applied voltage to suffer significant attenuation (due to the relatively inert electrical properties of the bulk PDMS material) before reaching the flowing droplets inside the microchannel. Three-dimensional electrostatic models performed in COMSOL Multiphysics (refer to figure 34a) indicate a $\approx 90\%$ reduction in applied voltage under these circumstances, bringing the experimental voltage drop along the microchannel boundaries to $V_0 \approx 200V$. The numerically applied voltage required for similar pinning behavior (under nearly identical conditions) was $V_0 \approx 390V$ for two-dimensional simulations, and $V_0 \approx 350V$ for three-dimensional simulations. The experimental voltage required for droplet pinning is smaller in magnitude than the voltage required numerically, but the agreement is still good considering the numerical approximation and the crude positioning of the copper wire electrodes.

An experiment was also performed using the MKII microchannel design, which suffered similar attenuation as observed on the MKI design. Since the electrodes are generated using microsolidics, they can be placed closer to the flowing droplets. However, the strength of the applied electrical potential is still reduced by 50% (refer to figure 34b) at the channel walls. The reason there is still such a large loss in electrical potential is because the microsolidic electrodes are the same depth as the microchannels themselves ($50\mu m$), since these features were produced from the same constant depth mold. So while the electrode is closer to the microchannel, there is more bulk PDMS material above and below the electrode damping the electric field. However, the MKII design still provided qualitatively good agreement with the droplet deceleration and pinning observed in numerical simulations. While a quantifiable experimental/numerical validation was not performed on

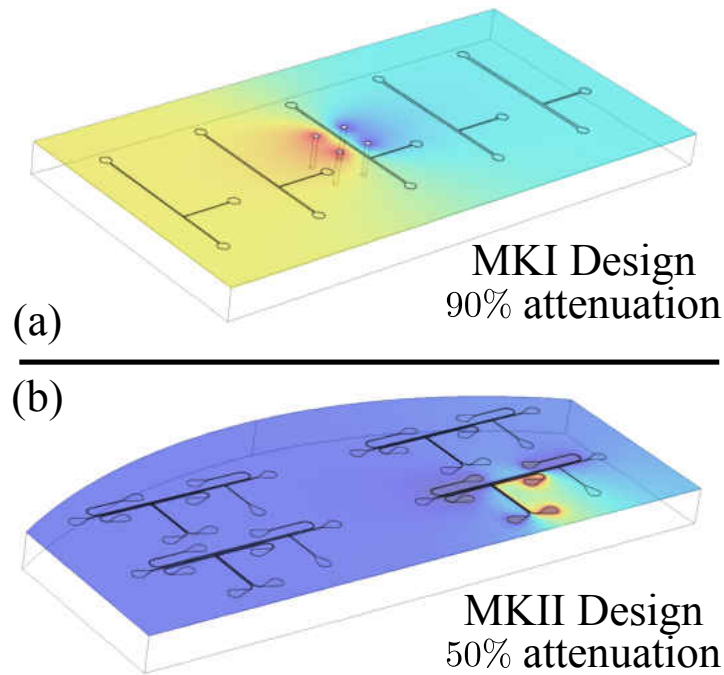


Figure 34: Three-dimensional electrostatic simulation of electrical potential distributions for MKI (a) and MKII (b) microchannel designs. Red color indicates applied potential ($V = V_0$) and blue indicates grounded region ($V = 0$).

the MKII design, three regions are clearly consistent between experimental and numerical droplet behavior. Upstream of the pinning site, the droplet deforms into a prolate spheroid due to the electric field developing across the channel width and the fluids' material properties. The pinning site causes droplet deceleration, and pinning if the electric force is strong enough. If the droplet is not pinned, then downstream of the pinning site the droplet is not electrified, and returns to its nominal shape. These regions are highlighted in figure 35 for experimental and three-dimensional numerical simulations.

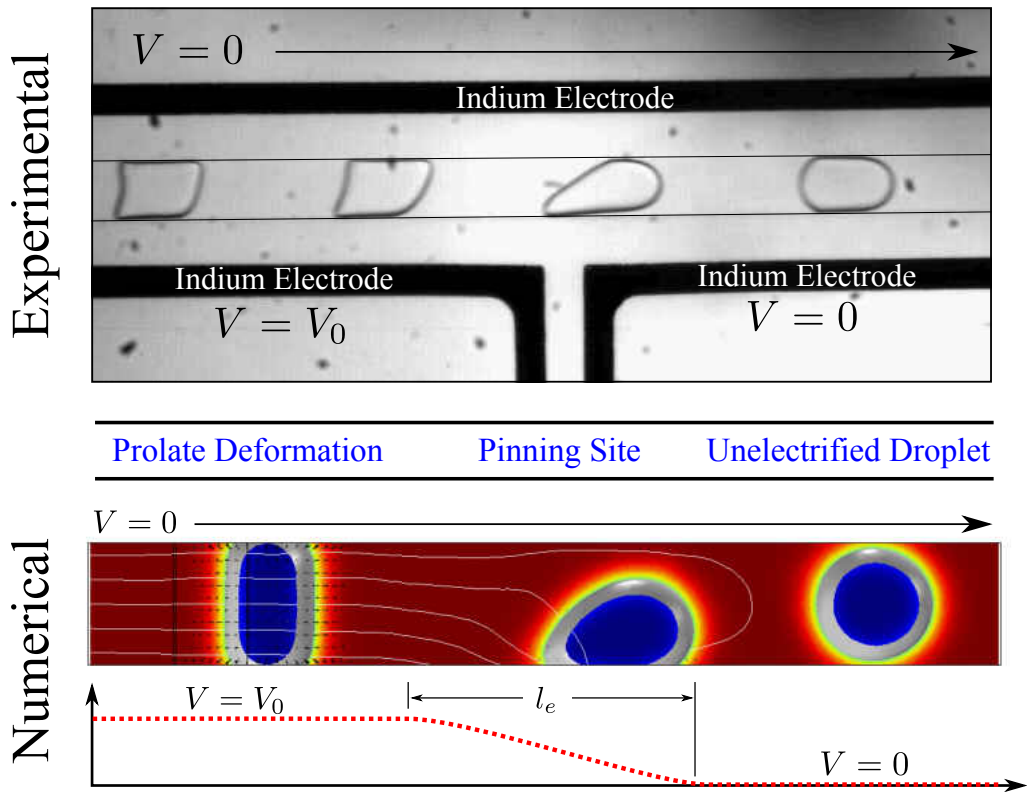


Figure 35: Qualitative comparison between experiments conducted on the MKII channel design and three-dimensional numerical droplets. Drop sizes observed experimentally for the MKII channel design were not exactly matched numerically. Two-dimensional numerical droplets depicted identical behavior, and are therefore not shown. The continuous fluid is silicone oil and the dispersed fluid is deionized water (see table 2 for material properties).

Droplet Routing

This pinning phenomena can be exploited by applying steep gradients in electrical potential at specific locations within a microchannel, thus allowing for precise control over flowing liquid droplet emulsions. A simplified T-junction configuration is numerically simulated two-dimensionally for two different diameter droplets: $d = 70\mu m$, and $d = 138\mu m$ (refer to figure 36). A steep electrical potential gradient is applied at either the upper or lower corner in order to route a droplet into either the upper or lower branch of the T-junction microchannel. Passive droplet routing is possible in this

configuration and is attributed to identical phenomena as seen with pinning. As a flowing droplet approaches the T-junction, the electric force caused by the steep electrical potential gradient in the corner begins to decelerate the droplet on one side. As the droplet decelerates, the viscous shear and upstream pressure buildup induced by the continuous flow causes the droplet to turn into the upper part of the T-junction, effectively pivoting around the electrified corner. The critical electrical potential for pinning the smaller drop at the corner is between $100V$ and $200V$, while the critical electrical potential for pinning the larger drop is between $200V$ and $300V$, suggesting the effects are also dependent on drop size under these flow conditions (same trend as figure 29).

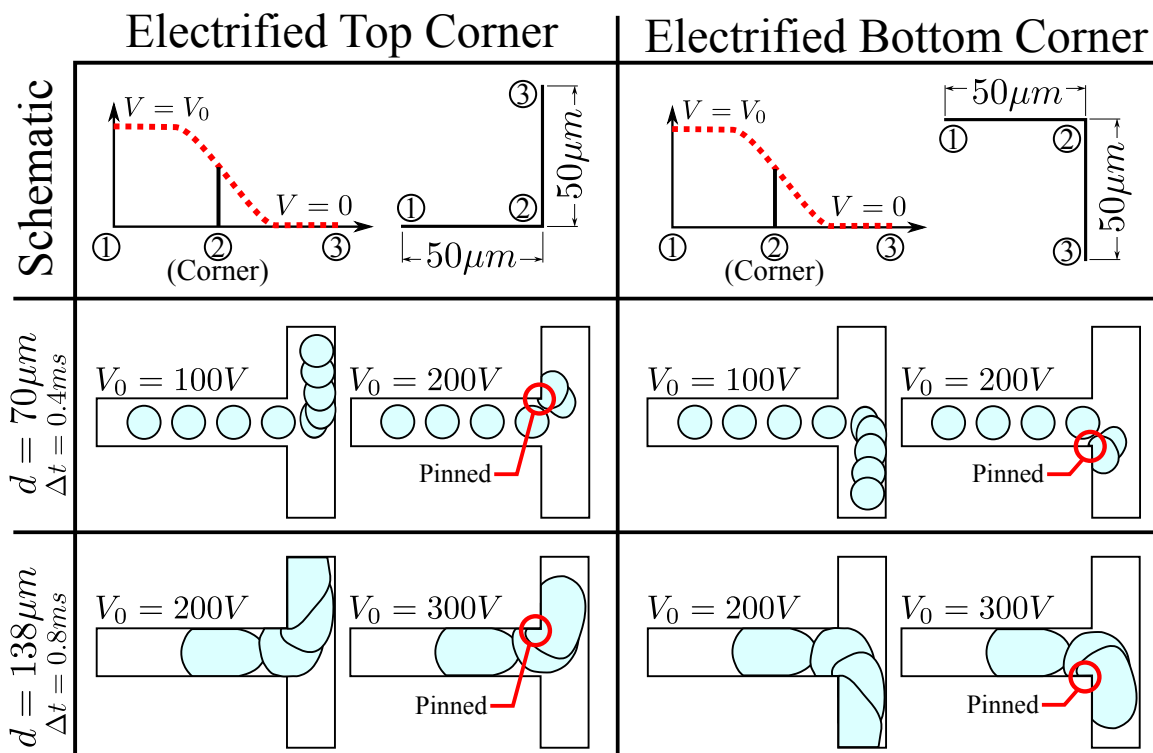


Figure 36: Two-dimensional numerical simulation of droplet routing configurations. Schematic and sequence of images at different times are listed for a T-junction electrified in the top corner (left column), and the bottom corner (right column) for two different drop diameters (d). Once pinned, the droplet position at all future time steps overlap the final pinning location (droplet totally arrested with no additional deformation). The channel width is $100\mu m$, and fluid properties are listed in table 2.

This behavior is consistent for flow situations according to the following set of hydrodynamic parameter values: Reynolds number ($Re = \rho_c u_c w_c / \mu_c \approx 1$), Froude number ($Fr = u_c / \sqrt{g w_c} \approx 6.4$), Weber number ($We = \rho_c u_c^2 w_c / \gamma \approx 0.1$), and capillary number ($Ca = \mu_c u_c / \gamma \approx 0.1$). The dimensionless parameters that account for the electric field strength are listed in table 6.

Table 6: List of dimensionless hydrodynamic / electric force ratios for two-dimensional routing simulations, according to equation 25b.

Number	$d = 70\mu m$		$d = 138\mu m$	
	$V_0 = 100V$ (not pinned)	$V_0 = 200V$ (pinned)	$V_0 = 200V$ (not pinned)	$V_0 = 300V$ (pinned)
Eu_e	0.75	0.19	0.73	0.32
Ma	8.58	2.15	4.23	1.88
Ps	17.16	4.29	8.46	3.76
Ca_e^{-1}	23.10	5.78	5.78	2.57

For all dimensionless force ratios listed in 6, as the value of the applied electrical potential decreases, the magnitude should increase because all of the ratios contain the hydrodynamic force in their numerators. As the applied electrical potential increases, the dimensionless number decreases due to the larger electric force in the denominator. In the simulations where each of the droplets were not pinned ($V_0 = 100V$ for $d = 70\mu m$, and $V_0 = 200V$ for $d = 138\mu m$), the hydrodynamic forces are large compared to the electric forces. As the electric forces are increased, the ratios decrease and the droplets are pinned at the corner where the steep gradient of electrical potential is applied. These results are also covered by Wehking et al [64].

An identical three-dimensional numerical study was performed for the simplified T-junction configuration (refer to figure 37). The two droplet sizes tested were identical to the dimensionless drop sizes in 2D, but since the droplet are normalized according to the hydraulic diameter in 3D [$d_h = 2w_c h / (w_c + h)$], the dimensional drop sizes varied. The two drop diameters tested were $d = 46.7\mu m$ and $d = 92\mu m$ (corresponding to $d^* = 0.7$ and $d^* = 1.38$, respectively). Routing

of droplets in 3D follow the same behavior as those in 2D, and is attributed to the same effects: namely, the decelerating of the droplet by the corner electric force allowing the viscous and pressure forces to rotate the droplet into the branch. If the electric forces are too large, then the hydrodynamic surface forces are insufficient to keep the droplet flowing and the droplet is pinned at the branch corner. If the electric forces are too small, the droplet would be unaffected by these forces and follow any bias in the flow field in choosing which direction to travel. Thus, a balance must be achieved between these two extremes in designing a passive droplet routing system. Hydrodynamic parameters used for these simulations are the Reynolds number ($Re = \rho_c u_c d_h / \mu_c \approx 0.1$), Froude number ($Fr = u_c / \sqrt{g w_c} \approx 1.2$), Weber number ($We = \rho_c u_c^2 w_c / \gamma \approx 0.001$), and capillary number ($Ca = \mu_c u_c / \gamma \approx 0.01$).

Table 7: List of dimensionless hydrodynamic / electric force ratios for three-dimensional routing simulations, according to equation 25b.

Number	$d = 46.7\mu m$		$d = 92\mu m$	
	$V_0 = 150V$ (not pinned)	$V_0 = 200V$ (pinned)	$V_0 = 150V$ (not pinned)	$V_0 = 200V$ (pinned)
Eu_e	0.002	0.001	0.017	0.009
Ma	1.452	0.817	5.636	3.170
Ps	5.808	3.267	22.542	12.680
Ca_e^{-1}	15.064	8.473	29.675	16.692

The hydrodynamic forces in three-dimensional simulations are larger than their two-dimensional counterparts with respect to the environment required for pinning. This is illustrated by the larger dimensionless numbers in table 7 when compared to table 6. From both tables it is evident that the hydrodynamic inertial forces are very small relative to the electric forces (for the fluids tested), and thus play very little role in the simulated routing system. However, the interfacial and pressure forces have the largest effect in the system, followed closely by the viscous forces. These findings are consistent with order of magnitude analyses of other droplet based microfluidic systems without electric fields [11, 12].

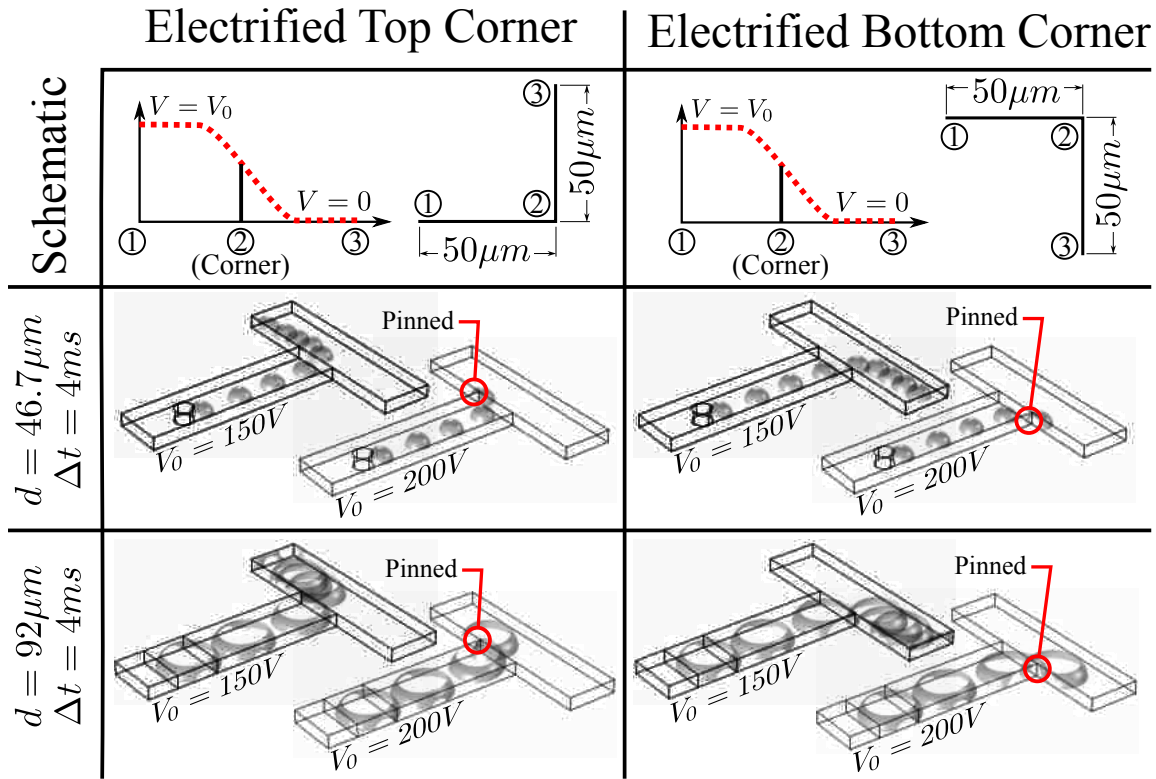


Figure 37: Three-dimensional numerical simulation of droplet routing configurations. Schematic and sequence of images at different times are listed for a T-junction electrified in the top corner (left column), and the bottom corner (right column) for two different drop diameters (d). Once pinned, the droplet position at all future time steps overlap the final pinning location (droplet totally arrested with no additional deformation). The channel width and height are $100\mu m$, and $50\mu m$ respectively, and fluid properties are listed in table 2.

Droplet Binning by Size

Droplet control is further enhanced by extending the simplified routing demonstration to droplet binning. Binning refers to a system's ability to automatically sort more than one object by some physical criteria. This is the exact mechanism used to in coin sorting devices, where a group of different coins can enter the device and be grouped automatically by type. This is possible because all of the coins, after entering the device, will pass over a series of different sized openings that will

only let through coins smaller than the opening. In the case of a droplet producing microfluidic system, the droplet size was also chosen as the physical criteria for binning into different sized branch channels. While the coins' weight is the force that makes coin binning possible (by gravity pulling a coin through an opening), the electric force is responsible for droplet binning. The following simulations illustrates how two droplets of different size are sorted by leveraging the same electric forces responsible for droplet deceleration and pinning.

Two-dimensional droplet binning was simulated using the fluid properties listed in table 2. The continuous channel width remained constant at $w_c = 200\mu m$, but branched off into a $140\mu m$ width channel, followed by a $200\mu m$ width channel further downstream, both angled at 60° from the downstream horizontal direction. The flow rate was set to obtain a Reynolds number of $Re = 0.4$. The electrical potential boundary conditions were set similar to the routing configuration detailed in figures 36 and 37, such that droplets would decelerate and flow into each of the 60° branches. This required the steep gradient in electrical potential to be located at the upstream corner of the upper channel walls where the branches started. Two deionized water droplets of diameters $140\mu m$ and $226\mu m$ were generated from two separate T-junctions (not simulated), and allowed to flow in silicone oil. The results of this simulation can be found in figure 38.

When no electric field was applied, both droplets flowed down the continuous channel without entering the branches (left column of images in figure 38), as there is insufficient electric force to cause the droplets to deviate away from the mainstream flow. The electric field with a steep gradient at the corners (right column of images in figure 38), however, produces enough electric force to route each of the droplets into their equivalently sized branches, thus binning them by size. As demonstrated with the droplet routing simulations, when the electric potential distribution in the corner is too abrupt or severe ($E_0 = V_0/l_e$ too large), the drops will be pinned to the wall due to the insurmountable electric force. If the electric force is too weak, the droplets will continue downstream unaffected. Thus, to achieve binning, a very precise balance between the

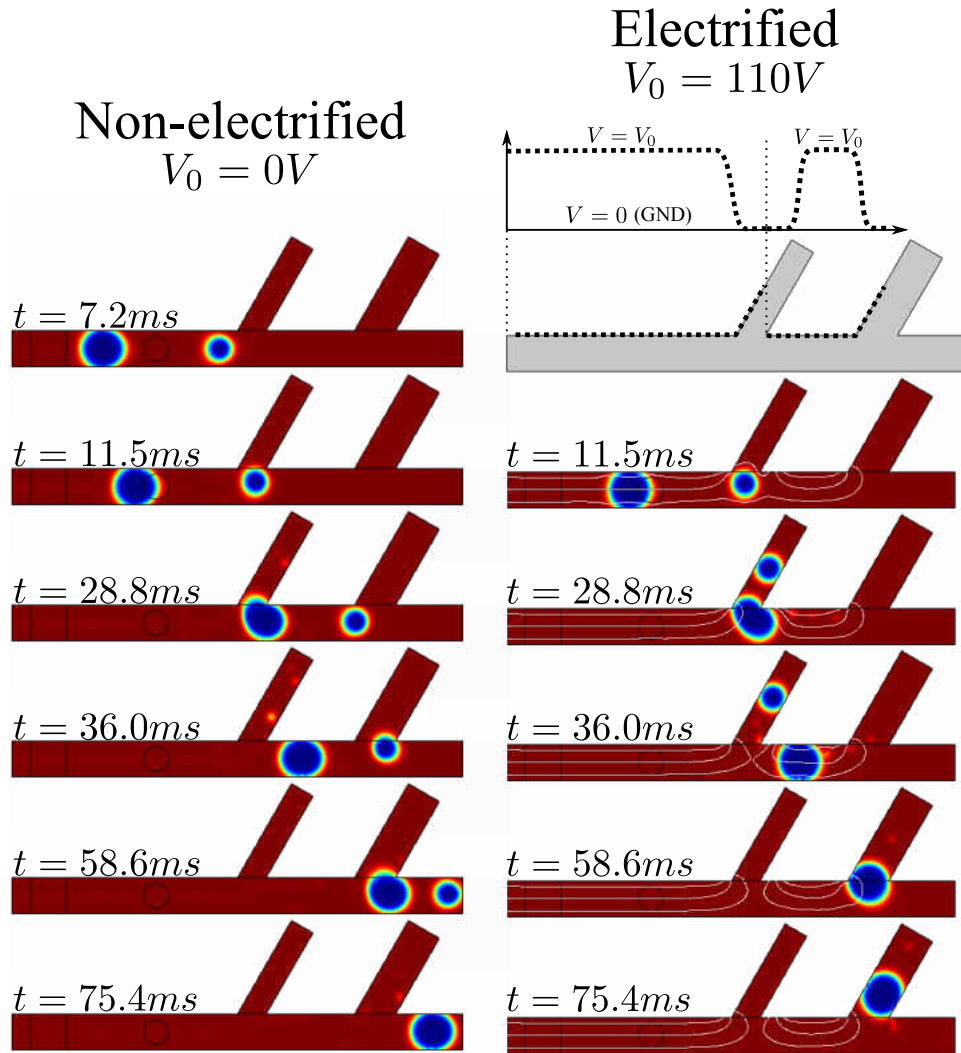


Figure 38: Two-dimensional numerical simulation of a two droplet binning configuration. Sequence of images are listed for the non-electrified two branch microchannel (left), and the electrified two branch microchannel (right), along with the electrical potential distribution at the channel wall.

electric and hydrodynamic forces is required. In the two-branch configuration shown in figure 38, the first droplet is routed and binned in the first branch due to sufficient electric forces for the given Reynolds number, branch angle (60°) and branch width. When the larger droplet reaches the first branch, the same electric force becomes insufficient for binning due to the increased drop

size. However, the same electric force approaching the second branch is sufficient for binning the larger diameter droplet due to the decrease in hydrodynamic forces downstream of the first branch. The hydrodynamic forces decrease downstream of the first branch because the fluid velocity must decrease in order to maintain flow continuity. Table 8 illustrates the dimensionless hydrodynamic to electric force ratios between the two droplet diameters at both the first and second branches.

Table 8: List of dimensionless hydrodynamic / electric force ratios for two-dimensional binning simulations, according to equation 25b. N/A values are due to the first droplet being binned at the first branch.

Number	First Branch		Second Branch	
	$d = 140\mu m$ (binned)	$d = 226\mu m$ (not binned)	$d = 140\mu m$ (-)	$d = 226\mu m$ (binned)
Eu_e	0.108	0.281	N/A	0.085
Ma	2.955	4.770	N/A	2.623
Ps	5.909	9.539	N/A	5.247
Ca_e^{-1}	38.184	38.184	N/A	38.184

All of the dimensionless numbers in table 8 contain the hydrodynamic forces in the numerator and the electric forces in their denominator, so a smaller force ratio correlates to a larger electric force (or smaller hydrodynamic force), and vice versa. Since the electric force remains constant between the two droplets in 2D, the criteria for routing a droplet into a branch is dependent on the strength of the hydrodynamic forces, which has already been shown to be dependent on the drop size. Approaching the first branch, the force ratios for the second larger droplet are larger than for the first smaller droplet. This is why the viscous shear (Ma) and upstream pressure forces (Ps) are able to bin the smaller diameter droplet (smaller Ma and Ps), while allowing the larger droplet to continue downstream (larger Ma and Ps). However, after passing the first branch, the hydrodynamic forces on the larger droplet are reduced due to the decreased flow rate (and average velocity). This is why the same electric force at the second branch, which was unable to bin the larger droplet at the first branch, is now able to bin the larger droplet at the second branch. This is

also supported by comparing the magnitudes of the force ratios between the $d = 140\mu m$ droplet at the first branch and the $d = 226\mu m$ droplet at the second branch.

Droplet binning was also simulated using three-dimensional numerical models using the same material properties listed in table 2. The continuous channel width remained constant at $w_c = 100\mu m$, but branched off into a $66.7\mu m$ width channel, followed by a $100\mu m$ width channel further downstream, both angled at 60° from the downstream horizontal direction. The flow rate was set to obtain a Reynolds number of $Re = 0.1$. The electrical potential boundary conditions were set similar to the two-dimensional binning simulations, such that droplets would decelerate and flow into each of the 60° branches. Two deionized water droplets of diameters $86\mu m$ and $125\mu m$ were generated from two separate T-junctions (not simulated), and allowed to flow in silicone oil. The results of this simulation can be found in figure 39.

The results are identical to two-dimensional simulations in that the first smaller diameter droplet is binned into the first smaller branch, while the second larger diameter droplet is binned into the second larger branch. The magnitudes of the dimensionless force ratios for this 3D two droplet binning system are listed in table 9.

Table 9: List of dimensionless hydrodynamic / electric force ratios for three-dimensional routing simulations, according to equation 25b. N/A values are due to the first droplet being binned at the first branch.

Number	First Branch		Second Branch	
	$d = 86\mu m$ (binned)	$d = 125\mu m$ (not binned)	$d = 86\mu m$ (-)	$d = 125\mu m$ (binned)
Eu_e	0.070	0.214	N/A	0.088
Ma	27.980	59.111	N/A	37.831
Ps	111.919	236.443	N/A	151.324
Ca_e^{-1}	173.375	251.999	N/A	251.999

The force ratio magnitudes for this binning system are much larger than for the two-dimensional

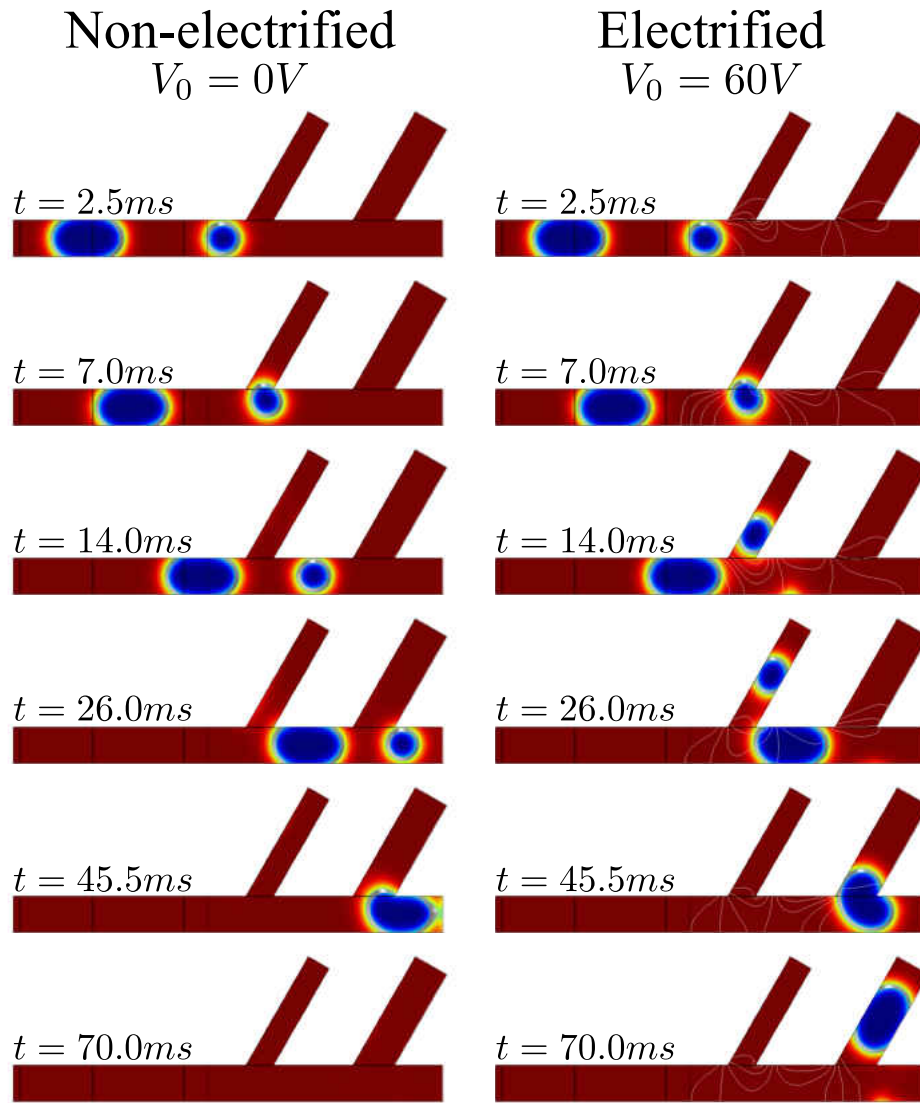


Figure 39: Three-dimensional numerical simulation of a two droplet binning configuration. Sequence of images are listed for the non-electrified two branch microchannel (left), and the electrified two branch microchannel (right). Electrical potential distribution locations are in the same corners illustrated in figure 38.

binning system. This is because the 3D system was optimized to find the lowest possible electric force required to bin the droplets simulated. Since this electric force is minimized, the force ratios

listed in table 9 will be maximized since the electric force is in their denominators. In addition, the electric force does not scale proportionally with the hydrodynamic forces per unit depth of the channel, as with 2D simulations. For example, as an unconfined droplet (whose boundaries do not contact the channel walls) is decelerating and migrating toward the electrified channel wall, the viscous shear and pressure forces are acting on three sides of the droplet rather than one. This will require additional electric force to pin the droplet, but pinning is not the objective in this system. Rather, it is the delicate balance between a slight deceleration on one side of the droplet and the hydrodynamic pushing of the droplet into a branch, all without pinning the droplet or forcing much larger droplets into the branch. Thus, for an optimized system, the already present hydrodynamic forces should do most of the work while the electric force simply helps to nudge droplets in the right direction (i.e. branch).

The balance between forces is more delicate with binning than with the routing system shown earlier since the angle between the branch and continuous channel is only 60° . The branch widths also play a role in permitting droplet binning. If the branch width is much larger than the droplet, the droplet will naturally flow into the branch when no electric force is applied. It may allow for another type of passive binning, but this system would need to be much more constrained since forces external to the hydrodynamics are absent. The ability to switch the binning on or off is also limited, where microvalves may be required that would drastically change the hydrodynamics of the system, and perhaps droplet production, when engaged. Droplet binning via electric fields offer a very non-intrusive method of permitting droplet binning that can be easily switched on or off without drastically affecting the hydrodynamics of the system.

This simplified two drop case demonstrates that droplet binning by size can be conducted passively and on demand for a given combination of electrical, flow, and geometric parameters.

CHAPTER 7: CONCLUSION

In conclusion, this work provided a fundamental framework, with some experimental validations, for understanding droplet emulsion dynamics in a microfluidic channel with applied electric fields. It outlined two primary models used in electrohydrodynamics: the leaky dielectric model and the perfect dielectric model. Finite element numerical results of stationary droplet deformations, implemented using the level set method, compared well both qualitatively (prolate/oblate and vortex directions), and quantitatively with results published by other researchers. Errors of less than 7.5% were found when comparing three-dimensional (3D) numerical results of this study to results predicted by the 3D leaky dielectric model, for a stationary high conductivity drop suspended in a slightly lower conductivity suspending medium. Droplet formations in a T-junction with no applied electric field were adequately predicted numerically using the level set finite element technique, as demonstrated by other researchers and verified in this study. For 3D models, droplet size was within 6%, and droplet production frequency was within 2.4% of experimental values found in the microfluidic T-junction device. In order to reduce computational complexity, a larger scale model was solved first to obtain electrical potential distributions localized at the channel walls for the electrode placement configurations.

Droplet deceleration and pinning was demonstrated, both experimentally and numerically, by applying steep gradients of electrical potential to the microchannel walls. As droplets flowed over these electrical potential “steps,” they were pinned to the channel walls if the resulting electric forces were large enough to overcome the hydrodynamic forces. A balance between four dimensionless force ratios, the electric Euler number (Eu_e – ratio of inertial to electric forces), Mason number (Ma – ratio of viscous to electric forces), electric pressure (Ps – ratio of upstream pressure forces to electric forces), and the electric capillary number (Ca_e – ratio of electric to capillary forces) were used to quantify the magnitudes of each of these forces required to pin a droplet,

and was consistent with a cubic dependency the drop diameter. For larger drop diameters, effects of hydrodynamic forces become more prominent, and for smaller droplets, a greater electric forces was required due to the proximity of the droplet boundary with reference to the electrified channel wall. Droplet deceleration and pinning was exploited to route droplets into different branches of a microfluidic T-junction in this study. In addition, using steep electrical potential gradients placed strategically along a microchannel, droplets were even passively binned by size into separate branches of the microfluidic device. These characteristics have been identified and demonstrated in this work.

Further work in this field will continue to advance the capabilities of electrohydrodynamics in droplet producing microfluidic systems. Using the results of this work, a deeper look into the dimensionless force balance as it applies to the more complex surface geometry of decelerating deforming droplets is needed. In addition, relating that dependency back to the droplet size (or diameter) would help generalize the model. Applying this model to a generic binning system, that includes the effects of branch size and branch angle would provide a very powerful and useful tool for microfluidic designers. This study paves the way for these and other advances in leveraging electrohydrodynamics to manipulate and control liquid droplet emulsions in microfluidic devices.

REFERENCES

- [1] Gordon F. Christopher and Shelly L. Anna. Microfluidic methods for generating continuous droplet streams. *Journal of Physics D: Applied Physics*, 40:R319–R336, 2007.
- [2] Frieder Mugele and Jean-Christophe Baret. Electrowetting: from basics to applications. *Journal of Physics: Condensed Matter*, 17:R705–R774, 2005.
- [3] Hao Gu, Chandrashekar U. Murade, Michael H. G. Duits, and Frieder Mugele. A microfluidic platform for on-demand formation and merging of microdroplets using electric control. *Biomicrofluidics*, 5:011101, 2011.
- [4] Brian J. Kirby. *Micro- and Nanoscale Fluid Mechanics : Transport in Microfluidic Devices*. Cambridge University Press, 2010.
- [5] David C. Duffy, J. Cooper McDonald, Olivier J. A. Schueller, and George M. Whitesides. Rapid prototyping of microfluidic systems in poly(dimethylsiloxane). *Analytical Chemistry*, 70:4974–4984, 1998.
- [6] J. Cooper McDonald, David C. Duffy, Janelle R. Anderson, Daniel T. Chiu, Hongkai Wu, Olivier J. A. Schueller, and George M. Whitesides. Fabrication of microfluidic systems in poly(dimethylsiloxane). *Electrophoresis*, 21:27–40, 2000.
- [7] Adam C Siegel, Derek A Bruzewicz, Douglas B Weibel, and George M Whitesides. Microsolidics: Fabrication of three-dimensional metallic microstructures in poly (dimethylsiloxane). *Advanced Materials*, 19(5):727–733, 2007.
- [8] Shia-Yen Teh, Robert Lin, Lung-Hsin Hungb, and Abraham P. Lee. Droplet microfluidics. *Lab on a Chip*, 8:198–220, 2008.

- [9] Ralf Seemann, Martin Brinkmann, Thomas Pfohl, and Stephan Herminghaus. Droplet based microfluidics. *Reports on Progress in Physics*, 75:016601, 2012.
- [10] Todd Thorsen, Richard W. Roberts, Frances H. Arnold, and Stephen R. Quake. Dynamic pattern formation in a vesicle-generating microfluidic device. *Physical Review Letters*, 86:4163–4166, 2001.
- [11] Gordon F. Christopher, N. Nadia Noharuddin, Joshua A. Taylor, and Shelly L. Anna. Experimental observations of the squeezing-to-dripping transition in t-shaped microfluidic junctions. *Physical Review E (Statistical, Nonlinear, and Soft Matter Physics)*, 78:036317 (12 pp.), 2008.
- [12] Piotr Garstecki, Michael J. Fuerstman, Howard A. Stone, and George M. Whitesides. Formation of droplets and bubbles in a microfluidic T-junction - scaling and mechanism of break-up. *Lab on a Chip*, 6:437–446, 2006.
- [13] Joeska Husny and Justin J. Cooper-White. The effect of elasticity on drop creation in t-shaped microchannels. *Journal of Non-Newtonian Fluid Mechanics*, 137:121–136, 2006.
- [14] J. H. Xu, S. W. Li, J. Tan, and G. S. Luo. Correlations of droplet formation in T-junction microfluidic devices: from squeezing to dripping. *Microfluid Nanofluid*, 5:711–717, 2008.
- [15] J. H. Xu, S. W. Li, J. Tan, Y. J. Wang, and G. S. Luo. Preparation of highly monodisperse droplet in a T-junction microfluidic device. *AIChE*, 52:3005–3010, 2006.
- [16] J. H. Xu, S. W. Li, J. Tan, Y. J. Wang, and G. S. Luo. Controllable preparation of monodisperse o/w and w/o emulsions in the same microfluidic device. *Langmuir*, 22:7943–7946, 2006.

- [17] J. H. Xu, G. S. Luo, S. W. Li, and G. G. Chen. Shear force induced monodisperse droplet formation in a microfluidic device by controlling wetting properties. *Lab on a Chip*, 6:131–136, 2006.
- [18] Shiyi Chen and Gary D. Doolen. Lattice boltzmann method for fluid flows. *Annual Review of Fluid Mechanics*, 30:329–364, 1998.
- [19] Amit Gupta, S. M. Sohel Murshed, and Ranganathan Kumar. Droplet formation and stability of flows in a microfluidic T-junction. *Applied Physics Letters*, 94:164107, 2009.
- [20] Amit Gupta and Ranganathan Kumar. Effect of geometry on droplet formation in the squeezing regime in a microfluidic T-junction. *Microfluid Nanofluid*, 8:799–812, 2010.
- [21] Amit Gupta and Ranganathan Kumar. Flow regime transition at high capillary numbers in a microfluidic T-junction: Viscosity contrast and geometry effect. *Physics of Fluids*, 22:122001, 2010.
- [22] M. DeMenech, P. Garstecki, F. Jousse, and H. A. Stone. Transition from squeezing to dripping in a microfluidic t-shaped junction. *Journal of Fluid Mechanics*, 595:141–161, 2008.
- [23] Jonathan D. Wehking, Michael Gabany, Larry Chew, and Ranganathan Kumar. Effects of viscosity, interfacial tension, and flow geometry on droplet formation in a microfluidic T-junction. *Microfluidics and Nanofluidics*, pages 1–13, 2013.
- [24] Junghoon Lee and Chang-Jin Kim. Surface-tension-driven microactuation based on continuous electrowetting. *Journal of Microelectromechanical Systems*, 9:171–180, 2000.
- [25] Masahide Gunji and Masao Washizu. Self-propulsion of a water droplet in an electric field. *Journal of Physics D: Applied Physics*, 38:2417–2423, 2005.
- [26] Tom Krupenkin and J. Ashley Taylor. Reverse electrowetting as a new approach to high-power energy harvesting. *Nature Communications*, 2:448, 2011.

- [27] Michele Zagnoni and Jonathan M. Cooper. On-chip electrocoalescence of microdroplets as a function of voltage, frequency and droplet size. *Lab on a Chip*, 9:2652–2658, 2009.
- [28] Michele Zagnoni, Guillaume Le Lain, and Jonathan M. Cooper. Electrocoalescence mechanisms of microdroplets using localized electric fields in microfluidic channels. *Langmuir*, 26(18):14443–14449, 2010.
- [29] Ronald Pethig. Dielectrophoresis: Status of the theory, technology, and applications. *Biomicrofluidics*, 4:022811, 2010.
- [30] Yandong Gao, Teck Neng Wong, Chun Yang, and Kim Tiow Ooi. Two-fluid electroosmotic flow in microchannels. *Journal of Colloid and Interface Science*, 284:306–314, 2005.
- [31] Haiwang Li, Teck Neng Wong, and Nam-Trung Nguyen. Analytical model of mixed electroosmotic/pressure driven three immiscible fluids in a rectangular microchannel. *International Journal of Heat and Mass Transfer*, 52:4459–4469, 2009.
- [32] Haiwang Li, Teck Neng Wong, and Nam-Trung Nguyen. Time-dependent model of mixed electroosmotic/pressure-driven three immiscible fluids in a rectangular microchannel. *International Journal of Heat and Mass Transfer*, 53:772–785, 2010.
- [33] Haiwang Li, Teck Neng Wong, and Nam-Trung Nguyen. Microfluidic switch based on combined effect of hydrodynamics and electroosmosis. *Microfluid Nanofluid*, 10:965–976, 2011.
- [34] Sir Geoffrey Taylor. Disintegration of water drops in an electric field. *Proceedings of the Royal Society of London: Series A*, 280:383–397, 1964.
- [35] R. S. Allan and S. G. Mason. Particle behaviour in shear and electric fields. i. deformation and burst of fluid drops. *Proceedings of the Royal Society of London: Series A*, 267:45–61, 1962.

- [36] Sir Geoffrey Taylor. Studies in electrohydrodynamics i. the circulation produced in a drop by an electric field. *Proceedings of the Royal Society of London: Series A*, 291:159–166, 1966.
- [37] J. R. Melcher and G. I. Taylor. Electrohydrodynamics: A review of the role of interfacial shear stresses. *Annual Review of Fluid Mechanics*, 1:111–146, 1969.
- [38] D. A. Saville. Electrohydrodynamics: The Taylor-Melcher leaky dielectric model. *Annual Review of Fluid Mechanics*, 29:27–64, 1997.
- [39] S. Torza, R. G. Cox, and S. G. Mason. Electrohydrodynamic deformation and burst of liquid drops. *Philosophical Transactions of the Royal Society of London: Series A*, 269:295–319, 1971.
- [40] O. Vizika and D. A. Saville. The electrohydrodynamic deformation of drops suspended in liquids in steady and oscillatory electric fields. *Journal of Fluid Mechanics*, 239:1–21, 1992.
- [41] J. D. Sherwood. Breakup of fluid droplets in electric and magnetic fields. *Journal of Fluid Mechanics*, 188:133–146, 1988.
- [42] James Q. Feng and Timothy C. Scott. A computational analysis of electrohydrodynamics of a leaky dielectric drop in an electric field. *Journal of Fluid Mechanics*, 311:289–326, 1996.
- [43] Jinsong Hua, Liang Kuang Lim, and Chi-Hwa Wang. Numerical simulation of deformation/motion of a drop suspended in viscous liquids under influence of steady electric fields. *Physics of Fluids*, 20:113302, 2008.
- [44] Yuan Lin, Paal Skjetne, and Andreas Carlson. A phase field model for multiphase electrohydrodynamic flow. *International Journal of Multiphase Flow*, 45:1–11, 2012.
- [45] Yuan Lin. Two-phase electro-hydrodynamic flow modeling by a conservative level set model. *Electrophoresis*, 34:1–9, 2013.

- [46] J. M. Lopez-Herrera, S. Popinet, and M. A. Herrada. A charge-conservative approach for simulating electrohydrodynamic two-phase flows using volume-of-fluid. *Journal of Computational Physics*, 230:1939–1955, 2011.
- [47] Junfeng Zhang and Daniel Y. Kwok. A 2D lattice boltzmann study on electrohydrodynamic drop deformation with the leaky dielectric theory. *Journal of Computational Physics*, 206:150–161, 2005.
- [48] James Q. Feng. A 2D electrohydrodynamic model for electrorotation of fluid drops. *Journal of Colloid and Interface Science*, 246:112–121, 2002.
- [49] Masayuki Sato, Sadayoshi Kato, and Masahiro Saito. Production of oil/water type uniformly sized droplets using a convergent ac electric field. *IEEE Transactions on Industry Applications*, 32:138–145, 1996.
- [50] Arturo Fernandez and Gretar Tryggvason. The effects of electrostatic forces on the distribution of drops in a channel flow: Two-dimensional oblate drops. *Physics of Fluids*, 17:093302, 2005.
- [51] Pushpendra Singh and Nadine Aubry. Transport and deformation of droplets in a microdevice using dielectrophoresis. *Electrophoresis*, 28:644–657, 2007.
- [52] Shuai Gong, Ping Cheng, and Xiaojun Quan. Lattice boltzmann simulation of droplet formation in microchannels under an electric field. *International Journal of Heat and Mass Transfer*, 53:5863–5870, 2010.
- [53] Emilij K. Zholkovskij, Jacob H. Masliyah, and Jan Czarnecki. An electrokinetic model of drop deformation in an electric field. *Journal of Fluid Mechanics*, 472:1–27, 2002.

- [54] Lung-Hsin Hung and Abraham P. Lee. Optimization of droplet generation by controlling pdms surface hydrophobicity. In *ASME International Mechanical Engineering Congress and RD&D Expo*, 2004.
- [55] Anna-Karin Tornberg and Bjorn Engquist. A finite element based level-set method for multiphase flow applications. *Computing and Visualization in Science*, 3:93–101, 2000.
- [56] John D. Anderson. *Computational Fluid Dynamics*. McGraw-Hill, 1995.
- [57] Elin Olsson and Gunilla Kreiss. A conservative level set method for two phase flow. *Journal of Computational Physics*, 210:225–246, 2005.
- [58] Elin Olsson, Gunilla Kreiss, and Sara Zahedi. A conservative level set method for two phase flow II. *Journal of Computational Physics*, 225:785–807, 2007.
- [59] Bruno Lafaurie, Carlo Nardone, Ruben Scardovelli, Stephane Zaleski, and Gianluigi Zanetti. Modelling mergeing and fragmentation in multiphase flows with surfer. *Journal of Computational Physics*, 113:134–147, 1994.
- [60] Knut Erik Teigen, Karl Yngve Lervag, and Svend Tollak Munkejord. Sharp interface simulations of surfactant-covered drops in electric fields. In *European Conference on Computational Fluid Dynamics*, 2010.
- [61] Knut Erik Teigen Giljarhus and Svend Tollak Munkejord. Numerical investigation of eletrostatically enhanced coalescence of two drops in a flow field. In *IEEE International Conference on Dielectric Liquids*, 2011.
- [62] Shazia Bashir, Julia M. Rees, and William B. Zimmerman. Simulations of microfluidic droplet formation using the two-phase level set method. *Chemical Engineering Science*, 66:4733–4741, 2011.

- [63] Marrivada Nanchara Reddy and Asghar Esmaeeli. The ehd-driven fluid flow and deformation of a liquid jet by a transverse electric field. *International Journal of Multiphase Flow*, 35:1051–1065, 2009.
- [64] Jonathan D. Wehking, Larry Chew, and Ranganathan Kumar. Droplet deformation and manipulation in an electrified microfluidic channel. *Applied Physics Letters*, 103:054101, 2013.